TUM School of Computation, Information and Technology

Development of a Phase Imaging Flow Cytometer for Blood Cell Aggregate Diagnosis

Christian Klenk, M.Sc.

Vollständiger Abdruck der von der TUM School of Computation, Information and Technology der Technischen Universität München zur Erlangung des akademischen Grades eines

Doktors der Ingenieurwissenschaften (Dr.-Ing.)

genehmigten Dissertation.

Vorsitz:		Prof. Dr.-Ing. Klaus Diepold
Prüfende der Dissertation	1.	Prof. Dr. Oliver Hayden
	2.	apl. Prof. Dr. Hristo Iglev
	3.	Prof. Dr. Alice Assinger

Die Dissertation wurde am 02.08.2023 bei der Technischen Universität München eingereicht und durch die TUM School of Computation, Information and Technology am 14.05.2024 angenommen.

Dedication

Diese Arbeit ist meinem Vater Dr. Herbert Klenk gewidmet.

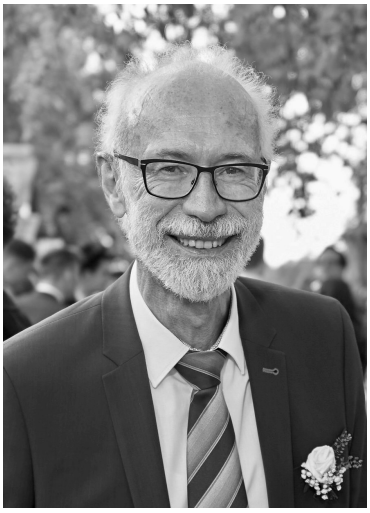

⋆ 17. Juni 1950 † 27. July 2021

Jeremia 31,3: Ich habe dich je und je geliebt, darum habe ich dich zu mir gezogen aus lauter Güte.

Papa, du hast mir vorgelebt, worauf es im Leben wirklich ankommt und bist mir zeitlebens ein Vorbild wahrer Größe. Ich weiß du bist jetzt an einem besseren Ort.

Acknowledgement

I would like to express my gratitude to all who contributed to the success of this work:

Prof. Dr. Oliver Hayden, for giving me the opportunity to work in your research group. I could not have undertaken this journey without your constant support, guidance, ideas, and valuable feedback.

Dr. Martin Brischwein, for mentoring me throughout the whole process. I am grateful for our regular exchanges on my research topics and teaching matters. I have benefited greatly from your experience.

I am also grateful to all my colleagues at the Heinz-Nixdorf-Chair of Biomedical Electronics, who have enriched this time considerably. Thank you, **Ellen Emken**, **Martin Knopp**, **Mohsin Muhammad Malik**, and **Moritz Leuthner**, for your valuable support and the fun of working with you. I would like to extend my sincere thanks to **Dr. Mathias Reisbeck** for his practical suggestions, helpful advise and our inspiring discussions in the office. I'm extremely grateful to **Dominik Heim** for all the time we spent talking about the research project and much more. I also wish to thank **Dr. Matthias Ugele** who helped me especially at the beginning of my doctoral thesis.

I would like to thank all the members of the CellFace team. In particular, I would like to thank **Stefan Röhrl**, who joined the interdisciplinary research team at the same time as I did. Your openness, commitment and supportive attitude have been of great benefit to the project and to me personally. Furthermore, I would also like to thank **David Elias Fresacher**, **Manuel Lengl**, **Simon Schumann**, and **Prof. Dr. Klaus Diepold**.

Special thanks to all collaborators and medical experts for your unwavering guidance and unparalleled knowledge. Here, I want to especially thank **Dr. Johanna Erber**, **Dr. Sebastian Rasch**, **Prof. Dr. Stefan Holdenrieder**, **Prof. Dr. Percy A. Knolle**, **Dr. Martin Schlegel**, **Prof. Dr. Gerhard Schneider** and **Prof. Dr. Tobias Lahmer**.

Many thanks to my family and friends, on whom I have always been able to rely. In particular, I would like to thank my mother **Edeltraud Klenk** and my father **Herbert Klenk**, to whom I also dedicate this work. You always believed in me and invested a lot so that I could pursue my plans. This would not have been possible without you. Last but not least, I would like to express my deepest gratitude to my wonderful wife **Friederike**. Thank you, for your endless support and for always being by my side.

Abstract

Fully automated haematology analysers are an essential tool in routine diagnostics. They are the most frequently performed laboratory tests in clinical practice. Despite their decade-long refinement, many relevant markers still can't be measured today. This is often due to limitations in the preanalytical and analytical techniques. In this thesis, digital holographic microscopy was used as a detection unit to overcome some of the highlighted drawbacks. Due to the inherent high contrast of this quantitative phase imaging technique, undesirable preparation steps can be reduced. Combining the imaging technique with a microfluidic module and an image analysis lays the foundation for the novel phase imaging flow cytometer. To reach the maturity of a haematology analyser, further steps were taken. These include the implementation of cell concentration measurements and the investigation of quality control materials. The development of a specific labeling method for immune cells further extended the range of potential applications.

Improvements in image analysis enabled the detection of individual cells within a group of cells. This was used to describe the morphology and composition of blood cell aggregates directly in whole blood samples. Effects of sample ageing and in-vitro activation with adenosine diphosphate (ADP) were investigated for blood anticoagulated with either EDTA, citrate, heparin, or hirudin. This was performed to investigate the characteristics and dynamics of the biomarker and to demonstrate the oppertunities for kinetic measurements. Depending on the anticoagulant, the blood showed different ageing patterns. Blood anticoagulated with hirudin and EDTA showed good long time stability. For the in-vitro activation, an intermediate increase in aggregate numbers and sizes was seen in hirudin, citrate, and heparin blood. After this initial spike, more than 50 % of the aggregates disintegrated over the next nine minutes. Unlike the other anticoagulants, EDTA completely prevented the formation of new aggregates by ADP activation.

In a clinical study investigating the blood of COVID-19 patients, aggregates and their components could be identified within 30 minutes of blood collection. This time frame includes the sample logistics and the measurement, which was performed within 2 minutes. It qualifies the method for potential use in point-of-care testing. A positive correlation was found between the severity of COVID-19 and the number of platelet- and platelet-leukocyte aggregates. Additionally, the platelet aggregates' composition and the diameter and phase delay distribution of its platelets showed a connection to the patient's severity. Since blood cell aggregates have been observed in several etiologies, this approach is a promising bedside diagnostic tool for prognostic and predictive testing.

Zusammenfassung

Vollautomatische Hämatologie-Analysatoren sind ein wesentlicher Bestandteil der Routinediagnostik. Sie sind weltweit die am häufigsten durchgeführten Labortests in der klinischen Praxis. Trotz jahrzehntelanger Forschung und Entwicklung können jedoch auch heute noch viele relevante Marker nicht automatisiert gemessen werden. Dies liegt häufig an der aufwendigen Probenvorbereitung sowie an Limitationen der analytischen Methoden. In dieser Arbeit wurde ein digitales holographisches Mikroskop als bildgebendes Verfahren eingesetzt, um einige der bestehenden Nachteile zu überwinden. Aufgrund des hohen Kontrasts, den dieses quantitative Phasenkontrastverfahren liefert, können aufwändige Probenvorbereitungsschritte reduziert werden. Die Kombination der Bildgebung mit einer Mikrofluidik und einer angepassten Bildanalyse bildet die Grundlage für das resultierende Phase-Imaging-Durchflusszytometer. Um die Reife eines Hämatologie-Analysators zu erreichen, wurden weitere Schritte wie Zellkonzentrationsmessungen und Materialuntersuchungen zur Qualitätskontrolle implementiert. Durch die Entwicklung einer Methode zur spezifischen Markierung von Immunzellen konnte das Spektrum der möglichen Anwendungsgebiete zusätzlich erweitert werden.
Eine Optimierung der Bildanalyse, ermöglichte die Detektion von einzelner Zellen innerhalb eines Zellverbandes. Dies wurde verwendet, um die Morphologie und Zusammensetzung von Blutzellaggregaten und deren Bestandteile in Vollblutproben zu beschreiben. Um die Eigenschaften und die Dynamik der Aggregate näher bestimmen zu können, wurden diese in einem Alterungsexperiment und in einem in-vitro Aktivierungsversuch untersucht. Das Blut wurde hierbei in Blutröhrchen mit den verschiedenen Antikoagulantien EDTA, Heparin, Hirudin und Citrat gelagert. Je nach Gerinnungshemmer, zeigte das Blut unterschiedliche Alterungsmuster. Mit Hirudin und EDTA antikoaguliertes Blut erwies im Vergleich zu den anderen eine gute Langzeitstabilität. Bei der in-vitro Aktivierung mit Adenosindiphosphat (ADP) wurde bei Hirudin-, Citrat- und Heparin-Blut eine initiale Zunahme der Aggregatanzahl und -größe beobachtet. Nach diesem anfänglichen Ansteigen zerfielen mehr als 50 % der Aggregate innerhalb der folgenden neun Minuten. Im Gegensatz zu den anderen Antikoagulantien verhinderte EDTA vollständig die Bildung neuer Aggregate durch externe ADP-Aktivierung.
In einer klinischen Studie, in der das Blut von COVID-19 Patienten untersucht wurde, konnten Aggregate innerhalb von 30 Minuten nach der Blutentnahme analysiert werden. Dies schloss sowohl die Probenlogistik als auch die zweiminütige Messung ein und qualifiziert den Ansatz für den potenziellen Einsatz als Point-of-Care Test. In der genannten Studie konnte eine positive Korrelation zwischen dem Schweregrad der Erkrankung und der Anzahl der Thrombozyten und Thrombozyten-Leukozyten Aggregate festgestellt werden. Darüber hinaus zeigten die Zusammensetzung der Thrombozytenaggregate sowie die Größe und induzierte Phasenverschiebung der Thrombozyten einen weiteren Zusammen-

hang mit dem Schweregrad des Patienten. Da Blutzellaggregate bereits bei verschiedenen medizinischen Krankheitsbildern nachgewiesen werden konnten, stellt der Ansatz ein vielversprechendes und patientennahes Verfahren für die prognostische und prädiktive Diagnostik dar.

List of Abbreviations

ADP	Adenosine Diphosphate
CAC	COVID-19-Associated Coagulopathy
CBC	Complete Blood Count
CD	Cluster of Differentiation
COVID-19	Coronavirus disease 2019
CV	Coefficient of Variation
DHM	Digital Holographic Microscopy
DOF	Depth-of-Field
ECMO	Extracorporeal Membrane Oxygenation
ED	Equivalent Diameter
EDTA	Ethylene Diamine Tetraacetic Acid
FACS	Fluorescence-Activated Cell Sorting
FCN	Fully Convolutional Network
FEM	Finite Element Method
FFT	Fast Fourier Transformation
FOV	Field of View
GLCM	Grey-Level Co-occurrence Matrix
ICU	Intensive Care Unit
LP-Aggregate	Leukocyte-Platelet Aggregate
MFI	Mean-Fluorescence-Intensity
OHM	Optical Height Maximum
OPD	Optical Phase Difference
P-Aggregate	Platelet Aggregate
PBMCs	Peripheral Blood Mononuclear Cells
PBS	Phosphate-Buffered Saline
PCT	Procalcitonin
PDE	Partial Differential Equation
PDMS	Polydimethylsiloxane
PEO	Polyethylene oxide
PMMA	Polymethylmethacrylate
PRP	Platelet-Rich Plasma
PVP	Polyvinylpyrrolidone
QPI	Quantitative Phase Imaging
RoI	Regions of Interest
RPN	Region Proposal Network
TRAP	Thrombin Receptor Activating Peptide
VI	Virtual Instrument

List of Symbols

The symbols tabulated here are used throughout the work. The locally applied symbols, e.g., in the case of substitutions or intermediate results, are explained or defined in the respective context.

*	Complex conjugate
α	Off-axis angle between object and reference beam
β	Shear gradient
$\dot{\gamma}$	Shear rate
η	Fluid viscosity
θ	spatial frequency by the off-axis angle
λ	Wavelength
λ_0	Central wavelength of the light source
λ_t	Relaxation time of the fluid
$\Delta\lambda$	Bandwidth of the light source
μ_C	viscosity of the continuous phase
ρ	Fluid density
σ	Surface tension
τ	Shear stress
Φ	Phase of light
$\Phi(x, y)$	Phase distribution / Phase image
$\Phi_\mathrm{Obj}(x, y)$	Phase distribution of the object beam
$\Phi_\mathrm{Ref}(x, y)$	Phase distribution of the reference beam
Ψ	Temporal phase shift of the reference beam
A	Light amplitude
a_P	Particle radius
C_EL	Elastic lift coefficient
C_IL	Inertial lift coefficient
Ca	Capillary number
d	Lateral resolution
D_h	Hydraulic diameter
d_P	Particle diameter
DOF	Depth of Field / Axial resolution
$DOF_\mathrm{Geomertry}$	Geometrical optical depth of fields
DOF_Wave	Wave optical depth of fields
F_C	Shear-gradient-induced lift force
F_drag	Drag force
F_E	Viscoelastic force

F_{lift}	Total lift force on a particle
F_{S}	Shear-gradient lift force
F_{SS}	Slip-shear lift force
F_{W}	Wall-induced lift force
G_1	First function of the lateral position
G_2	Second function of the lateral position
h	Height of the microfluidic channel
$h(x, y)$	Height distribution
$I(x, y)$	Intensity distribution
$I_{\text{Hol}}(x, y)$	Intensity distribution of the hologram
$I_{\text{Obj}}(x, y)$	Intensity distribution of the object beam
$I_{\text{Ref}}(x, y)$	Intensity distribution of the reference beam
$K(x, y)$	Two-dimensional kernel
l	Length of the microfluidic channel
l_{C}	Coherence length
l_{O}	Length of the orifice
m	Magnification
$n(x, y)$	Refractive index distribution
N_1	First normal stress difference
N_2	Second normal stress difference
n_{m}	Refractive index of the medium
n_{ML}	Refractive index between medium and lens
NA	Numeric aperture
$O(x, y)$	Object beam
$\hat{O}(x, y)$	Scalar amplitude distribution of the object beam
Δp	Pressure drop across a microfluidic channel
p_{Sens}	Pixel size of the sensor
Q	Flow rate
Q_{C}	Flow rate of the continuous phase
Q_{D}	Flow rate of the disperse phase
$R(x, y)$	Reference beam
$\hat{R}(x, y)$	Scalar amplitude distribution of the reference beam
R_{F}	Fluidic resistance
S_{Sobel}	Sharpness function
v_{fluid}	Characteristic velocity of the fluid
v_{fmean}	Mean velocity of the fluid
v_{P}	Particle velocity
$v_x(y, z)$	Velocity of a particle in flow direction
w	Width of the microfluidic channel
w_{C}	Width of the continuous phase
w_{D}	Width of the disperse phase
w_{O}	Width of the orifice
w_{Out}	Width of the outlet
Wi	Weissenberg number
$Z(x, y)$	Two-dimensional image

Δz	z-Dimension difference between hologram and image plane
z_{H}	z-Dimension of the hologram plane
z_{IP}	z-Dimension of the image plane

Contents

1 Introduction

1.1 Motivation

The cellular analysis of the human blood has a long history. Its beginnings are dated back to the first published observation of red blood cells through the microscopist Antonie van Leeuwenhoek in 1675 [1, 2]. Another 160 years were needed until William Addison (1802–1881) and Gabrielle Andral (1797–1876) first discovered the white blood cells [3]. In 1842, Alfred Donné described platelets as another cellular component. These findings were followed by a discovery by Hayem in 1875 that white blood cells can be sub-classified by analysing their sizes alone. The use of aniline dyes for blood cell staining was introduced by Paul Ehrlich (1854-1915). Based on this principle, he could differentiate lymphocytes, neutrophils, eosinophils, and basophils. Until now, many more leukocyte subtypes and blood cell characteristics could be discovered. The analysis of blood cells is still a crucial tool for clinical decision makings in fields like immunology, virology, oncology, and many more [4–6].

Cellular analysis of blood cells is primarily performed on three levels. First, the Complete Blood Count (CBC) with leukocyte differential performed by established haematology analysers. Second, the study of cells and cell morphologies changes with microscopic methods, and third, the subcellular evaluation of blood cells and blood cell physiologies with, e.g. fluorescent flow cytometry. All devices have advantages and disadvantages, which is why specific techniques or a combination of several are used for different cases. Standard **haematology analysers** have been refined over many years, providing cheap tests, high precision, high accuracy, high throughput, and reaching high standardisation through automation. Despite their advantages, a manual slide review is still necessary in several cases due to a low spatial resolution and only a limited amount of classifiable cell types [7]. In addition, using a wide range of analytical techniques such as impedance, spectrometry, absorption, and conductivity measurements in combination with a microfluidic does not ensure comparability between results of different devices [8]. Lastly, many reagents are also used for preanalytical sample preparation, sample labeling, and instrument maintenance. Cellular analysis of stained blood cells with a microscope can compensate for many of these disadvantages. Techniques like the **Giemsa-stained blood smear analysis** are still common practice for evaluating cell morphology changes [9]. It is an improvement to the staining approaches of Paul Ehrlich and provides contrast-rich images with a high spatial resolution. Here, the nucleus of leukocytes and platelets are highlighted in purple while erythrocytes appear in pink [10]. This allows for an in-depth cell subtyping, evaluating cellular degeneration, and detecting a parasitic infection like malaria. However, highly skilled personnel are needed to implement and evaluate

such a test. The analysis is time-consuming, and compared to automated devices, only a small statistical amount of cells are analysed. Subsequently, this can lead to a high inter-observer variation of results [11–13]. **Flow cytometer approaches** with fluorescent labeling of cell surface proteins, allowing rapid and automated analysis of cells. As long as there is a suitable marker, both specific cell types and cell characteristics, like the activation of a cell, can be evaluated [14]. Disadvantages of this technique are the high cost of fluorescent markers, the time-consuming sample preparation, and the limited spatial resolution for morphology analysis.

To overcome the limitations of the existing gold standards, a combination of the automated fashion of the fluorescent flow cytometer and the high spatial resolution of microscopes was developed. This was achieved by the introduction of a microfluidic chip, the use of a high-speed camera, and suitable image analysis techniques in combination with different imaging approaches [15, 16]. The development was primarily driven by increasing computational resources and groundbreaking improvements in automated cell analysis. Thus, based on blood smear images, an automatic classification of different leukocytes [17] and other blood cells [18] as well as the detection of sickle cell anaemia [19] could be achieved. Furthermore, detecting malaria-infected erythrocytes and differentiating leukaemia subtypes could be automatically analysed using machine learning and simple morphology-based parameter approaches [20–23]. Combining the automated measurement fashion of a flow cytometer with automated image analysis of microscope images allows the study of large cell numbers with high spatial analysis. Due to the low contrast of cells in many imaging approaches, reliance on sample preparation methods and fluorescent markers is still needed [15, 16]. This limitation can be overcome using contrast-rich imaging methods like Quantitative Phase Imaging (QPI) [24]. Despite its not fully established state, imaging flow cytometers possess a great opportunity in the automated measurement and analysis of blood cells with high spatial resolution. This could result in the discovery of novel biomarkers, which potentially improve diagnostics and enhance clinical decision-making.

1.2 Objectives and Outline

The structure of this work is defined by its research objectives. First, an existing phase imaging flow cytometer with an included QPI device will be developed further towards a haematology analyser. Second, this created method will be used to analyse blood cell aggregates as a potential new biomarker in clinical diagnostics. Finally, the findings of the first two objectives are used to validate this new biomarker in a clinical COVID-19 study.

This thesis is structured into six chapters. In this chapter (**chapter 1**), the motivation behind this thesis is elaborated and a high-level overview of the objectives and outline is given. **Chapter 2** describes basic mechanisms and techniques that are important for discussing the findings in the research. It includes an overview of the underlying physical principles in different QPI techniques and microfluidics. Additionally, the physiological

processes of platelets and the coagulation cascade are explained to underline the mechanisms that lead to blood cell aggregation in COVID-19 patients. Chapters 3-5 each discuss one research objective. All of these chapters includes its methodology, results, and discussion section. In **chapter 3**, the process from a laboratory prototype toward a medical technology device is described. This includes an enhanced microfluidic cell manipulation for cell focusing. Furthermore, possible interfering variables that could influence the measurement results were investigated. Measuring cell concentrations, calibrator materials for quality control, and the specific differentiation of subcell types with similar morphology is highly relevant for haematology analysers. Therefore, these issues are addressed within several subchapters. **Chapter 4** investigates blood cell aggregates as a potential new biomarker in clinical diagnostics. This includes their formation and decay characteristics for ageing samples and when exposed to an external activator. The possibilities and limitations arising from using the phase imaging flow cytometer approach are also considered in this section. In **chapter 5**, the described method was used to analyse blood cell aggregates in blood samples from patients with COVID-19 infection. For this purpose, a study protocol was developed that enables a quasi-point-of-care analysis of patients with different degrees of severity. The various subsections compare blood cell aggregates with the disease severity and other established biomarkers. **Chapter 6** summarises this work with a conclusion and a brief outlook.

2 Theoretical Background

2.1 Quantitative Phase Imaging

Imaging biological samples such as cells and tissues with microscopic devices is highly significant for clinical diagnostics. Depending on the definition, microscopes have been used for the last four centuries [24] or even longer [25]. The underlying physical principle is the use of visible electromagnetic radiation as a source and a lens or a lens system to magnify an object. In standard light microscopy, the difference between lighter and darker parts of an image gives the contrast. These arise from light absorption or scattering in certain parts of the analysed object. However, this spatial variation and therefore the contrast is low for cells because of their small absorption coefficient for visible light, their small thickness, and an even smaller thickness variation [26]. Using chemical reagents like fluorescent or non-fluorescent dyes can improve the contrast of a cell but are usually cytotoxic. Furthermore, the staining requires additional pre-processing steps. Scanning and tomographic imaging techniques provide high contrast and sometimes even three-dimensional images but require multiple exposures and cost-intensive post-processing. An alternative approach is the observation of the phase properties from the probe beam. The phase of the light is susceptible to the thickness and refractive index changes and can be expressed as:

$$\Phi(x, y) = \frac{2\pi}{\lambda} h(x, y) n(x, y) \tag{2.1}$$

where $\Phi(x, y)$ is the phase distribution, λ is the wavelength of the light source, $n(x, y)$ is the refractive index distribution, and $h(x, y)$ is the height distribution of the sample. The relationship between $h(x, y)$ and $n(x, y)$ is called Optical Phase Difference (OPD) [27]. It follows that the phase difference between two points can be stated as:

$$\Phi_{\text{diff}} = \Phi_1 - \Phi_2 = \frac{2\pi}{\lambda}(h_1 n_1 - h_2 n_2) \tag{2.2}$$

The formula can be further simplified accordingly for equal refractive indices and/or equal heights across the two points. If this difference is assigned to an intensity value, it results in the contrast of a subsequent image. It can also be seen from equation 2.1 that an object's actual height can be computed if a sample's phase and refractive index

are given. One way to capture the quantitative phase values is by the interference of the sample beam (also called object beam) with a reference beam. The amplitude and phase information can be calculated from the resulting hologram in subsequent steps. Since state-of-the-art QPI-systems record holograms mostly on a digital sensor, the associated microscopy method is often referred to as Digital Holographic Microscopy (DHM).

In the 1930s, Zernike invented the first technique capable of measuring the phase contrast [28]. His approach was based on the understanding of Abbe that imaging is an interference process. Several years later, in 1948, Gabor developed a technique that laid the foundation for modern DHM [29]. Originally he wanted solely to improve the resolution of electron microscopy but realised in the process that the intensity of an electron beam from an object at the out-of-focus plane contains both the complete amplitude and phase information. A disadvantageous limitation of Gabor's approach was that the in-focus image was overlapped by a second out-of-focus image (so-called twin image). Those appeared because the intensity signal is generated by pairs of counter-propagating waves [24]. This problem was later on solved by Lohmann [30], Leith and Upatnieks [31] through the invention of the **off-axis approach**. Here, an off-axis angle (α) between the object ($O(x,y)$) and reference beam ($R(x,y)$) is introduced. This shifts the unwanted twin image onto a different axis than the in-focus image. For an object beam with $O(x,y) = \hat{O}(x,y) \cdot exp(i\Phi_{\mathrm{Obj}}(x,y))$ and the reference beam with $R(x,y) = \hat{R}(x,y) \cdot exp(i\Phi_{\mathrm{Ref}}(x,y))$ the off-axis hologram intensity distribution is given by:

$$I_{\mathrm{Hol}}(x,y) = |O(x,y) + R(x,y)|^2 \tag{2.3}$$

$$= O(x,y)O(x,y)^* + R(x,y)R(x,y)^* + O(x,y)R(x,y)^* + O(x,y)^*R(x,y) \tag{2.4}$$

$$= I_{\mathrm{Obj}}(x,y) + I_{\mathrm{Ref}}(x,y) + 2\sqrt{I_{\mathrm{Obj}}(x,y)I_{\mathrm{Ref}}(x,y)}\cos[\theta x + \Phi(x,y)] \tag{2.5}$$

where $\hat{O}(x,y)$ and $\hat{R}(x,y)$ represent the scalar amplitudes, $\Phi_{\mathrm{Obj}}(x,y)$ and $\Phi_{\mathrm{Ref}}(x,y)$ the phase of the objective and reference beams, * is the complex conjugate, $I_{\mathrm{Obj}}(x,y)$ and $I_{\mathrm{Ref}}(x,y)$ are the intensities of the object beam and reference beams, θ is the spatial frequency introduced by the off-axis angle α in relation to the x-axis, $\theta = 2\pi \sin(\alpha/\lambda)$, and $\Phi(x,y)$ the spatially varying phase associated with the object (phase image) [32, 33].

Over the last years, many methods for the **numerical reconstruction** of the phase images of an off-axis hologram have been established [35–37]. A prominent example is the reconstruction by Fourier transformation-based spatial filtering in the frequency domain [34]. For this purpose, the sequence shown in Figure 2.1 is applied. Here, an image of human carcinoma cells in cell culture media serves as an example. In Figure 2.1a, the off-axis hologram is shown for the whole image. After a Fast Fourier Transformation (FFT) the 2D spectrum of the image can be obtained (Figure 2.1b) including the "zero-order intensities" ($|R|^2 + |O|^2$), the image (R^*O) and the twin image (RO^*) spatially separated by an adequate off-axis angle (α). Next, a suitable spatial filter mask eliminates all components except the image (R^*O). By shifting the image (R^*O) towards the centre of the spectrum, the phase-conjugated reference wave contribution is removed (Figure 2.1c).

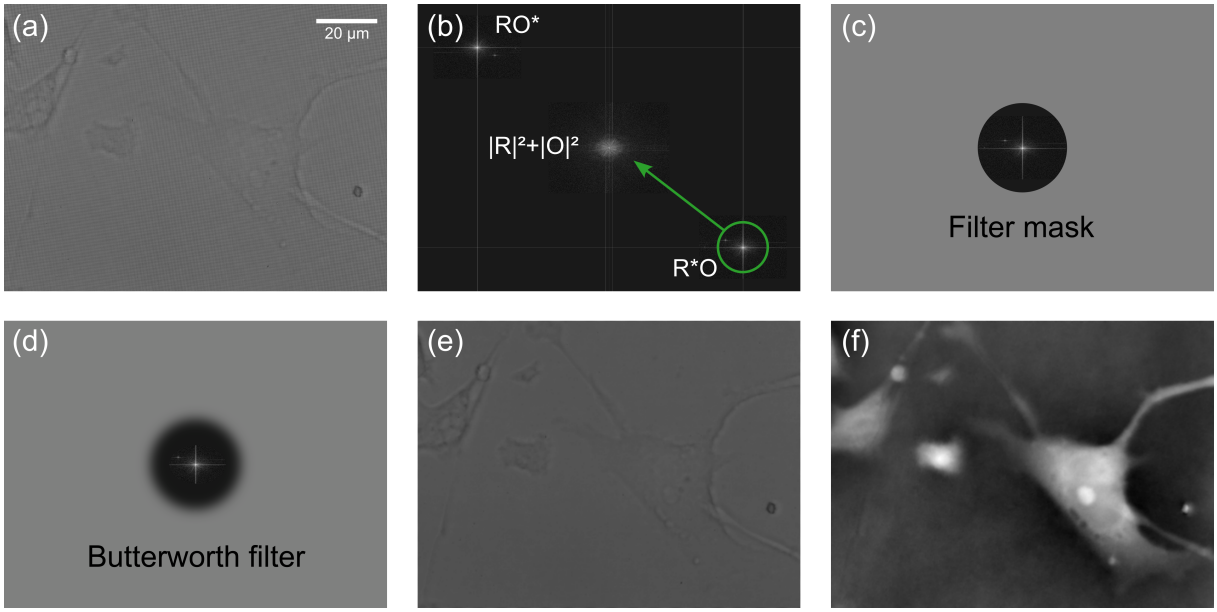

Figure 2.1: Representative images of phase and amplitude reconstruction from an off-axis hologram. **(a)** Hologram image of human carcinoma cells, **(b)** frequency spectrum of the hologram including the "zero-order intensities" ($|R|^2+|O|^2$), the image (R^*O) and the twin image (RO^*), **(c)** spatial filter to eliminate the "zero-order intensities" and the twin image with the subsequent realignment of the image in the centre, **(d)** Butterworth filtering of the frequency to enhance the image quality of the resulting amplitude image **(e)** and phase image **(f)**. Figure inspired by [34].

A Butterworth filter decreases disturbing spatial frequencies and numerical artefacts like the ringing effect (Figure 2.1d). Through an inverse FFT, the object beam (O) in the spatial domain can be determined. The resulting amplitude distribution ($\hat{O}$) is shown in Figure 2.1e. Now the phase image can be reconstructed by:

$$\Phi(x,y) = \arctan\frac{Im\{O(x,y)\}}{Re\{O(x,y)\}}(mod 2\pi) \tag{2.6}$$

After phase unwrapping, where the 2π ambiguity caused by the periodic properties of the arctangent function is eliminated, we obtain the phase image shown in Figure 2.1f. If necessary, a numerical propagation of the object beam to the image plane can be performed by:

$$O(x,y,z_{IP}) = FFT^{-1}\{FFT\{O(x,y,z_H)\}exp(i\pi\lambda\Delta z(\nu^2+\xi^2))\} \tag{2.7}$$

$$z_{\mathrm{IP}} = z_{\mathrm{H}} + \Delta z \tag{2.8}$$

where z_{IP} and z_{H} are the z-dimensions of the image plane and hologram plane, Δz is the difference, and ν and ξ represent the coordinates in the frequency domain.

Alternatively, the twin image free phase image can be obtained using a **phase shifting approach**. Here, images are received directly in the focus plane. This can be achieved by combining an in-line geometry with a temporal phase shift of the reference by $\Psi = 0, \pi/2, \pi, 3\,pi/2$ compared to the object image [38, 39]. This time the interference intensity is given by:

$$I_{\mathrm{Hol}}(x,y) = I_{\mathrm{Obj}}(x,y) + I_{\mathrm{Ref}}(x,y) + 2\sqrt{I_{\mathrm{Obj}}(x,y) I_{\mathrm{Ref}}(x,y)}\cos[\Psi + \Phi(x,y)] \tag{2.9}$$

assuming that the reference wave is a plane wave normally incident on the hologram plane, this leads to:

$$I_0(x,y) = I_{\mathrm{Obj}}(x,y) + I_{\mathrm{Ref}}(x,y) + 2\sqrt{I_{\mathrm{Obj}}(x,y) I_{\mathrm{Ref}}(x,y)}\cos[\Phi(x,y)] \tag{2.10}$$

$$I_{\pi/2}(x,y) = I_{\mathrm{Obj}}(x,y) + I_{\mathrm{Ref}}(x,y) - 2\sqrt{I_{\mathrm{Obj}}(x,y) I_{\mathrm{Ref}}(x,y)}\sin[\Phi(x,y)] \tag{2.11}$$

$$I_{\pi}(x,y) = I_{\mathrm{Obj}}(x,y) + I_{\mathrm{Ref}}(x,y) - 2\sqrt{I_{\mathrm{Obj}}(x,y) I_{\mathrm{Ref}}(x,y)}\cos[\Phi(x,y)] \tag{2.12}$$

$$I_{3\pi/2}(x,y) = I_{\mathrm{Obj}}(x,y) + I_{\mathrm{Ref}}(x,y) + 2\sqrt{I_{\mathrm{Obj}}(x,y) I_{\mathrm{Ref}}(x,y)}\sin[\Phi(x,y)] \tag{2.13}$$

A numerical combination of these equations leads to a solution that allows the reconstruction of the amplitude and the phase:

$$\hat{O}(x,y) = \frac{1}{4\hat{R}(x,y)}[(I_0(x,y) - I_{\pi}(x,y)) + i(I_{3\pi/2}(x,y) - I_{\pi/2}(x,y))] \tag{2.14}$$

$$\Phi(x,y) = \tan^{-1}\left[\frac{I_{3\pi/2}(x,y) - I_{\pi/2}(x,y)}{I_0(x,y) - I_{\pi}(x,y)}\right] \tag{2.15}$$

This technique allows a reconstruction of the whole field of view on the sensor and does not suffer from cropping in the Fourier domain like the off-axis method. Furthermore, it does not need complex computational reconstruction steps. However, the need for more than one image does not allow the measurement of moving samples. Therefore both approaches are used broadly, dependent on the application. In this work, cells in flow are measured. For this reason, the off-axis approach is the more suitable solution.

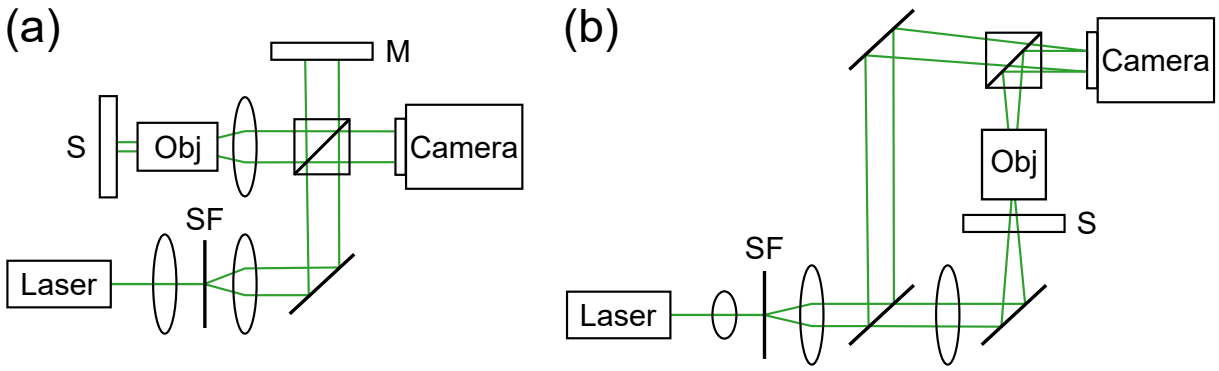

Figure 2.2: Two commonly used off-axis approaches for two beam DHM. (a) A Michelson interferometer for reflection mode and **(b)** a Mach-Zehnder interferometer for transmission mode measurements. Both setups include lenses, samples (S), objectives (Obj), spatial filters (SF), mirrors (M), cameras, and a laser. Adapted from [40].

2.1.1 Two-beam Digital Holographic Microscopy

For the off-axis approach, interference is commonly achieved using an adapted version of a Mach-Zehnder or a Michelson interferometer. The **Michelson interferometer** is used when looking at dense optical materials which do not allow a suitable amount of light transmission and therefore need to be measured in the reflection mode (Figure 2.2a). One example is the measurement of vibrations and their corresponding velocity direction of a material surface [41]. However, because cells are mostly transparent to visible light, they can be measured in the transmission mode and therefore with an **Mach-Zehnder** based approach [37, 42–44]. Here, the light of the source is divided by a beam splitter into the object beam and reference beam. The object beam passes the sample. The reference beam on the other side is aligned to contain the same propagation distance but does not interfere with the sample. Nevertheless, it also passes a similar microscope objective configuration as in the object path, resulting in a linear fringe system. This produces a less spread frequency spectrum, allowing easier image filtering after the FFT. To lower the complexity of focusing, the sample is usually mounted on a movable z-stage. Through the alignment of the two beams, they can be guided to interfere on the imaging system with an induced off-axis angle (Figure 2.2b), resulting in a full hologram. The biggest challenge in developing such a two-beam setup is the alignment of the object and reference path so that the distance is nearly the same. After a certain difference between the two paths, no more interference can be generated. This maximum difference is called coherence length (l_c) and is highly dependent on the light source, with:

$$l_\mathrm{c} = \frac{2ln(2)}{\pi n_\mathrm{m}} \frac{\lambda_0^2}{\Delta\lambda} \tag{2.16}$$

where n_m is the refractive index of the medium, λ_0 is the central wavelength, and $\Delta\lambda$ the bandwidth of the light source. Lasers are regularly used in such interferometers because

they usually have a low light source bandwidth, which achieves a high coherence length. This makes the alignment easier, but the setup remains vulnerable to external factors like mechanical vibrations. This can lead to poor temporal stability and low reproducibility of experiments.

2.1.2 Self-referencing Microscopy

An alternative to the two-beam interferometer setups are the self-referencing microscopes with a partially common path between the object beam and reference beam. This is performed by manipulating the object beam after it passes the sample to generate a quasi-reference beam. For example, a Michelson interferometer can be used to split the object beam into two individual beams. A frequency mask can manipulate one of the beams to block all higher frequencies, which mainly leaves low-frequency reference information. This quasi-reference is then interfered with the non-manipulated object part to obtain an interferogram [45].

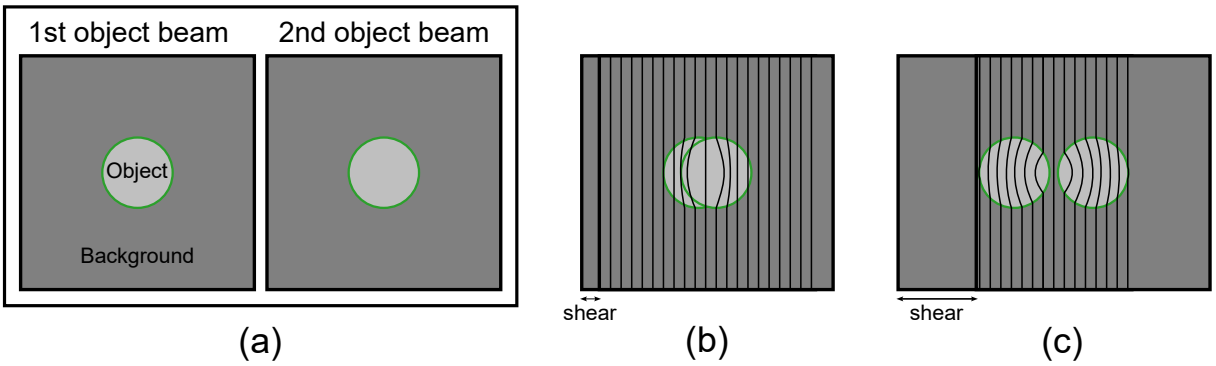

Figure 2.3: Principle of the lateral self-referencing microscopy, illustrated by using the example of a circular object. **(a)** Images from the first and second object beam. **(b)** Shear of less than the object size results in a shearogram. **(c)** Shear bigger than the object size results in a hologram. The figure was inspired by [26].

A second self-referencing technique is based on the lateral shear between the two identical object beams (Figure 2.3a). The methods to obtain two identical beams can differ and range from a complex Michelson interferometer [46] over the use of grating filters with additional optical stops [208] or by the simple use of a glass plate [26]. Regardless of the chosen method, in the second step, a lateral shear is introduced between both beams. If this shear is smaller than the size of the investigated object, a shearing interference pattern appears, which contains the gradient phase information of the object along the direction of the shear (Figure 2.3b). This is also referred to as a **shearogram**. In contrast, if the shear is bigger than the object, the modulated part of one object beam superposes with the unmodulated part of the other object beam (quasi-reference), resulting in a **hologram** (Figure 2.3c). Both techniques can be performed with a single shear in one direction but also with multiple shears in more than one direction. This directly influences the shape of

the interference patterns. A one-dimension shear produces parallel interference patterns in one direction, but a two-dimension shear produces mostly grid-shaped interference patterns.

Many self-referencing DHMs allow similar or the same image quality as the two-beam approach while retaining high temporal stability and compactness. More minor differences between the object and the quasi-reference beam also simplify the alignment so that simple LED can be used for many techniques. Those advantages allow a good on-field application. A significant drawback of the self-referencing approaches is that those who reach the image quality of the two-beam method only work with sparse object distributions. This is due to the need for a high amount of unmodulated areas which can serve as a suitable reference.

2.2 Microfluidics

Many medical diagnostic tools need to analyse high amounts of cells in a short time frame. Additionally, precise handling of specimens and reduced sample amount is desired. With the help of microfluidic devices, such challenges can be met. Microfluidics describes the dynamics of fluids in channels a few hundred micrometres in size. In this regime, surface forces dominate over volumetric forces and the flow can be described as a laminar flow. Here, the differentiation between this laminar flow and turbulent flow conditions is essential. Turbulent flow is unpredictable and chaotic. Hence it is impossible to predict the exact position of a particle as a function of time. In contrast, laminar flow describes a condition where the velocity of a particle is not random. Instead, objects can be precisely aligned by changing flow parameters such as the flow rate, the viscosity of the measurement medium, and the channel geometry. Since, in contrast to turbulent flow, laminar flow is not dominated by inertial forces but by viscous forces, contrary physical phenomena arise. Thus, two or more streams flowing in contact with each other mix in turbulent but not in the laminar regime. Here, one exception is the mixing by diffusion [47].

The **Reynolds Number** (Re) describes the quotient of inertial and viscous forces and thus whether a system is in the laminar or turbulent regime:

$$Re = \frac{\rho v_{\text{fluid}} D_{\text{h}}}{\eta} \tag{2.17}$$

where ρ is the fluidic density, v_{fluid} the characteristic velocity of the fluid, D_{h} the hydraulic diameter, and η the fluid viscosity. For rectangular channel cross-sections, the hydraulic diameter is defined as:

$$D_{\text{h}} = \frac{2hw}{h+w} \tag{2.18}$$

where h is the height and w the width of the rectangular channel. The value of $Re = 2,300$ is mostly considered as a threshold between the laminar ($Re < 2,300$) and the turbulent ($Re \geq 2,300$) regime [47, 48]. Others define $Re < 2,100$ as laminar flow, $Re > 4,000$ as turbulent flow, and everything in between as transition state [49]. Even if the exact threshold differs, values far above or below can be clearly assigned to a regime.
The **flow rate (Q)** in a microfluidic channel is only dependent on the fluidic resistance (R_F) and the pressure drop across the channel (Δp). Here, R_F can be described as:

$$R_\mathrm{F} = \frac{12\eta l}{wh^3}\left[1 - \sum_{n,odd}^{\infty} \frac{192}{n^5\pi^5}\frac{h}{w}\tanh\left(n\pi\frac{w}{2h}\right)\right]^{-1} \tag{2.19}$$

resulting in:

$$Q = \frac{\Delta p}{R_\mathrm{F}} = \frac{\Delta p w h^3}{12\eta l}\left[1 - \sum_{n,odd}^{\infty} \frac{192}{n^5\pi^5}\frac{h}{w}\tanh\left(n\pi\frac{w}{2h}\right)\right] \tag{2.20}$$

where l is the length of the channel. Additionally, the velocity of a single particle in such a fluidic system in flow direction x is defined by:

$$v_x(y,z) = \frac{4\Delta p h^2}{\pi^3\eta l}\sum_{n,odd}^{\infty}\left[1 - \frac{\cosh\left(n\pi\frac{y}{h}\right)}{\cosh\left(n\pi\frac{w}{2h}\right)}\right]\sin\left(n\pi\frac{z}{h}\right) \tag{2.21}$$

where y is the lateral position of the particle in the channel, and z is the analytic midpoint. By substituting the equation into equation 2.20, the particle velocity can be determined as a function of the flow rate:

$$v_x(y,z) = \frac{48Q}{\pi^3 h w}\frac{\sum_{n,odd}^{\infty}\left[1 - \frac{\cosh\left(n\pi\frac{y}{h}\right)}{\cosh\left(n\pi\frac{w}{2h}\right)}\right]\sin\left(n\pi\frac{z}{h}\right)}{1 - \sum_{n,odd}^{\infty}\frac{192}{n^5\pi^5}\frac{h}{w}\tanh\left(n\pi\frac{w}{2h}\right)} \tag{2.22}$$

Most of the equations mentioned here apply only if the particle surrounding media in the channel has a constant viscosity [50]. This assumption is always given for so-called **Newtonian fluids**. Other fluids, however, change their viscosity dependent on the applied shear rate. One group of liquids contains large deformable particles that can be stretched out at high shear rate values leading to a decrease in viscosity. Another group of liquids

can contain small particles with strong interactions between each other. Those interactions can hinder the flow at an increased shear rate, leading to an increase in viscosity. Here, shear rate ($\dot{\gamma}$) is defined by the velocity gradient:

$$\dot{\gamma} = \frac{\partial v}{\partial z} \tag{2.23}$$

Fluids that express a lower viscosity at a higher shear rate are called shear-thinning. The contrary group is called shear-thickening:

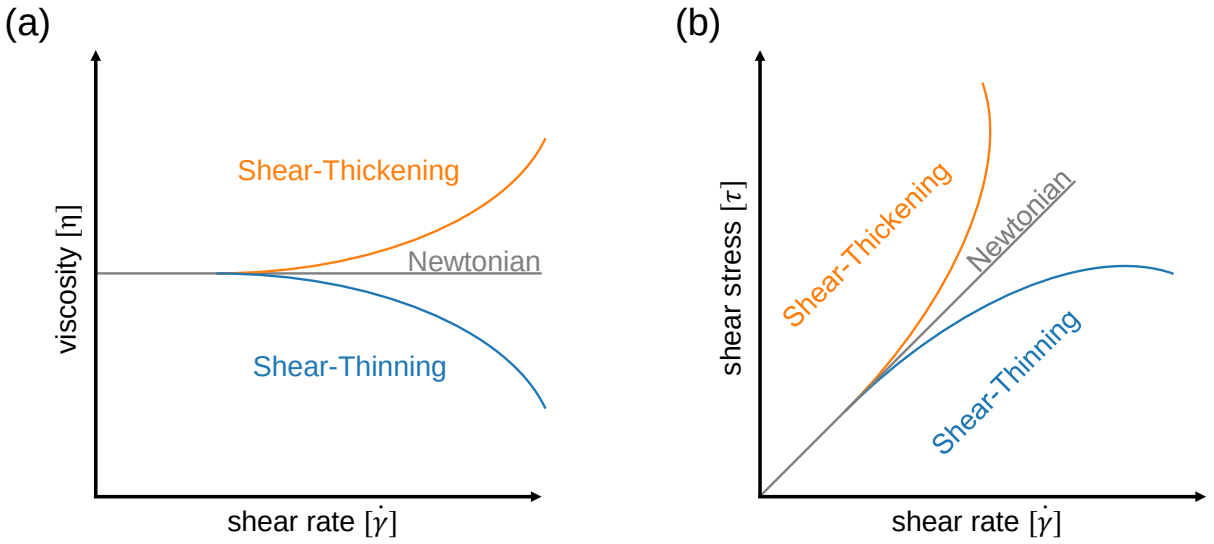

Figure 2.4: Differences for Newtonian, shear-thickening, and shear-thinning liquids. Illustrated by the comparison between **(a)** shear rate and viscosity as well as **(b)** shear rate and shear stress.

As shown in Figure 2.4b, the different groups can also be classified by the relationship between shear rate ($\dot{\gamma}$) and shear stress(τ) [51]. Here, the shear stress is dependent on the shear rate and the viscosity:

$$\tau = \eta\dot{\gamma} = \eta\frac{\partial v}{\partial z} \tag{2.24}$$

For rectangular channel geometries with $h << w$, the wall shear stress is given by [52]:

$$\tau = \eta\frac{6Q}{h^2 w} \tag{2.25}$$

In Newtonian fluids, the drag and lift force are the **two dominant forces** acting on a particle in a microfluidic channel. The drag force arises due to the velocity difference

between a particle and the surrounding liquid and is always in the direction of particle flow. Strokes drag law describes the force for low Reynolds numbers as:

$$F_{\text{drag}} = 6\pi\eta a_{\text{P}}(v_{\text{fluid}} - v_{\text{P}}) \tag{2.26}$$

where a_{P} is the particle radius and v_{P} the particle velocity [53]. The total lift force acting on a particle (F_{lift}) is the sum of the wall-induced lift (F_{W}), the shear-gradient lift (F_{S}), the slip-shear lift (F_{SS}), and the correction of the shear-gradient-induced lift (F_{C}). Since the effects of F_{SS} and F_{C} are significantly smaller compared to the other two, the total inertial lift force can be formulated as:

$$F_{\text{lift}} = F_{\text{W}} + F_{\text{S}} = \frac{\rho v_{\text{fmean}}^2 a_{\text{P}}^4}{D_{\text{h}}^2} C_{\text{IL}} \tag{2.27}$$

$$C_{\text{IL}} = \dot{\gamma}^2 G_1 + \dot{\gamma}\beta G_2 \tag{2.28}$$

where, v_{fmean} is the mean velocity of the fluid, C_{IL} is the inertial lift coefficient, G_1 and G_2 are functions of the lateral position, and β is the dimensionless shear gradient [54]. The wall-induced lift force is a lateral force in the direction of the channel centre, whereas the shear-gradient lift force is a lateral force in the direction of the channel walls. However, these forces are not constant throughout their lateral position. Near the channel border, F_{W} is the prevailing force and near the channel centre, F_{S} is dominating. A balance between the different lift forces and the drag force results in the inertial focusing of particles in equilibrium lines. For rectangular channels, there are two focus positions, for a square, there are four, and for a circular geometry, there are many distributed with the same radius around the centre [55, 56].

An additional force is needed to focus particles from those equilibrium positions towards one position in the centre of the channel. One example of that is the introduction of the **viscoelastic force (F_E)** by using non-Newtonian polymer solutions [57]. The viscoelastic effect in the liquids can be quantified with the non-dimensional Weissenberg number (Wi), which is the ratio of the elastic force to the viscous force. For channel dimensions with $w < h$, the equation is given as:

$$Wi = \lambda_{\text{t}}\dot{\gamma} = \lambda_{\text{t}}\frac{2Q}{hw^2} \tag{2.29}$$

where λ_{t} is the relaxation time of the fluid. When $Wi >> 1$, the viscoelastic effect becomes significant. In pure viscoelastic flows, particles tend to migrate to lower shear rate regions, which is in the case of a rectangular channel either in the corners or in

the centre plane. In detail, particle migration is due to the non-uniform normal stress differences like the first (N_1) and the second (N_2) normal stress differences [58]. For most polymer solutions, the effects of N_1 are dominant, wherefore other stress differences can be neglected [59]. Therefore the viscoelastic force is formulated as:

$$F_{\mathrm{E}} = C_{\mathrm{EL}} d_{\mathrm{P}}^3 \nabla N_1 = -2 C_{\mathrm{EL}} d_{\mathrm{P}}^3 \lambda_{\mathrm{t}} \eta \nabla \dot{\gamma}^2 \tag{2.30}$$

where C_{EL} is the dimensionless elastic lift coefficient and d_{P} is the particle diameter. Similar to the lift forces, also the viscoelastic force acts on the particle in the lateral direction. Stress differences in a microfluidic channel are more dominant around the channel border regions than in the centre. Therefore also F_{E} is greatest at the channel borders and decreases gradually until the centre of the channel.

Furthermore, liquids and particles can also be focused in fluids by **hydrodynamic focusing**. This principle occurs for systems with low Re when two streams are introduced into a straight microfluidic channel, flowing side-by-side along the channel. When the fluids match in both viscosity and hydrophobicity, no mixing occurs until a certain length when diffusion becomes dominant. Now, if one of the two flows has a higher flow rate than the other, a redirection of the slower stream by the faster one takes place. The width of the stream in a system with two parallel streams is defined by:

$$w_{\mathrm{A}} = w \frac{Q_{\mathrm{A}}}{Q_{\mathrm{A}} + Q_{\mathrm{B}}} \tag{2.31}$$

where w_{A} is the width of the flow A, Q_{A} is the flow rate of input A, and Q_{B} is the flow rate of input B [60].

The introduction of multiple streams in one microfluidic channel not only allows the manipulation of fluids for focusing but can also be used to create so-called droplets. This principle is based on strong interfacial and viscous forces between two fluids initialised by suitable channel geometries [61]. The corresponding subsection of microfluidics is often referred to as **droplet microfluidics**. Droplets consist of two immiscible fluids, one on the inside and the other on the outside. One of the two fluids, the so-called carrier phase, splits the disperse phase into discrete bundles to create droplets. Two regularly used fluids due to their inherent properties are deionised water and mineral oil. The resulting droplets are called water-in-oil-droplets for geometries where mineral oil serves as a continuous phase and deionised water as disperse phase. Here it should be noted that a surfactant can be used to create a stable emulsion and also helps the droplet generation by reducing the interfacial tension between both phases. Furthermore, for a stable generation of droplets without the adherence to the channel walls, the channel walls need to have the same properties as the continuous phase regarding hydrophilicity and hydrophobicity. Many geometries can be used for droplet generation like the T-junction [62], the co-flow structure [63], and the flow-focusing structure [64]. The following explains droplet creation

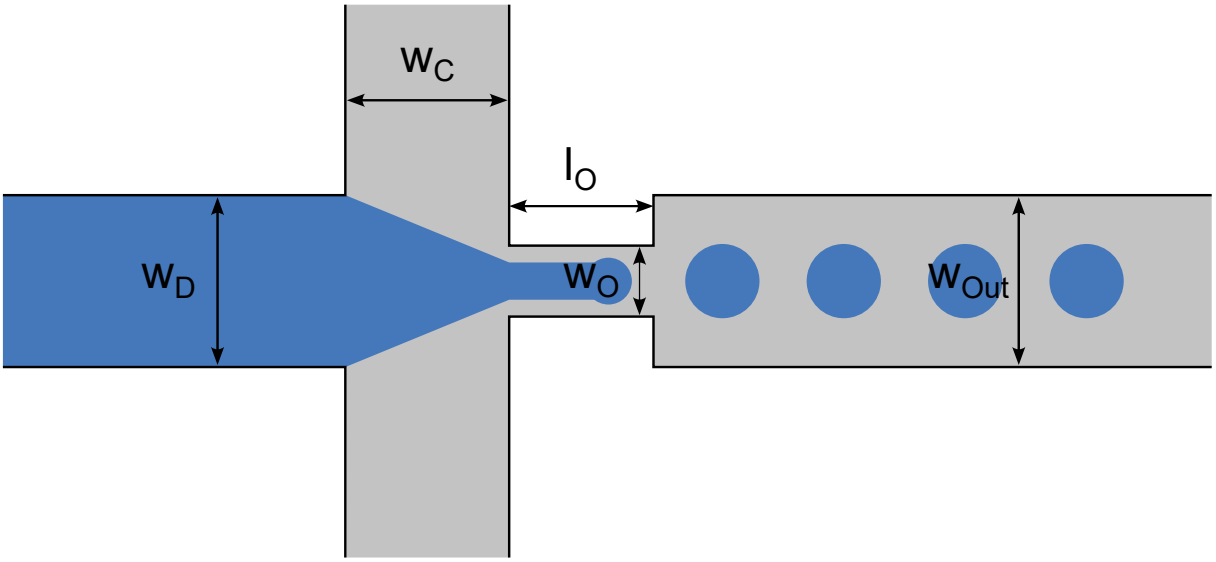

Figure 2.5: Principle of droplet generation in a flow-focusing geometry. The setup includes one disperse phase with the width w_{D}, two continuous phases with the width w_{C}, an orifice with a width w_{O} and a length l_{O}, and an outlet with a width w_{Out}. The height h is not shown.

with the example of flow-focusing structures. The geometry of this principle is based on the previously described hydrodynamic focusing.

In a flow-focusing geometry, as shown in Figure 2.5, the disperse phase enters the junction perpendicularly to the two continuous phases, resulting in three inlets. In many variations, the beginning of the outlet is narrower than the rest. This section is called orifice and can be adjusted through the width w_{O} and the length l_{O}. Additionally, the width of the disperse phases w_{D}, of the continuous phase w_{C}, and the outlet w_{Out} as well as the flow rates of the disperse phase Q_{D} and continuous phase Q_{C} influence the droplet creation. The capillary number is essential to characterise the generated droplets and the prevailing flow regime. It describes the relationship between viscous forces and interfacial tension forces and is defined as:

$$Ca = \frac{\eta v_{\mathrm{fluid}}}{\sigma} \tag{2.32}$$

where σ is the surface tension. The flow-focusing design is not yet fully mathematically described. However, there are some approaches like from Anna and Mayer [65], where they propose a definition of the capillary number as:

$$Ca = \frac{\mu_{\mathrm{C}} Q_{\mathrm{C}} w_{\mathrm{D}}}{2\sigma h w_{\mathrm{C}}} \left(\frac{1}{w_{\mathrm{O}}} - \frac{1}{2w_{\mathrm{C}}} \right) \tag{2.33}$$

where μ_C and Q_C are the viscosity and flow rate of the continuous phase. Furthermore, Lee et al. proclaim, based on this definition, that for moderate capillary numbers, the diameter of a droplet can be estimated as [66]:

$$d_{\text{Droplet}} \propto Ca^{-1/3} \tag{2.34}$$

Additionally, empirical studies like Lashkaripour et al. [67] showed that the orifice width has the most significant influence on the droplet diameter for almost all capillary numbers. This is followed by the channel height, the normalised width of the outlet channel, the width of the continuous phase, the orifice length, and the flow rate ratio between the continuous and disperse phases.

2.3 Haemostasis

In this work, the phase imaging flow cytometer is used to characterise temporal dynamics in processes such as blood cell aggregate formation and decay. For this purpose, it is essential to understand the underlying mechanisms in human physiology. In this chapter, the basic mechanisms of haemostasis are explained. Haemostasis includes processes that, on the one side, stop an extended blood loss through the formation of fibrin clots. On the other hand, it should regulate this formation to prevent excessive thrombus generation, which can lead to vascular occlusion [68]. Platelets are highly relevant for the coagulation dynamics described by the so-called coagulation cascade. With anticoagulants, the coagulation can be stopped temporally or even irreversibly. When looking at blood cell aggregates, not only the interplay between platelets is relevant, but also the specific interaction with different subtypes of leukocytes.

2.3.1 Platelets

Platelets are generated through the decay of megakaryocytes. Depending on the surrounding media and other influencing variables, they can be either in their physiological state, also known as the unactivated state, or in an activated form. In their physiological condition, they have a diameter of $1 - 4\,\mu\text{m}$, which results in a surface area of $8\,\mu\text{m}^2$. In the activated stage the size changes and surface areas of $13\,\mu\text{m}^2$ were observed. Platelets circulate in the blood at a concentration of $150 - 300 \times 10^3\,\mu\text{L}^{-1}$ and are mainly concentrated near the vessel walls. This, together with their surface morphology, leads to a close contact of platelets with the endothelium of the blood vessels. The activation of platelets, describing the process from physiological to the activated state, usually happens through an antagonist like **Adenosine Diphosphate (ADP)** or **thrombin** or through the adhesion at the vessel subendothelium, which can occur in the case of a damaged vessel wall. This leads to a morphological shape change and an expression of receptors on the cell surface. There are several interactions and bindings of the different platelet receptors.

First, the interaction between the **von-Willebrand-factor** on the subendothelium and the glycoprotein Ib-V-IX-receptor at the platelet surface. A stabilization of the platelet-subendothelium-connection occurs through the binding of other proteins like collagen, fibronectin, and laminin. The activated platelet now releases thromboxane A2 and ADP, which binds on the corresponding surface receptors of the platelets. This increases both the activation and the adhesion. Furthermore, a vasoconstriction is promoted by thromboxane A2 leading to a better thrombus formation by a reduced blood flow. A connection between different platelets occurs due to the expressed GpIIb-IIIa-receptors on their surface and the connecting fibrinogen. This connection is highly dependent on the presence of calcium ions. However, the resulting Platelet Aggregate (P-Aggregate) is relatively unstable compared to fully evolved thrombi [68].

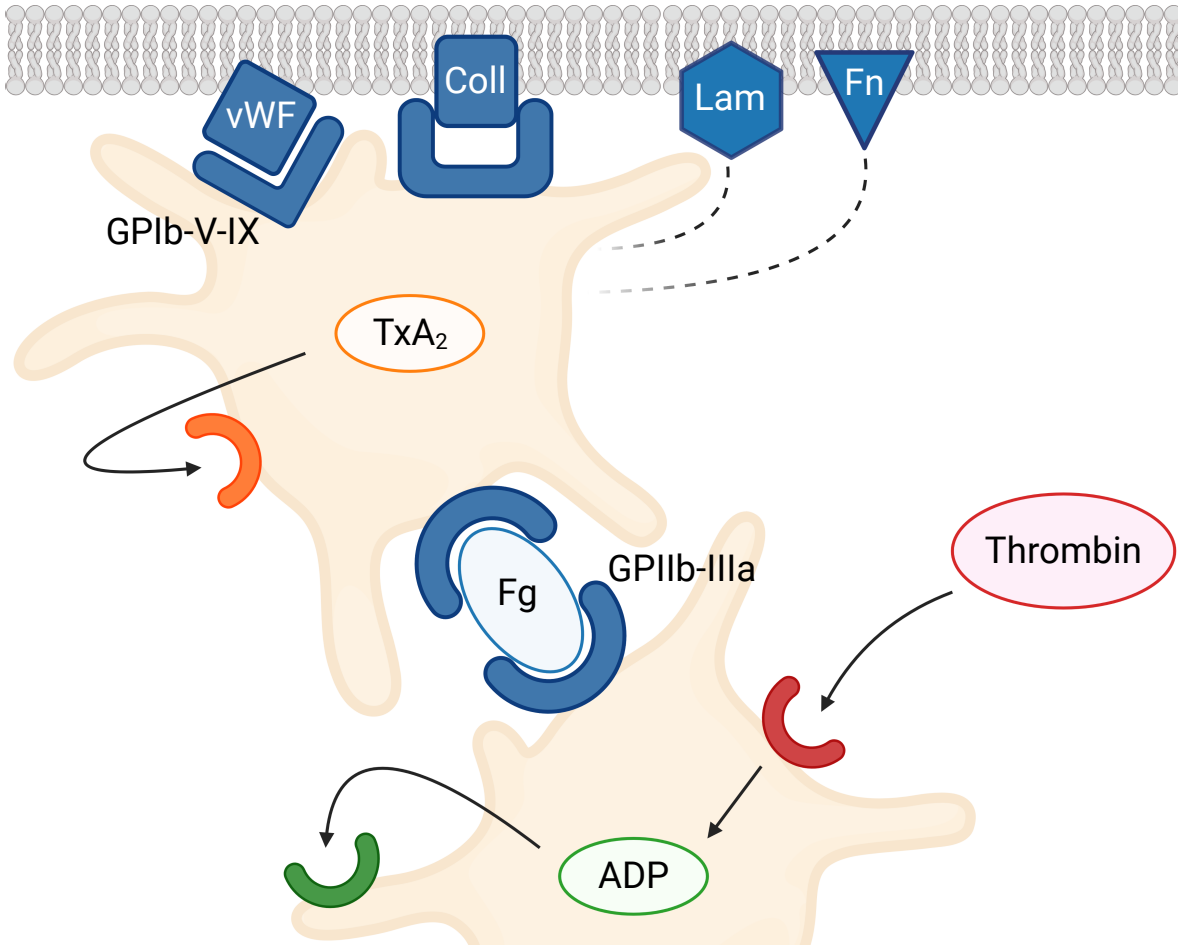

Figure 2.6: Platelet activation and aggregation. Platelet interaction with proteins of the subendothelium like the von-Willebrand-factor (vWF), collagen (Coll), fibronectin (Fn), and laminin (Lam) stabilizes the platelet-subendothelium-connection and strengthens the activation process. The process is driven by thromboxane A2 (TxA_2) and ADP and can be further supported by thrombin. Fibrinogen (Fg) serves as a connector between the GpIIb-IIIa-receptors of different platelets. Figure was adapted from [68] and created with biorender.com.

2.3.2 Coagulation Cascade

The coagulation cascade is a sequence of events that leads to haemostasis. This sequence involves the interplay and activation of different coagulation factors. There are two different starting strands of coagulation, the extrinsic and intrinsic pathways. The **intrinsic pathway** gets activated through the contact of plasma factors (XII and XI) with the negatively charged matrix of the subendothelium. Additionally, factor IX gets activated to IXa, subsequently leading to the activation of factor X which marks the common pathway with the extrinsic pathway. The activation of the **extrinsic pathway** is initialised by an injury of the tissue wall followed by an exposure of the tissue factor. Together with the Factor VII present in plasma, this results in the most efficient coagulation activator. This complex then activates factor X, also resulting in the common pathway. The extrinsic pathway is more efficient and way faster than the intrinsic pathway. The tissue factor is present in high concentrations in organs where bleeding is a serious risk to life (e.g., heart, kidney, and brain). The **common pathway** describes, among others, two important complexes. The prothrombinase complex describes the catalysis of prothrombin (II) into thrombin (IIa) by the involvement of Ca^{2+} ions, the platelet factor (Pf3), and factor Va and Xa. This process, like the activation of X to Xa and IX to IXa, takes place at the platelet membrane. Thrombin is needed to activate fibrinogen (I) into fibrin (Ia) and factor XIII to XIIIa. Finally, long fibrin fibres are formed from fibrinogen, resulting in a fibrin network cross-linked by factor XIIIa. This network is the end product of the coagulation cascade, can stabilise clots, and has sufficient resistance to enzymatic lysis by plasmin. [68–70]

2.3.3 Anticoagulants and Agonists

Within minutes after being drawn, blood starts with the coagulation process. This effect can be driven by temperature change, high shear rates, or other influencing variables [71]. However, many blood tests depend on single cell measurement, so this behaviour could present a major challenge in the field of in-vitro blood diagnostics [72]. This problem is addressed by using chemicals, which inactivate or bind to certain coagulation factors resulting in a disturbed blood coagulation. Four common agents used in the clinical routine are heparin, hirudin, citrate, and Ethylene Diamine Tetraacetic Acid (EDTA). These **anticoagulants** have different mechanisms of action. EDTA strongly chelates Ca^{2+} and Mg^{2+} ions. This results in a blockage of many steps in coagulation complexes and in the platelet aggregation process. Similar to EDTA, also citrate binds to Ca^{2+} and Mg^{2+} ions but with a lower strength. Both anticoagulation processes are reversible by adding calcium and/or magnesium to the sample. Heparin binds to antithrombin through a high-affinity pentasaccharide [73]. This complex then irreversible connects to prothrombin, inhibiting the formation of thrombin as well as the factors Xa, IXa, XIa, and XIIa in an irreversible manner. Hirudin is a peptide with 65 amino acids, providing potent thrombin inhibition [74]. By forming a tight and irreversible bond with it, thrombin gets inactivated. As a result, fibrinogen clotting, thrombin-induces platelet activation, and the activation of clotting factors V, VIII, and XIII are blocked.

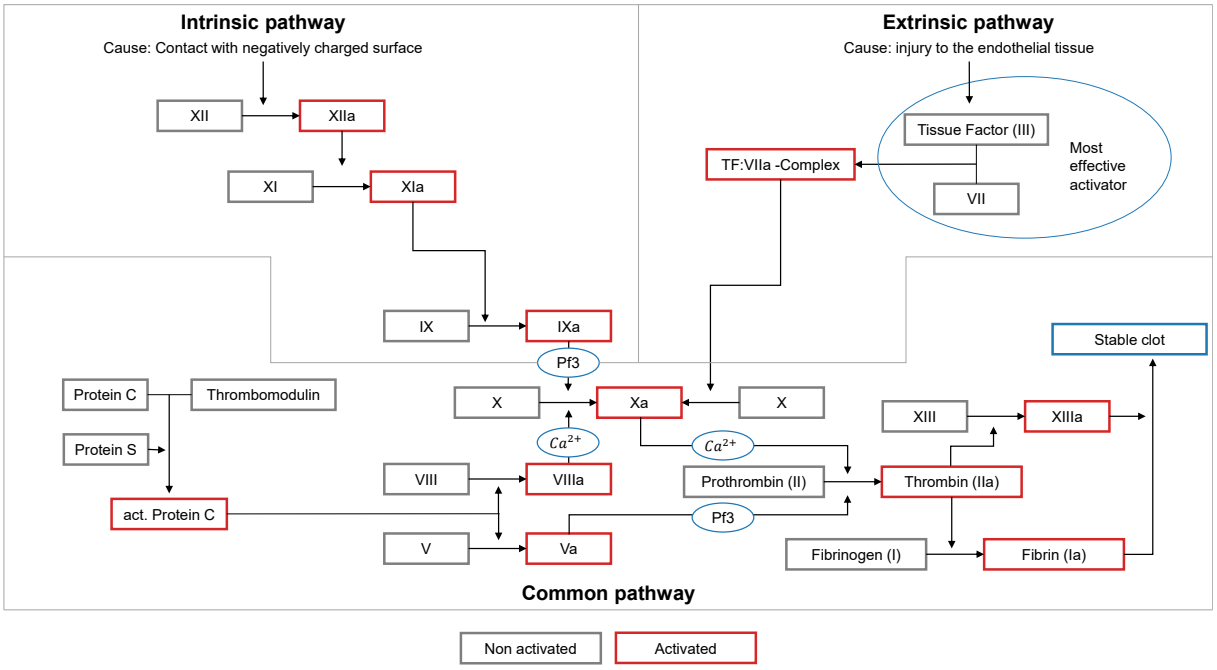

Figure 2.7: Interaction of the different coagulation factors into the coagulation cascade. The intrinsic, extrinsic, and common pathways have been drawn in individual areas for clarity. The filled colours indicate where the respective substance is present, and the border indicates whether the factor is activated or non-activated. Figure was adapted from [68–70].

In addition to direct coagulation of blood after collection, it can also be activated by the addition of **activating agonists** such as ADP and Thrombin Receptor Activating Peptide (TRAP). ADP activates the platelet receptors P2Y12 and P2Y1 what supports further ADP secretion out of the granula after activation [75]. Therefore, ADP results in a positive feedback loop. In contrast, TRAP binds to different protease-activated receptors of the platelets like PAR1 and PAR3, which triggers platelet secretion and aggregation [76].

By using such substances, dynamics in patients' blood coagulation can be determined. For such activation assays, the agonists are added to the blood sample, which initialises the clotting process. Next to the time until a part or the full sample is coagulated, also dynamics in the process are analysed. This can be achieved by a mechanical [77] or impedance [78] measurement method. In such assays, it could be shown that some anticoagulants allow a subsequent platelet activation and others do not. Hirudin, heparin, and citrate are regularly used in in-vitro assays because they allow blood coagulation after initial activation with the agonists [79]. EDTA on the other side inhibits the formation of aggregates through the prevented interaction between fibrinogen and the exposed receptors on the platelet membranes [80].

2.3.4 Blood Cell Aggregates

Platelets play an essential role in haemostasis and close vessel injuries by forming aggregates and clots. But platelets can not only specifically bind to each other or the subendothelium but also to leukocytes. Platelet aggregation and the accompanying degranulation allow for association with leukocytes through interactions of various receptors [81]. On the side of the platelets, two prominent examples are P-selectin (CD62P) and CD40 Ligands (CD40L), which are both presented at the surface after platelet activation. For Leukocytes, CD40 and P-selectin glycoprotein ligand-1 (PSGL-1) are important receptors that have a high binding affinity with CD40L and CD62P, respectively. Those connections are then further stabilised by other receptors [82, 83]. This, however, triggers further processes that support platelet and leukocyte activation. It has also been shown that this connection leads to a release of neutrophil extracellular traps (NETs) [84, 85], strengthens leukocyte recruitment [86], and promotes the release of pro-inflammatory mediators by the leukocytes [87, 88]. Using the example of Leukocyte-Platelet Aggregate (LP-Aggregate)s, it could be shown that the formation of aggregates not only represents a preliminary stage of blood coagulation after an injury of the endothelium but also occur specific to inflammatory and infectious processes. Aggregates have been detected in bacterial and viral diseases of the liver [85, 89], kidney [90, 91], and lung [92, 93] as well as in cardiovascular disorders [94, 95]. However, the exact composition of LP-Aggregates differs according to the type of disease. P-Aggregates and their appearance in clinical disorders are lesser investigated due to more limited measurement methods. Nevertheless, they could be observed, for example, in patients with arterial insufficiencies [96] and in infections of the lungs [97]. This could indicate that blood cell aggregates are a potential marker for various diseases [81].

2.4 COVID-19

Coronavirus disease 2019 (COVID-19) is the clinical manifestation caused by Severe Acute Respiratory Syndrome Coronavirus 2 (SARS-CoV-2). It ranges from asymptomatic infections to a life-threatening diseases, whereby Acute Respiratory Distress Syndrome (ARDS) and multi-organ failure can occur. Such serious complications can be partially prevented by treating vulnerable patients with suitable drugs [98] or methods such as the Extracorporeal Membrane Oxygenation (ECMO) [99]. Still, diagnostic tools are needed to understand the progression of the disease. One key mechanism of COVID-19 is the COVID-19-Associated Coagulopathy (CAC), which manifests in micro- and macrothrombi. This can subsequently lead to multi-organ injury and failure. CAC has not been completely understood when looking at the underlying cellular and molecular mechanisms. Still, many pieces of evidence suggest that it is driven by dysregulated immunothrombosis, which is a complex interplay between the coagulation cascade, white blood cells, platelets, fibrinolytic pathways, and the vascular endothelium [100–103]. The hyperinflammatory immune response combined with hypercoagulability and vascular endothelial cell dysfunction results in the clinical phenotype of COVID-19, which is linked to

patient morbidity and mortality [103–105]. Many clinical biomarkers have been analysed and combined for the longitudinal measurement of the patient's health status and a possible prediction of the severity status. Two prominent examples that showed promising links to disease severity, mortality, and thromboembolic complications are plasma levels of D-dimers [106] and the C-reactive protein (CRP)[107, 108]. However, the relevance of both markers for clinical management including anticoagulation, requires further investigation [107, 109, 110]. Furthermore, while many other possible markers were investigated, hardly any has been translated into clinical practice [111, 112]. Next to insufficient prospective validation, inaccuracy of the biomarker, complex workflows, and economic reasons, there are many more reasons for their discrepancy [113–115]. Many of these biomarkers try to detect resulting products of the CAC. These can occur in many manifestations depending on the pathological platelet hyperactivation. To name some, platelets have a higher microvesicle, granule, cytokine, and chemokine release and more frequently tend to undergo apoptosis. Additionally, increased amounts of P-Aggregates and LP-Aggregates have been detected in COVID-19 patients that could be linked with disease severity. This includes platelet-monocyte and platelet-neutrophil aggregates [116–118].

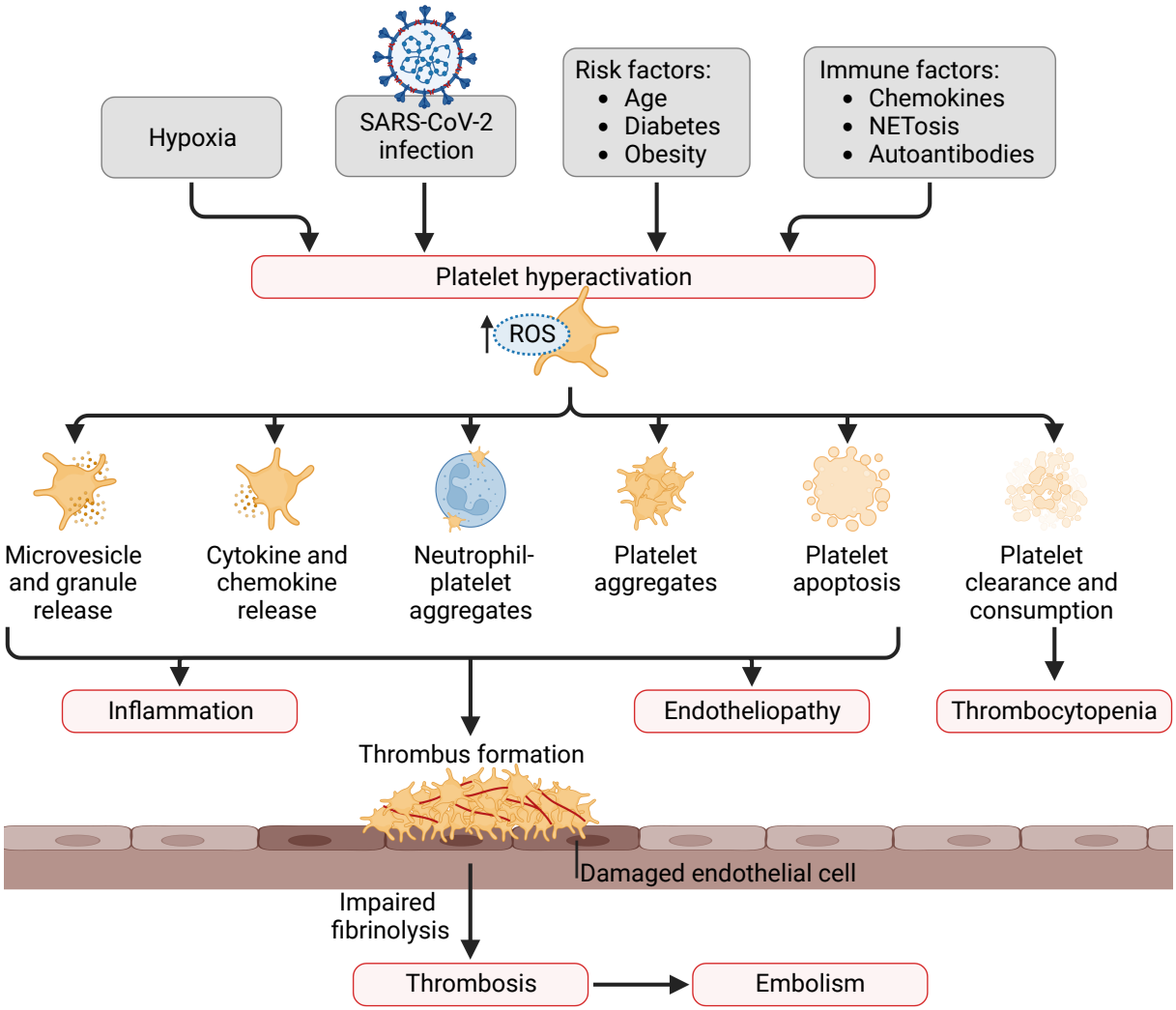

Figure 2.8: Impact of the COVID-19-associated coagulopathy on the physiological platelet response. Inducers like old age, obesity, diabetes mellitus, and hypoxia due to a previous illness in combination with a SARS-COV-2 infection lead to increased intracellular levels of Reactive Oxygen Species (ROS), which subsequently results in hyperactivation of platelets. This leads to a higher release of microvesicles, granules, cytokines, and chemokines. A supplementary higher platelet aggregation to other platelets and specific bindings to certain leukocytes combined with a high platelet apoptosis results in a bigger platelet consumption. A parallel combination of all mentioned physiological responses simultaneously leads to increased thrombosis and inflammation, which can end in life-threatening thromboembolism. In COVID-19 patients, the lungs are predominantly affected, but these events can also occur in other organs, like the heart, kidneys, and liver. The figure was adapted from [119] and created with BioRender.com.

3 From a Laboratory Prototype towards a Medical Technology Device

3.1 Motivation and Problem Statement

In previous work, the interplay of a DHM with a microfluidic chip and downstream image analysis was used to differentiate between different types of leukaemia and detect infected red blood cells [22, 23]. For this, single blood cells were analysed based on morphological features such as a cell's diameter or maximum phase shift. However, several further steps are required to obtain a clinically relevant haematology device. First, an improvement of the components of the analyser is needed to meet the requirements of various medical questions. This includes a reproducible high amount of focused cells provided by the microfluidic system. Because smaller particles are more difficult to focus than bigger objects (chapter 2.2), a high amount of unfocused cells can lead to a loss of small cells and, subsequently, to wrong cell ratios. This not only lowers the precision of the device but can also lead to misdiagnosis [120, 121]. In addition to the hardware, the image analysis needs to be adjusted to fulfil new requirements like the detection of cell aggregates. Furthermore, for many clinical decisions, blood cell concentration measurements are highly important [122, 123]. Therefore, new analysers need to include this functionality to show established laboratory values for the experts and allow a comparison of different methods. Furthermore, the stability and reliability of the measurements must be ensured for each sample. This can be met by introducing a calibrator system and an in-depth analysis of possible influences on the blood cells. Finally, the label-free approach of DHM has limited discrimination power for cells with similar morphological properties. This is true for some leukocytes, such as B- and T-Cells. In fluorescence flow cytometry, this problem is tackled by specific marker-cell interactions, allowing sub-typing of leukocytes as long as there are suitable antibodies [124]. This led to the development of hybrid systems containing both a DHM and a fluorescent sensor unit [125, 126]. However, this has the disadvantage of an increased optical system complexity and the necessity of expensive fluorescent markers. An alternative approach for optical systems is using beads coated with antibodies, which also allows a specific bead-cell interaction. This was already shown for other imaging methods, especially for cell sorting [127, 128].

Another major step towards a medical technology device is the automation of the system. This drastically reduces inter-observer variabilities and allows a more simplified measurement procedure. Especially for large studies or multicenter approaches, such automated workflows are essential. Therefore, an overview of the applied automation steps is shown in chapter A.2.

3.2 Methodology

The measurement system used in this work comprises a DHM, a microfluidic system, and subsequent image analysis. This methodology chapter explains all these single components and their interplay in depth. For microfluidic focusing, different polymers were evaluated for suitability as viscoelastic focusing materials and how they interact with blood cells. Furthermore, used sample preparation steps for the extraction of leukocytes and the sphering of erythrocytes are explained. Finally, the necessary steps for labeling leukocytes with microbeads and using a Finite Element Method (FEM) to simulate the properties of the microfluidic channel are described.

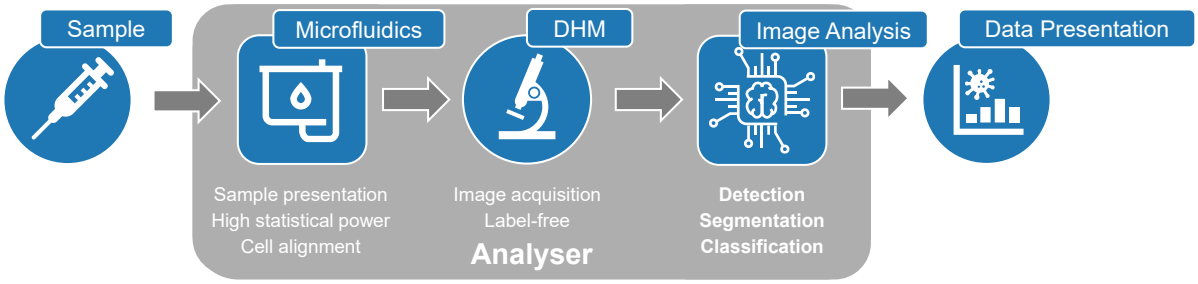

Figure 3.1: Workflow of the measurement system. A microfluidic module allows the measurement of high amount of sample material while aligning the cells in one horizontal plane. The usage of DHM provides phase-contrast images without the need for labeling. The subsequent image analysis detects and segments single elements in an image and allows cell classification.

3.2.1 Optical Setup

A customized transmission DHM developed with Ovizio Imaging System was used for image acquisition. This device combines an off-axis approach for interference with a self-referencing technique based on the shearing of the object beam. A SLED from Osram with a wavelength of $\lambda = 528\,\text{nm}$ in combination with a Koehler illumination unit was used as a light source. Light passes the sample toward the objective, which has a 40× magnification and a 0.55 numeric aperture (CFI LWD, Nikon). The numeric aperture was chosen to be a compromise between a moderate axial and lateral resolution. According to Max Berek, the axial resolution (Depth-of-Field (DOF)) is defined as:

$$DOF = DOF_{\text{Wave}} + DOF_{\text{Geometry}} = \frac{\lambda n_{\text{ML}}}{NA^2} + \frac{n_{\text{ML}}}{mNA} \cdot p_{\text{Sens}} \tag{3.1}$$

where DOF_{Wave} and DOF_{Geometry} are the wave and geometrical optical depth of fields, n_{ML} is the refractive index between medium and lens, NA is the numeric aperture of the light collecting optics, m is the magnification, and p_{Sens} the pixel size of the sensor.

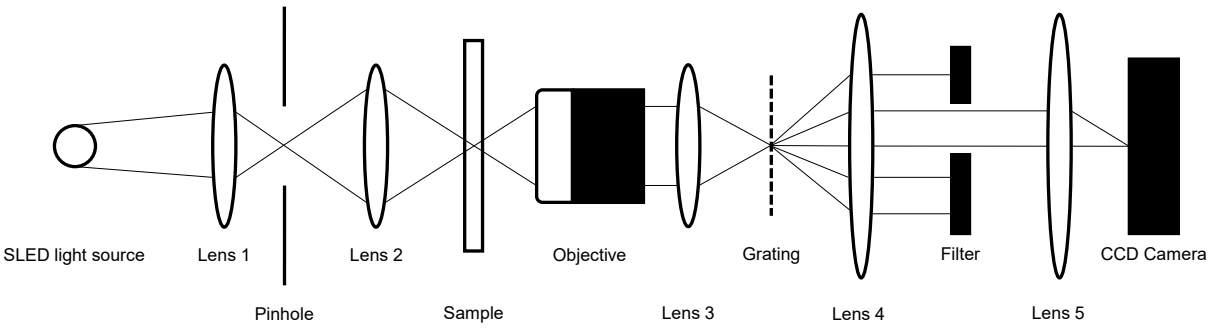

Figure 3.2: Optical components and pathways of the used self-referencing DHM. The microscope is built of a SLED with a wavelength of $\lambda = 528\,\text{nm}$, lenses for beam alignment, a grating filter for diffraction of the object beam, a spatial filter to obtain desired maxima, and a CCD camera for image acquisition. The self-referencing shearing approach is obtained after the beam passes the sample through diffraction, filtering into zero and first maxima, and a subsequent sheared interference.

The lateral resolution (d) is defined by the Rayleigh criterion by:

$$d = \frac{1.22\lambda}{2NA} \tag{3.2}$$

While a high numeric aperture improves lateral resolution, it decreases the DOF, which is especially important for analysing bigger cells.

Different shears are created by a grating of the object beam, resulting in a two-dimensional diffraction pattern. The spatial filter eliminates all maxima except the zero-order maximum and the first-order maxima in both the x and y direction. With an off-axis angle α, the zero-order maximum interferes with the first-order maxima in the x and y direction. Here, a shear in their respective direction is introduced on both first-order maxima to obtain a quasi-reference. Thus, a hologram is created where phase and amplitude information can be reconstructed by eliminating zero-order intensities and the twin image (Figure 2.1). Images are recorded with a frame rate of 105 frames per second at a exposure time of 5 µs using a GS3-U3- 32S4M camera (Teledyne FLIR LLC). For the recording and reconstruction, the software Os-One Version 5.12.12 (Ovizio Imaging Systems) was used. Dependent on the requirements, between $7,500 - 15,000$ images per capture were recorded.

3.2.2 Microfluidic Design

A high throughput sample measurement with a precise blood cell alignment was achieved by combining the DHM with a microfluidic system. Here, a Polymethylmethacrylate (PMMA) from Fraunhofer IMM was used as material for the 500 µm wide, 50 µm high and

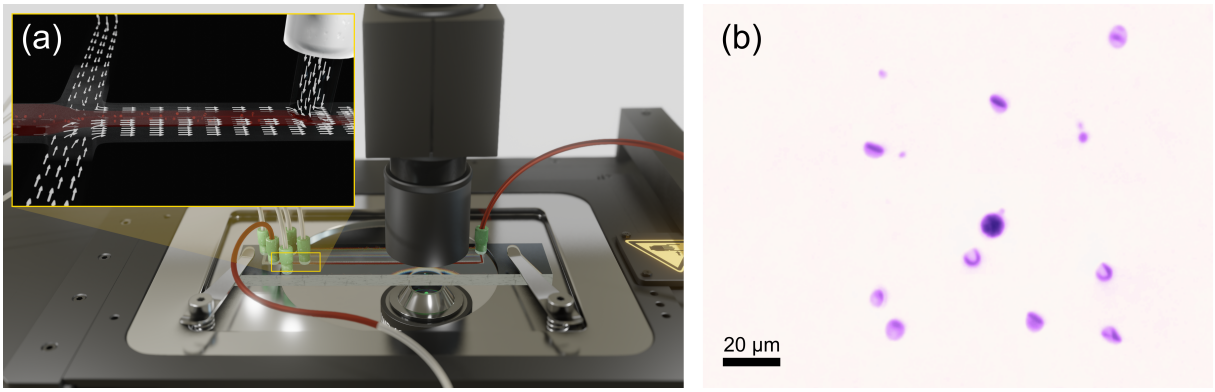

Figure 3.3: Microfluidic system for cell alignment. **(a)** Schematic of the DHM setup including a microfluidic chip, tubings, the microscope light source, and objective. The insert figure on the top left highlights the hydrodynamic focusing principle using four sheath flows and one sample inlet. **(b)** Exemplary image of a blood cell measurement. Here, the horizontal and vertical alignment allows measurements without a cell loss due to defocusing or cells out of the Field of View (FOV). Image adapted from [207].

50 mm long channel. To ensure high-focusing precisions, viscoelastic and hydrodynamic techniques were combined. Viscoelastic focusing was enabled by introducing specific polymer solutions to the measurement media and the sheath flows. In the here presented work, Polyethylene oxide (PEO) or Polyvinylpyrrolidone (PVP) were dissolved in different concentrations in Phosphate-Buffered Saline (PBS) (Table 3.1). PVP (M_W = 360 kDa, Sigma-Aldrich) has been shown to promote three-dimensional particle focusing in cylindrical channels [129, 130]. In different experiments, a nearly constant shear viscosity for PVP was shown for shear rates $\dot{\gamma} < 10^3$ with a slight shear-thinning behaviour for larger values [131, 132]. PEO (M_W = 4 MDa, Sigma-Aldrich) is also commonly used for particle sorting and alignment [133, 134]. As for PVP, it shows a stable shear viscosity in the lower shear rate regime and shear-thinning properties for higher shear rates. It was also observed that its inherent focusing properties are reduced in the shear thinning regime [135].

Alternatively to the Fraunhofer channel, a second microfluidic design was used for erythrocyte cell alignment. For some experiments, not only the horizontal focusing but also the orientation of the discoid erythrocytes was of interest. This can be especially relevant when looking at intracellular properties of erythrocytes, which need a reproducible alignment of the non-rotationally symmetrical cells. In order to achieve this, a Polydimethylsiloxane (PDMS) chip with a width of 500 µm, a height of 50 µm, and a length of 90 mm was designed. As measurement media, again, either PVP or PEO solution served as a viscoelastic material. Contrary to the first design, only one inlet and one outlet were implemented. The focusing in the vertical direction was waived not to induce any turbulences on the cells.

For hydrodynamic focusing, a total of five inlets to the microfluidic channel were implemented. One served as sample inlet and four as sheath flows surrounding the sample

Table 3.1: List of used polymers used for viscoelastic focusing. All polymers were diluted in PBS.

Polymers	Concentration (w/v)	Atomic mass unit (M_W)
PVP	0.9 %	360 kDa
PEO	0.05 % 0.1 % 0.15 % 0.2 %	4 MDa

from the bottom, top, and sides. The total flow rate was fixed to 1.6 µL/s, resulting in a Reynolds number of $Re \approx 6$. This low Reynolds number highlights that the flow conditions are in the laminar flow regime.

3.2.3 Droplet Fluidics

For droplet creation, a flow-focusing geometry with mineral oil as the dispersed and deionised water + 0.1 % (v/v) Tween-20 as the continuous phase was used. Here, the refractive index of deionized water and mineral oil is 1.333 and 1.467, respectively. The PDMS channel for droplet generation has a homogeneous height of $h = 22\,\mu m$, a orifice width of $w_O = 12\,\mu m$, a disperse phase width of $w_D = 15\,\mu m$, a continuous phase width of $w_C = 14\,\mu m$, and a outlet width of $w_{\text{Out}} = 50\,\mu m$. The PDMS channel was connected to a glass surface with plasma bonding. The flow rate ratio between both phases ($Q_{\text{diff}} = Q_C/Q_D$) varied throughout different experiments.

3.2.4 Analysis of Cell Morphologies and Focus Values

Quantitative phase images of the DHM have a size of 512×384 pixels, the phase shift is stored in float, and each image can contain more than one cell. Before the **properties of single cells** can be analysed, specific preprocessing steps are needed. Background subtraction is applied to remove background noise and artefacts in the capture. This is performed by taking the median of the first images of the capture. Since the FOV does not change during a measurement, the background (including all background noise) remains unchanged. Dependent on the measurement, the median of the first $20 - 1,000$ images is taken. After the background subtraction, the important regions in the image need to be located, hence the blood cells. This is performed by an applied binary thresholding. Dependent on the sample and the size of the cells, a threshold value between $0.3 - 0.45$ rad provides good results in filtering out small debris [209]. The remaining objects are stored in smaller image sections (patches) for further processing.

Morphological features based on the shape and size of the object are calculated from the contour line, binary mask, and intensity of the cell images. Texture characterising features are calculated from the Grey-Level Co-occurrence Matrix (GLCM), which describes

the distribution of co-occurring pixel values in an image. This is commonly used for texture analysis in image processing [136]. Such cell analysis allows high intuitiveness and explainability for the user but can have limits in complex intracellular cell analysis. Most used examples of the morphological features can be found in table 3.2.

Table 3.2: List of regularly used morphological features calculated from float phase images.

Feature	Unit	Description
Equivalent Diameter	µm	Diameter of a fitted circle whose area is same as the contour area
Perimeter	µm	Cell contour perimeter
Width	µm	Width of the bounding box with the minimum area
Height	µm	Height of the bounding box with the minimum area
Cell Area	μm^2	Area within the cell contour
Optical Volume	μm^3	Sum of all contour volume pixel, whereas the volume pixel is defined by: $\lambda/2\pi(pixelsize)$
Aspect Ratio	a.u.	Quotient of width and height
Radius Variance	a.u.	Variance of the distance between the centroid of the contour and each contour point
Circularity	$[0, 1]$	Dependent on the cell area and the perimeter with: $4\pi(CellArea)/(Perimeter)^2$
Biconcavity	a.u.	Correlation of phase values on a horizontal and vertical cut in the centre of the cell contour compared to $-4x^4 + 4x^2 + 0.5$
Homogeneity	a.u.	Homogeneity of phase values for all pixels inside the cell contour based on the grey level co-occurrence matrix
Optical Height Maximum	rad	Maximum phase value inside the segmented object
Optical Height Mean	rad	Mean phase value inside the segmented object
Optical Height Variance	rad	Phase value variance inside the segmented object

The Sobel Gradient sharpness functions [137, 138] was used to investigate whether a cell is **in focus**. This method is edge-based thus, the assumption was made that a focused image has a sharper edge and therefore, higher frequency components than a blurred image. The Sobel Gradient operator convolves an image $\mathbf{Z} \in \mathbb{R}^{N \times M}, N, M \in \mathbb{N}$ with a small kernel $\mathbf{K} \in \mathbb{R}^{(2n+1)\times(2n+1)}, n \in \mathbb{N}$ in horizontal and vertical direction (x, y). The discrete convolution operation is defined as:

$$\mathbf{Z}(x, y) * \mathbf{K}(x, y) = \sum_{i=-n}^{n} \sum_{j=-n}^{n} \mathbf{Z}(x + i, y + j) \cdot \mathbf{K}(n + i, n + j) \tag{3.3}$$

The partial derivatives of $\mathbf{Z}$ in the horizontal and vertical direction are stated as:

$$\mathbf{G}_x = \frac{\delta \mathbf{Z}(x,y)}{\delta x} = \begin{bmatrix} -1 & 0 & 1 \\ -2 & 0 & 2 \\ -1 & 0 & 1 \end{bmatrix} * \mathbf{Z},\ Z \in \mathbb{R},\ N, M\ \in\ \mathbb{N} \tag{3.4}$$

$$\mathbf{G}_y = \frac{\delta \mathbf{Z}(x,y)}{\delta y} = \begin{bmatrix} -1 & -2 & -1 \\ 0 & 0 & 0 \\ 1 & 2 & 1 \end{bmatrix} * \mathbf{Z},\ Z \in \mathbb{R},\ N, M\ \in\ \mathbb{N} \tag{3.5}$$

At each point of the image, the gradient approximation and the corresponding sharpness function can be stated as:

$$\mathbf{G} = \sqrt{\mathbf{G}_x^2 + \mathbf{G}_y^2} \tag{3.6}$$

$$S_{\text{Sobel}}(\mathbf{Z}) = \sum_{i=1}^{N} \sum_{j=1}^{M} \mathbf{G}(i,j) \tag{3.7}$$

where $\mathbf{G}(i,j) \in \mathbb{R}$ is a component of the matrix $\mathbf{G} \in \mathbb{R}^{N \times M}$.

3.2.5 Extraction of Leukocytes out of Whole Blood

One method to extract leukocytes from whole blood is by **immunomagnetic separation** that uses magnetic nanoparticles functionalized with cell-specific antibodies. In the case of helper T-cells, B-cells, neutrophils, and eosinophils, all other leukocytes are removed by magnetic labeling. In contrast, erythrocytes and platelets are removed by aggregation and density gradient differences. No centrifugation steps or direct cell labeling were needed for the extraction step, allowing gentle cell handling. Only when necessary, remaining erythrocytes were removed by using the Miltenyi Biotec MACSxpress® erythrocyte depletion kit. After all unwanted cells are removed, the remaining cell suspension is centrifuged at 400 × g for 10 min. This will result in a pellet of cells from which the supernatant can be removed, and the test solution can be added. Monocytes were obtained with the help of the Pan Monocyte isolation kit of Miltenyi Biotec. The protocol consists of two parts: separating Peripheral Blood Mononuclear Cells (PBMCs) via density gradient centrifugation and dividing the monocytes from other PBMCs via magnetic labeling. Three centrifugation steps were performed for the first step, including one centrifugation with 400 × g for 35 min and two steps with 200 × g for 10 min. Magnetic separation works by the direct magnetic labeling of monocytes.

Another method to extract leukocytes out of blood samples is by **lysis** of the erythrocytes. This can be performed using water or specific lysis buffers. The hypotonic water lysis of erythrocytes used in this work was previously described [139]. Remaining erythrocyte fragments are removed using the Miltenyi Biotec MACSxpress® erythrocyte depletion kit. After centrifugation with $400 \times$ g for 10 min, the remaining pellet was resuspended in the measurement solution. For the second method, a conventional erythrocyte lysis buffer (J62990 RBC lysis buffer for humans, Alfa Aesar) based on ammonium chloride and potassium bicarbonate-based buffers was used. These buffers are broadly used to isolate deoxyribonucleic acid and ribonucleic acid, as well as for several flow cytometer assays [140, 141]. 1 mL of blood was mixed with 4 mL of lysis buffer at room temperature and then incubated for either 5, 10, 15, 20, or 25 minutes with continuous mixing on a roller mixer. After centrifugation with $1,000 \times$ g for 10 min, the remaining pellet was resuspended in 500 µL of the measurement solution.

3.2.6 Immunostaining of Cell Surface Markers

Identifying and analyzing different cells requires, in many cases, the staining of target proteins, which are expressed by the cells. These cell surface markers are labeled with specific primary antibodies. The antibodies can either be tagged with fluorescent molecules or with specific binding proteins for further processing. In this work, 1 µL of antibodies was used for 49 µL of cell suspension up to a concentration of 1×10^4 µL^{-1}. After the addition of antibodies to the cell suspension, the mixture is incubated in the dark for 10 minutes at $2 - 8$ °C. To remove unbound antibodies after incubation, the sample was washed twice. For this, the sample was centrifuged at $400 \times$ g for 10 min, allowing the removal of the supernatant and the resuspension with PBS. An overview of some of the most frequently used antibodies in this work can be found in table 3.3.

Table 3.3: List of used antibodies for cell staining. For a clear identification the Cluster of Differentiation (CD) naming scheme was used.

Antigen	Conjugate	Dilution	Target
CD3	APC	1:50	T-cells
CD4	FITC	1:50	Helper T-cells
CD4	Biotin	1:50	Helper T-cells
CD19	PE	1:50	B-cells
CD45	VioBlue	1:50	Leukocytes
CD54	FITC	1:50	Broader activation marker
CD61	APC	1:50	Platelet marker
CD62P	APC	1:50	P-selectin as platelet activation marker
CD64	PE	1:50	Activation marker for monocytes and neutrophils
CD71	FITC	1:50	T-cells activation marker

3.2.7 Labeling of Leukocytes with Microbeads

The strong non-covalent interaction of the streptavidin-biotin complex is used in assays to bind various biological molecules. Streptavidin is a tetrameric protein with four subunits, each able to bind one molecule of biotin with high affinity per subunit. The dissociation constant has been widely accepted as $K_d \sim 10^{-14}$ [142]. Three main reasons exist for the specific and irreversible binding between both proteins. The hydrogen bonds, van der Waals interactions between both molecules, and specific surface polypeptide loops of the streptavidin, which can integrate biotin. The advantage of this binding is that it is rapid and almost independent of temperature, pH value, proteolysis, and denaturants. In addition, since biotin is a small molecule, its interaction with the streptavidin protein does not significantly affect the functionality or shape of streptavidin. Because of these advantages, streptavidin-coated beads are commercially available for microfluidic assays that can be used to label and detect biotinylated cells [143, 144].

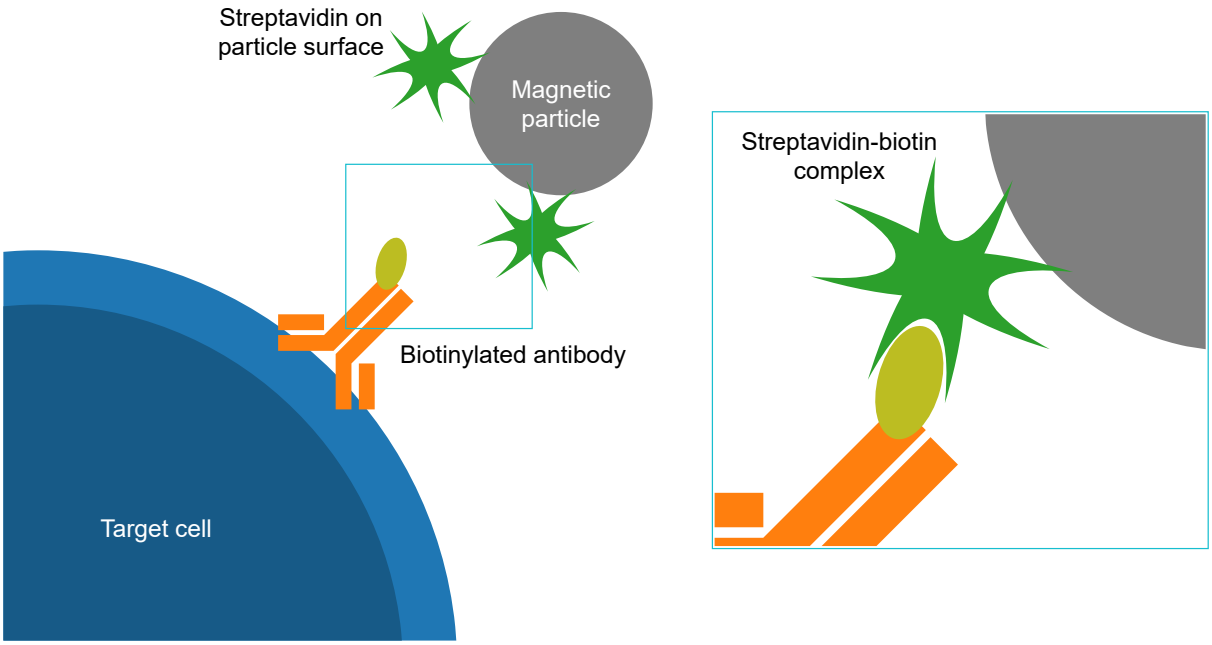

Figure 3.4: Schematic illustration of the binding of magnetic particles to a target cell. This is obtained by the specific and near covalent binding between streptavidin and biotin.

After isolating single leukocytes, they were stained with the respective CD-biotin antibody using the protocol in chapter 3.2.6. In the case of B-cells, these are CD19-biotin antibodies and in the case of $CD4^+$ T-cells, they are $CD4^+$-biotin antibodies. This staining step is followed by labeling the coated cells with streptavidin-coated beads and then incubating them for 15 minutes in the dark at $2 - 8\,°C$. Micromer®-M magnetic polystyrene beads from micromod with a diameter of 2, 4 and 8 µm were diluted in the cell suspension with a factor of 26, 16, and 11.5. Here, the cell suspension never exceeded $1 \times 10^4\,\mu L^{-1}$.

3.2.8 Sphering of Erythrocytes

Isovolumetric sphering was achieved by mixing 200 µL of whole blood with 120 µL of sphering buffer. The adopted sphering buffer consisted of 0.1 % glutaraldehyde, 109.30 mM sodium chloride, 4.03 mM Na_2EDTA, 3.36 mM Na_4EDTA, and 0.035 mM sodium dodecyl sulfate (SDS). This step was followed by a centrifugation of 400 × g for 10 min to remove the sphering buffer. The sphered erythrocyte pellet is then resuspended in 12 mL of 0.9 % PVP and divided into three control groups. All samples are stored at 4 °C over a duration of 33 days. For each measurement, a total of 3,000 frames were acquired.

3.2.9 Finite Element Modelling

The characterisation of the laws of physics, such as electrostatics, quantum mechanics, sound, and fluid dynamics, which are usually dependent on time and space, can be expressed as a Partial Differential Equation (PDE). In many cases, these PDEs cannot be solved by analytical methods and need a numerical estimation. The FEM is a numerical approach that divides the model geometry into smaller so-called finite elements and generates a finite number of points. The size of the finite elements, also referred to as mesh elements, greatly influences the precision of the final estimation. However, a finer mesh comes at a high computational cost, which means a trade-off between more accurate solutions and longer computation times, including big memory requirements. For each finite number of points, called nodes, the approximated solution is numerically solved by consideration of initial value, boundary, and transitional conditions.

COMSOL Multiphysics 5.3 is a software specialised in solving FEM simulations. Allowing the graphical design of the geometry, adding initial values and boundary conditions, using a pre-implemented set of PDEs for different physical questions, and creating a mesh. The microfluidic module of COMSOL Multiphysics has many PDEs for fluidic simulations in a laminar regime already implemented, allowing a simple simulation of channel properties as shown in chapter 3.3.

3.3 Microfluidic Cell Manipulation

The use of a microfluidic chip in combination with the optical system has many advantages, like a reproducible focusing of blood cells in one focal plane and the alignment of erythrocytes for intracellular analysis. However, there are also possible influences on the sample introduced by the microfluidic system. In this chapter, some advantages and potential disadvantages are discussed.

First, the **microfluidic channel was simulated** to obtain certain flow properties acting on the sample. For this purpose, the described channel geometry of the Fraunhofer channel was simplified as far as it did not change the simulation result. This allows more accurate analysis with limited computing power by increasing the mesh density. One example is

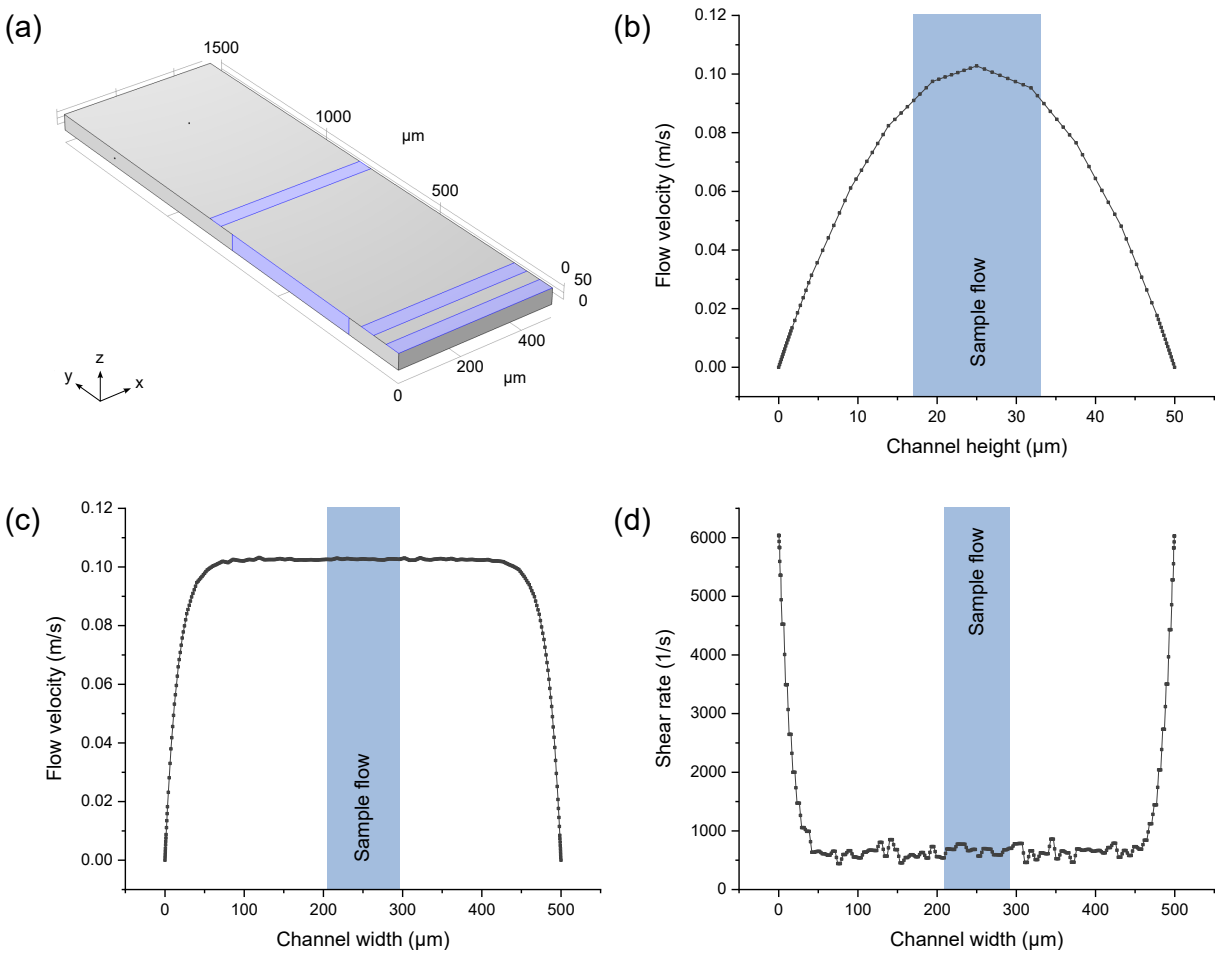

Figure 3.5: Simplified FEM simulation of the Fraunhofer microfluidic channel. Flow velocity and shear rate values are obtained by simulations performed with COMSOL Multiphysics 5.6. **(a)** Geometry of the model used. Blue areas highlight the different inlets. **(b)** Flow velocity in vertical direction at $y = 1{,}250\,\mu m$ showing a parabolic flow profile. The focused sample flow under typical flow conditions is highlighted in blue. **(c)** Flow velocity along the width of the channel at $y = 1{,}250\,\mu m$. **(d)** Shear rate distribution in horizontal direction at $y = 1{,}250\,\mu m$.

reducing the channel length to 1,500 µm. It could be seen that immediately after the last inlet, a balance between the different flows was established, which did not change further along the channel. Values of horizontal and vertical flow value distributions were calculated at $y = 1{,}250\,\mu m$. In both cases, the line was drawn in the centre of each plane. Flow rates of the different inlets and materials properties were set as previously discussed (chapter 3.2.2). The total flow rate of 1.6 µL/s resulted in a maximum flow velocity of 10.3 cm/s (Figure 3.5b). The maximum flow velocity was located in the centre of the channel and could be seen both in the vertical and horizontal dimension 3.5b and c). As expected for laminar flow conditions, the total flow profile showed a parabolic form with the minima at the channel borders [50]. This was particularly evident in Figure 3.5b.

Furthermore, the shear rate distribution within a microfluidic system is also a relevant factor. Higher shear rates can influence the sample and therefore should be avoided. Figure 3.5d shows the shear rate plotted against the channel width. As for the flow velocity over the horizontal plane, the same position was evaluated to obtain the shear values. The portion of the sample flow for normal flow conditions is highlighted in blue. Contrary to the flow rate, the shear rate had its maximum values at the channel borders, where the velocity difference was the biggest. For smaller flow velocity differences also, the shear rate is reduced. This was mainly in the centre of the channel, between $x = 50\,\mu m$ and $x = 450\,\mu m$. Here values were distributed around $600\,s^{-1}$.

Different **experiments were performed** to see whether the flow conditions and the measurement media influence the sample. First, the influence of the measurement media was analysed by storing a platelet solution in different media for 120 minutes. This included a regular PBS solution and PEO solution in different concentrations (0.05 %, 0.1 %, 0.15 %, and 0.2 %). To test whether this had an influence on the cell composition, the amount of aggregated platelets was measured. The first measurement without ageing is with a value of 0.78 %, the same for all media. However, within the first 15 minutes, big differences arose. While the values for PBS, 0.05 % PEO, and 0.1 % PEO stayed nearly the same (0.68 %, 0.72 %, and 0.76 %), already some differences could be seen for 0.15 % PEO (1.82 %) and 0.2 % PEO (8.15 %). This trend continued within the 120 minutes, whereby the number of aggregates continued to rise for 0.15 % PEO at minute 120 to 2.39 %. The PBS, 0.05 % PEO and 0.1 % PEO solution tended to distribute around the initial measurement value indicating no influence of the medium on the blood cells (Figure 3.6a and b).

Activation markers were measured with a common fluorescent flow cytometer to further validate these findings and to see whether the microfluidic system had an **influence on the cells**. In Figure 3.6, the results for the T-cell activation marker CD71 and the platelet activation marker CD62P are shown. Further activation markers were measured and can be found elsewhere [214]. For the CD71 experiment, leukocytes were extracted from whole blood and measured before and after introduction to the microfluidic system. Before the flow cytometry measurement, cells were labeled both with CD71 and CD45 to be able to exclude debris or remaining erythrocytes. After passing the microfluidic channel, cells were collected and directly labeled with the same antibodies. Gates for activated and non-activated cells were set at the same threshold. This allowed a comparison between both cohorts, even though there are differences in the number of measured cells due to the dilution in the Fraunhofer channel. The amount of activated cells rose from 1.77 % before the fluidic to 2.35 %. For CD62P measurements, a platelet solution was measured in PBS and 0.05 % PEO before passing the fluidic and in 0.05 % PEO after passing the fluidic. Since the values of CD62P change gradually with activation, the MFI over all platelets was calculated. As shown before, the introduction of 0.05 % PEO did not induce noteworthy differences on platelets compared to PBS. This was reflected by a MFI of 49.93 and 48.45 for PBS and 0.05 % PEO. Additionally, after passing the fluidic, no increase of the MFI could be observed as it would be expected for activated platelets. Instead, the value dropped to 44.40.

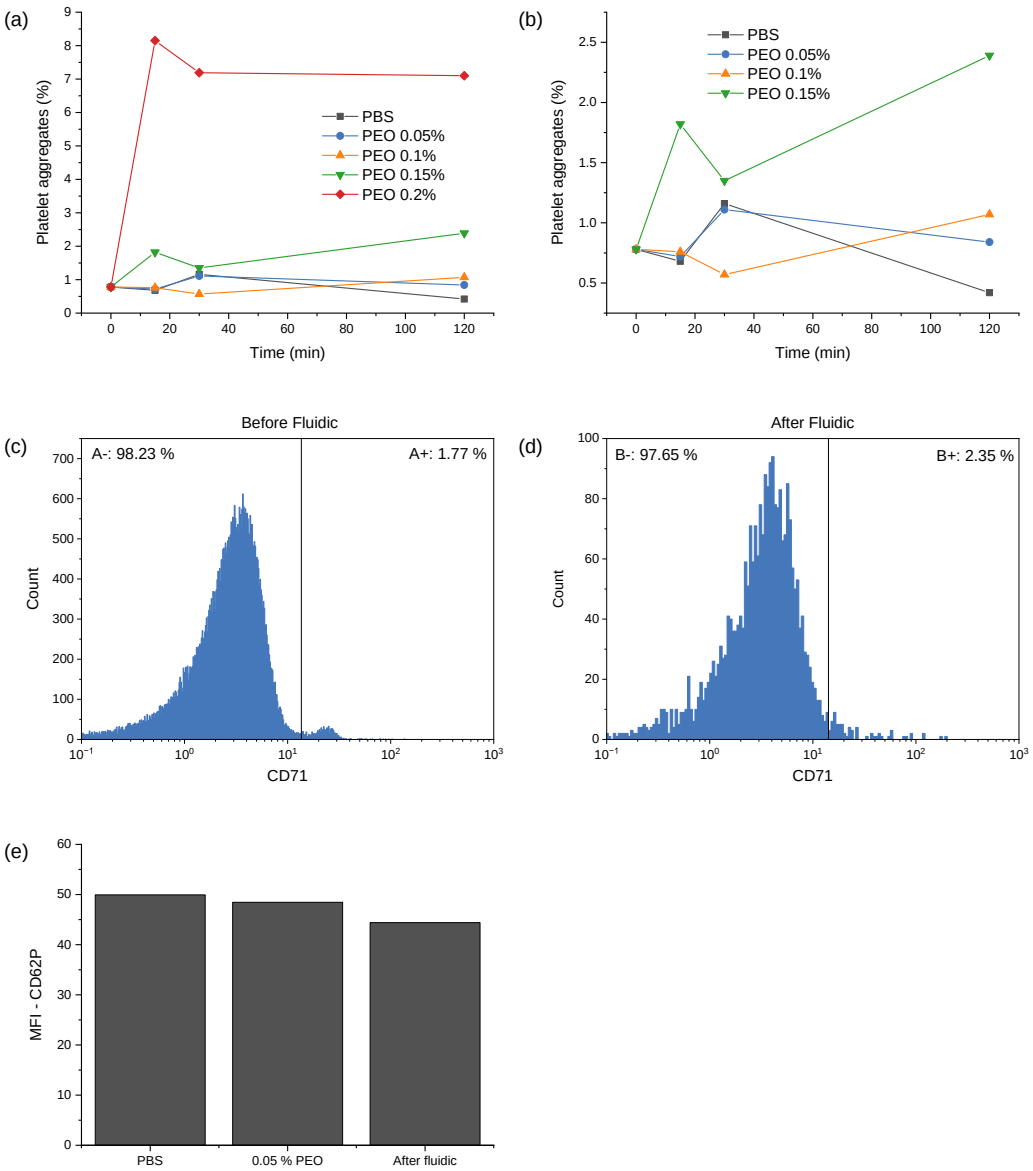

Figure 3.6: Influences of the microfluidic environment on the blood cells. **(a)** Effect of different PEO concentrations on the artificial formation of P-Aggregates over a storage time of 120 minutes. **(b)** Enlarged image of the lower PEO concentrations measurements. **(c)** Analysis of the T-cell activation marker CD71 in a healthy sample before being introduced to the microfluidic system. **(d)** Histogram of CD71 after the sample passed the microfluidic and was collected. **(e)** Analysis of the platelet activation marker CD62P (P-selectin) for samples stored in PBS, the measurement solution containing of 0.05 % PEO and after the sample passes the fluidics while stored in the measurement solution. The Mean-Fluorescence-Intensity (MFI) of CD62P over all platelets is plotted against the corresponding sample. Images partly adapted from [207, 214].

Finally, also the **concentration of blood cells** in the sample solution can have an influence on the measurement results. Especially when analysing aggregates, it is important to ensure that coincidences of cells due to high concentrations are not mistaken for aggregates. On the other side, the sample should not be overly diluted, otherwise, this leads either to a low statistical power or higher measurement times. Leukocytes are rare compared to all other blood cells leading to a low probability of randomly overlapping. Since erythrocyte aggregates are not analysed in this work, the main sources of errors can occur from overlapping platelets. Therefore, these types of cells were investigated in more detail with the Fraunhofer channel. A whole blood sample was diluted 1:25, 1:50, 1:75, and 1:100 and the individual platelets measured were analysed. For each dilution step, three measurements of the same sample were performed. Figure 3.7a shows the mean values and standard deviation of these three measurements. The number of single platelets compared to all platelets is plotted against the dilution factor. For higher dilutions, namely 1:75 and 1:100, nearly no differences in the amount of single platelets could be seen. The changes for lower dilutions. While at a dilution of 1:100 and 1:75 the single platelets were at 82.63 % and 82.67 %, this decreases to 79.84 % for 1:50 and to 68.42 % for 1:25.

One exception where the hydrodynamic focusing properties of the Fraunhofer channel are disadvantageous is the **uniformed orientation of erythrocytes** in the focal plane. Here, influencing forces from the side sheaths interact with the horizontal focusing of the viscoelastic media, resulting in the random orientation of the cells. To surpass this phenomenon, another channel setup with only one inlet was used. In this case, mainly the lateral viscoelastic force acting on the cells. Due to the geometry of the channel with $h << w$, the forces in the vertical direction are dominant in the centre of the channel. This allows a uniform orientation of the non-rotationally symmetrical erythrocytes. As different polymers interact differently with the sample, this experiment was performed on two polymer solutions, 0.9 % PVP and 0.05 % PEO. The orientation of the cells was obtained by analysing the morphological parameters biconcavity and circularity (Table 3.2). Erythrocytes with a circularity > 0.8 and a biconcavity > 1 were considered correctly oriented. Three measurements were performed for each polymer solution, whereby the mean and the standard deviation are plotted in Figure 3.7b. 49.85 % of all erythrocytes were correctly aligned when diluted in 0.9 % PVP solution. This value increased to 69.24 % when using 0.05 % PEO instead.

As mentioned before, a key advantage of using this microfluidic channel setup is the reproducible focusing of cells on one focal plane. To **characterise this focusing behaviour** in a diluted whole blood sample, the mean focus measure for every cell was analysed. This was performed by calculating the Sobel sharpness values for each pixel within a cell segmentation. The mean overall pixel then results in the mean focus measure. A typical distribution can be seen in Figure 3.7c. The threshold defining the out-of-focus and in-focus cells was set to 5 by manually looking at cells in different focus planes and their corresponding mean focus measures. Lastly, this methodology was used to evaluate focused cells in a study including 146 patient measurements. Again, the threshold for the mean focus measure was set to 5. The mean value of cells in focus overall measurements is at 92.09 %, with a corresponding median of 90.71 %. Within the 146 measurement, the

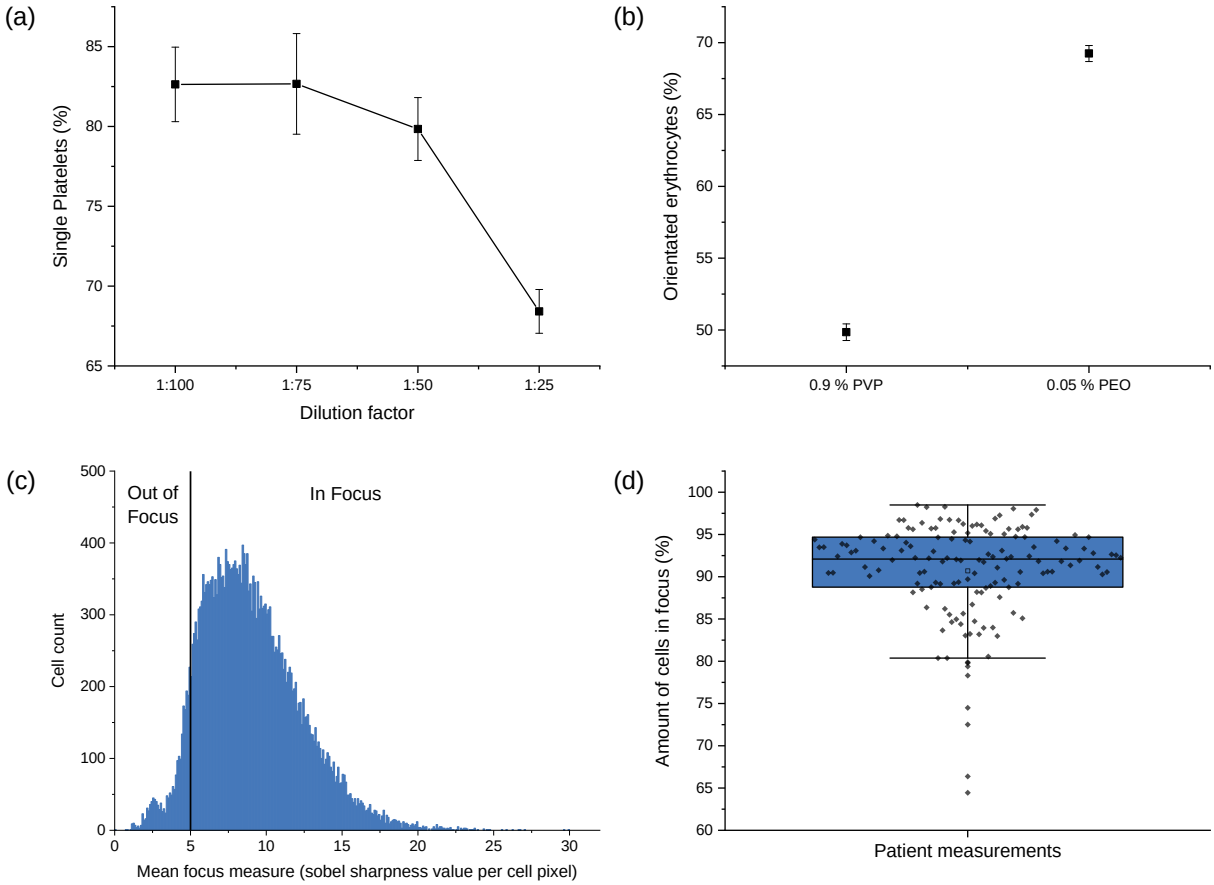

Figure 3.7: Channel properties and performance at normal flow conditions. **(a)** Detection of single platelets in the same sample for different dilution factors highlighting the threshold of platelet overlapping. **(b)** The proportion of uniformly orientated erythrocytes is shown for the PEO and PVP measurement media. Here, the erythrocyte cell alignment channel was used. **(c)** Through the calculation of Sobel sharpness values, a threshold can be set at which cells are classified as out of focus and in focus. **(d)** The number of cells in focus is shown for a cohort of 118 independent clinical measurements. In this case, the Fraunhofer channel was in use. Images partly adapted from [207].

lowest value was at 64.44 % while the highest reached 98.49 %.

3.4 Cell Concentration Measurements

The measurement of blood cell concentrations is a highly relevant marker in the field of haematology. Therefore, many state-of-the-art analysers provide this information [145]. Cell concentration can be estimated either by analysing the number of cells per capture and comparing this to a known reference concentration measurement or by adding the

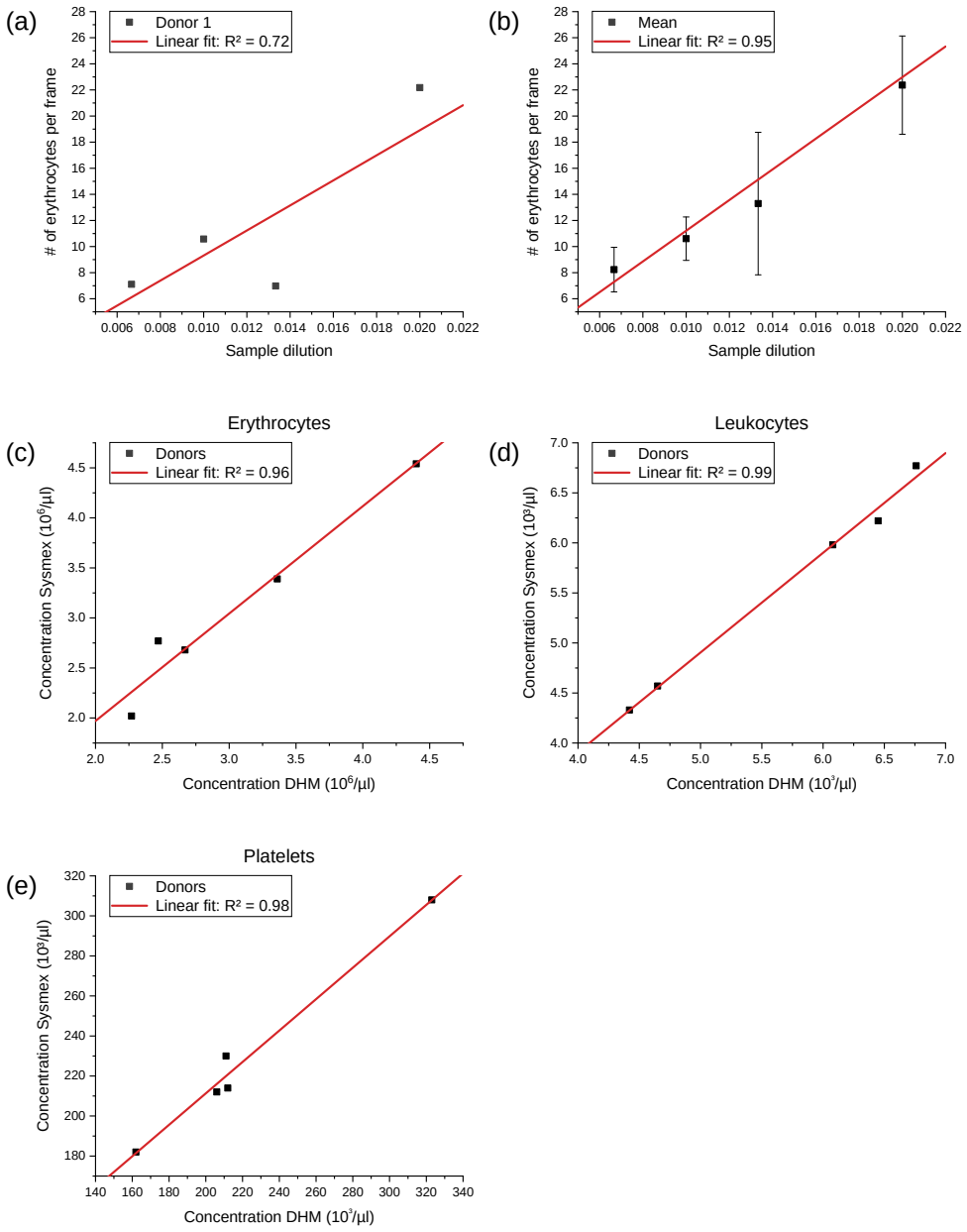

Figure 3.8: Concentration measurements of different blood cells. **(a)** Measurement of erythrocytes per frame for one exemplary donor at four different dilution steps. The linear fit between the different measurement points is highlighted in red. **(b)** Number of erythrocytes per frame for four independent dilution experiments. The mean values and the standard deviation are shown in black. **(c)** Comparison of erythrocyte measurements between Sysmex and phase imaging flow cytometer measurements with five independent donor samples. **(d)** Correlation between leukocyte concentrations measured with the Sysmex analyser and the phase imaging flow cytometer. **(e)** Comparison of erythrocyte measurements between Sysmex and phase imaging flow cytometer measurements.

reference directly into the sample [146]. In this section, both methods were tested.

For the first method, a reproducible measurement of **cell numbers per frame** is highly important. Four blood samples of independent healthy donors were analysed to test the performance of the here presented method. Blood was diluted with the factor 1:50, 1:75, 1:100, and 1:150 in the 0.9 % PVP solution and then measured in the Fraunhofer microfluidic channel. In Figure 3.8, the results for (a) one exemplary donor and (b) for all donors are plotted. A high correlation between the introduced dilution and the erythrocytes per capture could be seen among all donors. Increased dilution corresponded to a lower number of cells per capture and the coefficient of determination of the linear fit was at 0.95. However, especially for lower dilutions (1:50 and 1:100), a high standard deviation could be seen, indicating outliers. One of these outliers was observable for Donor 1 at a dilution of 1:75. The measured 6.98 erythrocytes per capture at this dilutions were lower than the 10.58 and 7.11 for 1:100 and 1:150. This dramatically influences also the coefficient of determination, which was at 0.72.

In a second experiment, an **internal reference** was introduced to the blood sample. For this, monodisperse polystyrene beads (micromer®-M, micromod Partikeltechnologie GmbH) with a diameter of 8 µm were diluted in 0.9 % PVP and their concentration was measured with a hemocytometer. Through the dilution of the beads, the bead concentration in the final samples could be fixed to $7.45 \cdot 10^3\,\mu L^{-1}$. Reference beads with the same concentration were used for measurements of erythrocytes, leukocytes, and platelets. In all cases, the blood of five donors was analysed. For the erythrocyte and leukocyte experiment, the beads were introduced to the whole blood sample allowing a direct calculation of cell concentrations. For platelet measurements, the Platelet-Rich Plasma (PRP) had to be extracted first and then the reference beads were added. The final platelet concentration could be obtained by considering the total blood volume before extracting the PRP. Further sample preparation included a simple dilution of whole blood for erythrocytes, using a lysis buffer for leukocytes, and the dilution of the PRP for platelets. As shown in Figure 3.8c-e, there was a high correlation between reference measurements with a state-of-the-art analyser (Sysmex) and the here presented method (DHM) for all blood cells. The coefficient of determination for erythrocytes, leukocytes, and platelets between both methods was 0.96, 0.99, and 0.98, respectively. However, it is noteworthy that even though a positive overall correlation was given, slight differences in the absolute values sometimes occurred.

3.5 Influence of Sample Preparation on Cell Morphology

As previously discussed, one way of leukocyte extraction is through cell lysis of erythrocytes (chapter 3.2.5). This can be performed using either a hypotonic water lysis or a conventional erythrocyte lysis buffer. Both methods are performed on whole blood, so an influence on leukocytes cannot be ruled out. Two morphological parameters, namely Optical Height Maximum (OHM) and Equivalent Diameter (ED), were investigated to determine these effects. Variations in these values represent changes in the cells' outer

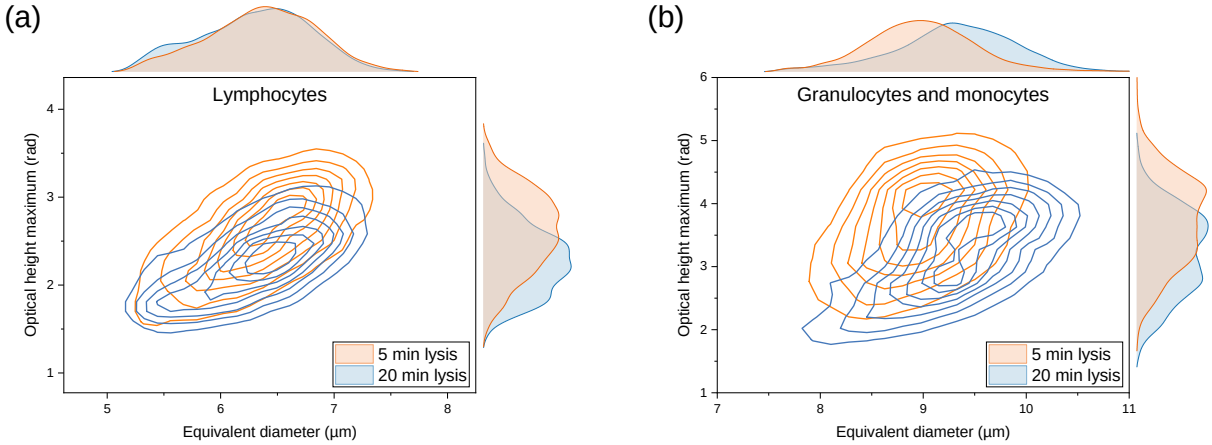

Figure 3.9: Changes of leukocyte morphologies through cell lysis. **(a)** Effect on lymphocyte equivalent diameter and optical height maximum when using 5 and 20 minutes incubation of erythrocyte lysis buffer. **(b)** Changes in monocyte and granulocyte morphology for the same experimental conditions. Images adapted from [214].

and/or inner shape. In the following, two populations were investigated: the lymphocyte and granulocyte-monocyte clusters. They were separated from each other and debris by applying suitable gates along the ED. Erythrocyte debris and platelets have a diameter below 5.30 µm, lymphocytes are between 5.30 µm and 7.50 µm, and the granulocyte-monocyte clusters are between 7.5 µm and 11.00 µm. Bigger objects with ED > 11.00 µm were classified as doublets and ignored for further analysis. As shown in Figure 3.9, single leukocyte populations were widely distributed along both axes, indicating a high heterogeneity. Here, the ED and OHM were plotted for an experiment using 5 min and 20 min of erythrocyte lysis buffer incubation times. It could already be observed from these two example measurements that longer incubation times seem to have an influence on the cells. For lymphocytes, mainly a decrease in OHM was seen while the diameter was not directly affected. In contrast, for granulocytes and monocytes both, a reduction in OHM and an increase of ED could be observed.

Different **leukocyte extraction methods** were analysed in four measurement samples of two donors to further evaluate this behaviour. Here, using hypotonic water lysis in combination with a depletion kit was compared to erythrocyte lysis buffer protocols using different incubation times. In Figure 3.10a and b, are shown mean values of ED in orange, the mean values of OHM in blue, and the corresponding standard deviation, which corresponds to the population distribution, in coloured areas. For lymphocytes, no relevant change in ED could be seen independent of the sample preparation method. Values remained over the whole experiments between 6.31 µm and 6.35 µm. A different pattern could be observed when looking at the OHM. While short incubation times of the lysis buffer also did not seem to show differences compared to the hypotonic water lysis (2.61 rad to 2.60 rad), longer incubation of 20 minutes resulted in a reduction of the OHM (2.28 rad). Influences on granulocytes and monocytes on the other hand, were even more dominant. Already after five minutes of incubation, a noticeable difference in OHM

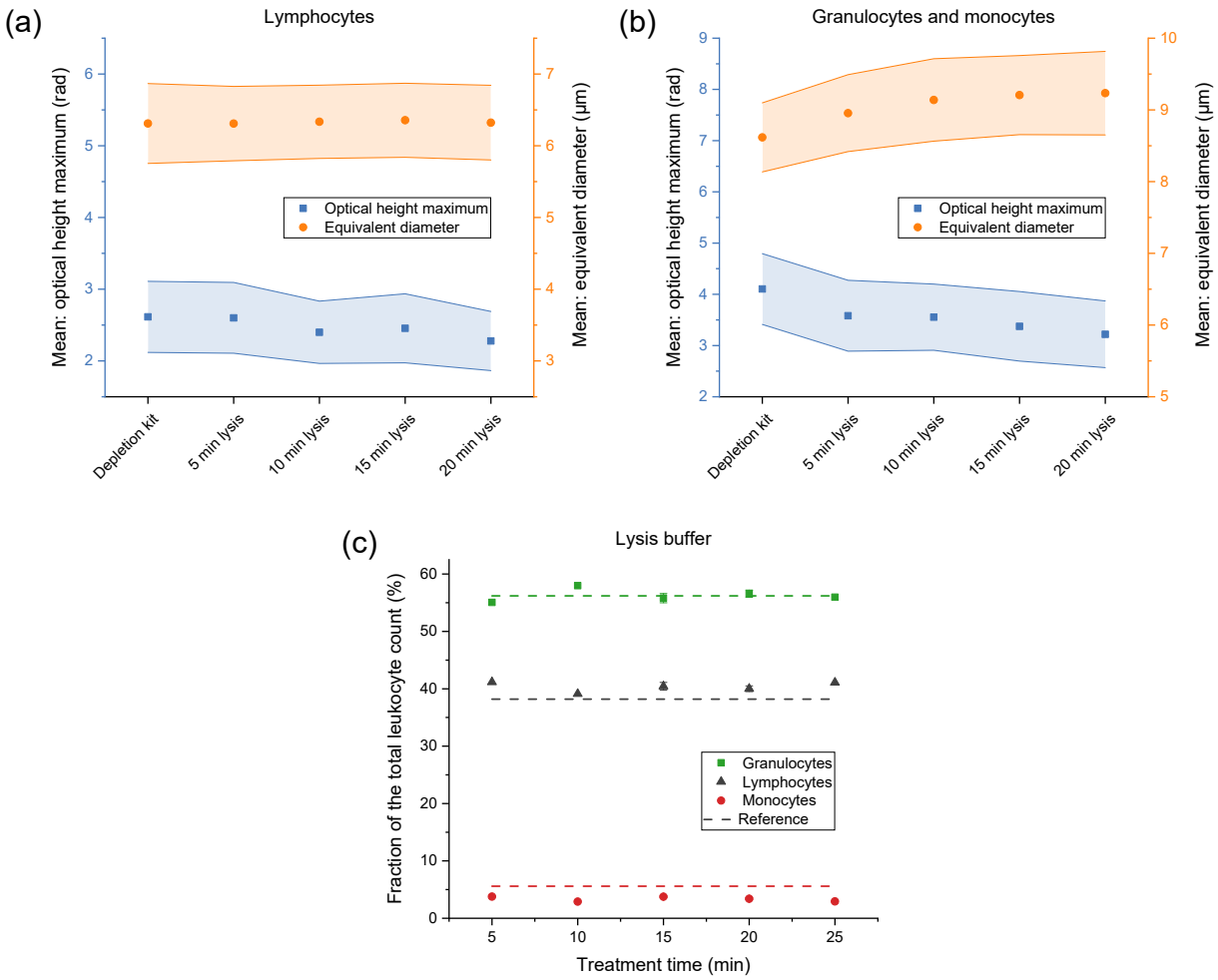

Figure 3.10: Influence of erythrocyte cell lysis on leukocyte morphologies and numbers. Presented data for two donors with a total of four measurements. **(a)** Changes in lymphocyte equivalent diameter (orange) and optical height maximum (blue) induced by different sample preparation methods. The mean of the four measurements is highlighted as squares or circles, whereas the coloured area indicates the standard deviation, which represents the population's distribution. **(b)** Equivalent diameter (orange) and optical height maximum (blue) for the granulocyte-monocyte population for different sample preparation methods. **(c)** Granulocyte, lymphocyte, and monocyte counts for different lysis incubation times, measured with a fluorescent flow cytometer. Images adapted from [214].

could be observed compared to hypotonic water lysis. Values dropped from 4.10 rad to 3.58 rad. The trend continued for longer incubation times, resulting in 3.21 rad at 20 minutes of incubation. In contrast to lymphocytes, there was even a noticeable change in the ED. For hypotonic water lysis, the mean ED over this population laid at 8.62 µm. This value increased to 9.00 µm for five minutes of lysis and 9.23 µm for 20 minutes. Thus, an inverse progression to the optical height could be identified. No relevant change in the standard deviation could be observed for all cell types and for both morphological

parameters indicating a homogeneous change over the respective populations.

Finally, the impact of erythrocyte lysis buffer incubation times was investigated by multicolour fluorescence flow cytometry. The aim was to observe if lysis not only affects the leukocyte morphology but also whether it changes leukocyte ratios. For this, three blood samples of one donor were independently labeled, and each was measured one time. As reference method served the complete blood count values obtained by a Sysmex XN-350 haematology analyser. The percentages are given as a fraction of the total number of white blood cells. Flow cytometer results showed granulocyte values between 55.06 % and 57.98 %, lymphocyte values between 39.12 % and 41.16 %, and monocytes between 2.94 % and 3.78 %. All subtypes showed no cell loss through long incubation times. Granulocytes and lymphocytes values agreed with the reference (56.20 % and 38.20 %), with monocytes showing higher values of 5.60 %.

3.6 Development of a Calibrator System

For the approval and operation of in-vitro diagnostic devices, calibration is required. According to the International Vocabulary of Metrology (VIM), it is an "operation that establishes the relation, obtained by reference to one or more measurement standards, that exists under specified conditions, between the indication of a measuring system and the measurement result that would be obtained using the measuring system" [147]. This implies regularly using a reference, also known as a quality control material or calibrator, to test the measurement system. Here, the introduction of a calibrator serves two purposes. First, it allows the comparison between different devices using different technologies. This is especially important in the field of haematology analysers, where different fluidic setups, other hardware, or software are used [148]. In addition, many biomarkers such as white blood cell count, red blood cell count, and mean corpuscular volume, are measured at the same time. Second, it also allows longitudinal control of the system itself. This enables the location of errors occurring due to wear and tear or other influences. Although haematology analysers showed a rapid technological progress over the last years, it was not paralleled by a similar improvement of reference materials. Still, the usage of whole blood samples of healthy donors, collected with a suitable anticoagulant, is common practice [148, 149].

This chapter discusses possible calibrator systems for the DHM setup. The focus laid on the longitudinal quality control and less on the inter-technology comparability with other haematology analysers. For cell differentiation in quantitative phase imaging, mainly two properties are important: the phase difference and the object size. The first solely depends on the object's height and the refractive index. A suitable calibrator should therefore show a comparability in those properties when compared to the target sample. It should also have inherent reproducibility and stability over long storage times.

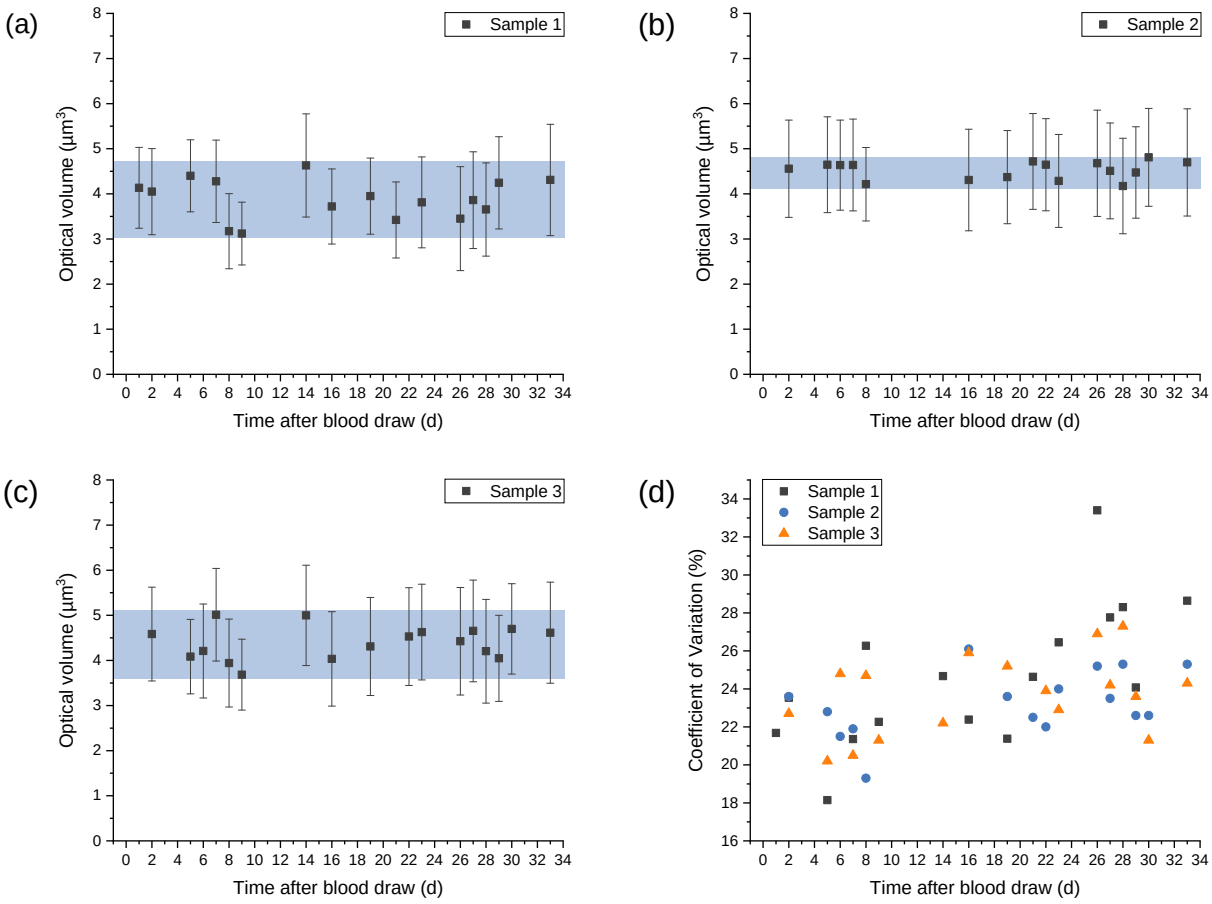

Figure 3.11: Ageing effects on the optical volume of sphered erythrocytes. (a-c) Mean and standard deviation of sphered erythrocytes optical volume over a duration of up to 17 days. The maximum range of the mean values is highlighted in blue.

3.6.1 Sphered Erythrocytes

Isovolumetric sphering of erythrocytes is an established method to measure the volume and refractive index in flow cytometry [150] and in DHM [151]. Here, the comparability over different samples and stability over a duration of 33 days were tested. For this, three different samples were prepared from a blood sample of one donor. The applied protocol for sample storing and capturing is highlighted in chapter 3.2.8. The results of the longitudinal measurement of this calibrator are shown in Figure 3.11. For inset figures a-c, the optical volume was plotted against the time after blood collection. The range of the mean volume was for Sample 1, 2, and 3 at $3.02-4.80\,\mu m^3$, $4.12-4.80\,\mu m^3$, and $3.62-5.13\,\mu m^3$, respectively. They showed a similar range of values but a varying distribution of the mean values. The standard deviation, which also represents the homogeneity of the cell population, ranged between $0.695-1.234$. To further evaluate the stability of the calibrator, also the Coefficient of Variation (CV) was calculated. For all three samples, a similar CV distribution between 18.14 % and 28.64 % could be observed with one outlier at sample 1 on day 26. Over the course, a slight increase in CV was observable.

3.6.2 Chicken Erythrocytes

One possibility of introducing a calibrator with multiple phase shifts per object while retaining the biological properties is using cells with a cell nucleus. In contrast to human erythrocytes, chicken erythrocytes contain a nucleus. This allows for a differentiation of the phase shift induced by the medium (n_1), the cell cytoplasm (n_2), and the cell nucleus (n_3). In Figure 3.12b, a typical optical height profile of such an erythrocyte is shown. While the background medium was set to zero, the cell cytoplasms showed a distinct plateau at around 2.30 rad. The cell nucleus induced an even higher phase shift resulting in an optical height of around 3.25 rad. A patent application has been filed describing the results of the investigations [219].

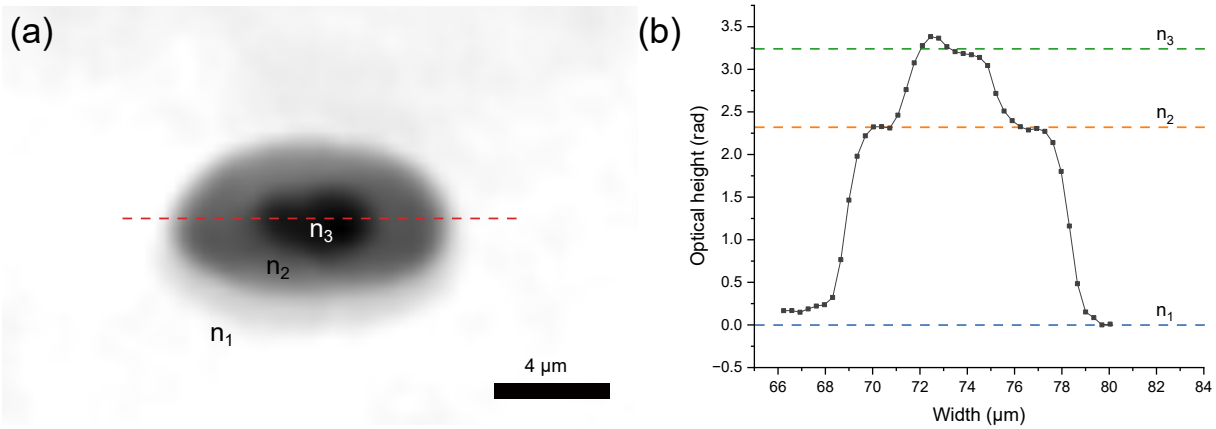

Figure 3.12: Chicken erythrocytes as a calibrator for DHM. (a) Quantitative phase contrast image of a chicken erythrocyte including the background (n_1), the erythrocyte cytoplasm (n_2), and the erythrocyte nucleus (n_3). The line indicates the height profile for inset figure (b). **(b)** Optical height profile of the erythrocyte, including the three distinct refractive index regions.

3.6.3 Droplets

Finally, droplets were investigated as an alternative non-biological calibration material. A difference between homogeneous single droplets (Figure 3.13a) and droplets in droplets (Figure 3.13b) can be made. Both structures were generated in flow-focusing geometries, whereby droplets in droplets are generated by putting two structures in a sequence. Here, the outlet of the first structure serves as an inlet of the second, while the continuous phase medium is the opposite for both geometries [152]. Single droplets induce one phase shift between the background medium (n_1) and the droplet (n_2). Droplets in droplets allow a second phase shift between the outer (n_2) and inner droplet (n_3). In the results presented here, only single droplets were investigated.

As before, the performance of the calibrator was evaluated by its homogeneity, stability, and similarity to the actual sample. Therefore, droplets were generated at day 0 and

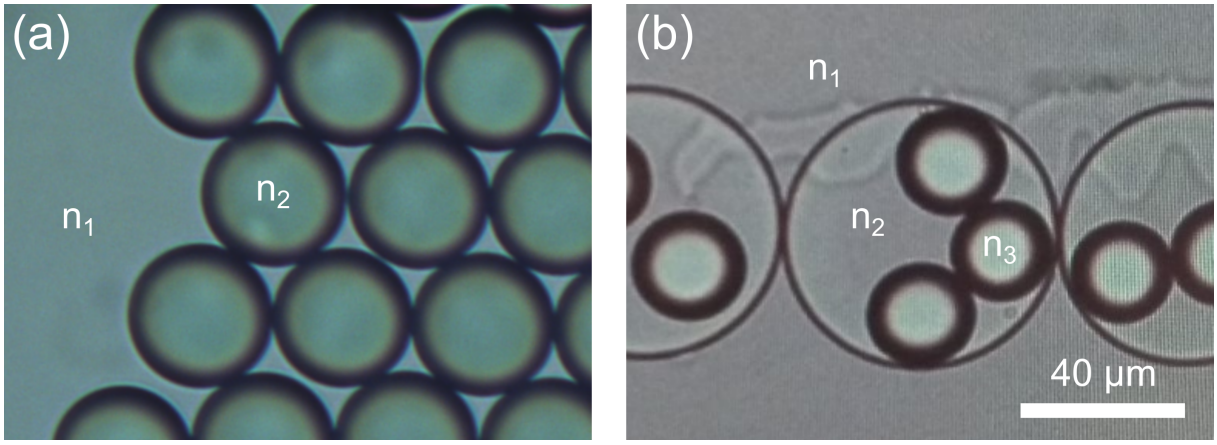

Figure 3.13: Different types of droplets generated in a flow-focusing geometry. (a) Droplets as calibrators allow a defined refractive index difference between the background (n_1) and the droplet (n_2). **(b)** Droplet in droplets can mimic intracellular refractive changes ($n_3 - n_2$).

then stored for 31 days at room temperature. Once a week, a total of 171 droplets were measured and analysed. Results for the droplet diameter are plotted in Figure 3.14a and b. The mean diameter and standard deviation values ranged from 33.31 ± 0.64 µm at day 0 up to 33.72 ± 0.80 µm on day 31. The median was the lowest at day 0 with 33.33 µm and the highest at day 21 with 33.79 µm. This change in values over time was also reflected when looking at the CV for each measurement. Within the first week, the values remained nearly the same with a CV at days 0 and 7 with 1.96 % and 1.97 %. After 16 days, the CV rose to 2.14 % and peaked at days 21 and 31 with a value of 2.42 % and 2.38 %.

Additionally, the OHM of the droplets were analysed for three different flow rate ratios between the continuous and dispersed phases. For each flow rate, three measurements with 5,000 images were performed. As expected, an increase in the flow rate ratio led to a decrease in droplet diameter and, therefore, a decrease in the OHM. For $Q_C/Q_D = 10$, $Q_C/Q_D = 20$, and $Q_C/Q_D = 32$ the mean OHM were 23.04 rad, 19.15 rad, and 15.98 rad, respectively. With the increasing flow rate ratio, the standard deviation between the three measurements also increased. At $Q_C/Q_D = 10$ the standard deviation was the lowest with 0.24 rad compared to the maximum at $Q_C/Q_D = 30$ with 0.65 rad.

3.7 Improved Leukocyte Subtyping through Targeted Cell Labeling

The label-free measurement of blood cells has many advantages but also some limits. This is especially the case for cells with a similar morphological appearance. Therefore, this experiment targeted cell labeling with polystyrene beads of different sizes to enhance the differentiation power. For this, the described protocols in chapter 3.2.7 were applied on previously extracted $CD4^+$ T-helper cells. Measurements were performed in the standard

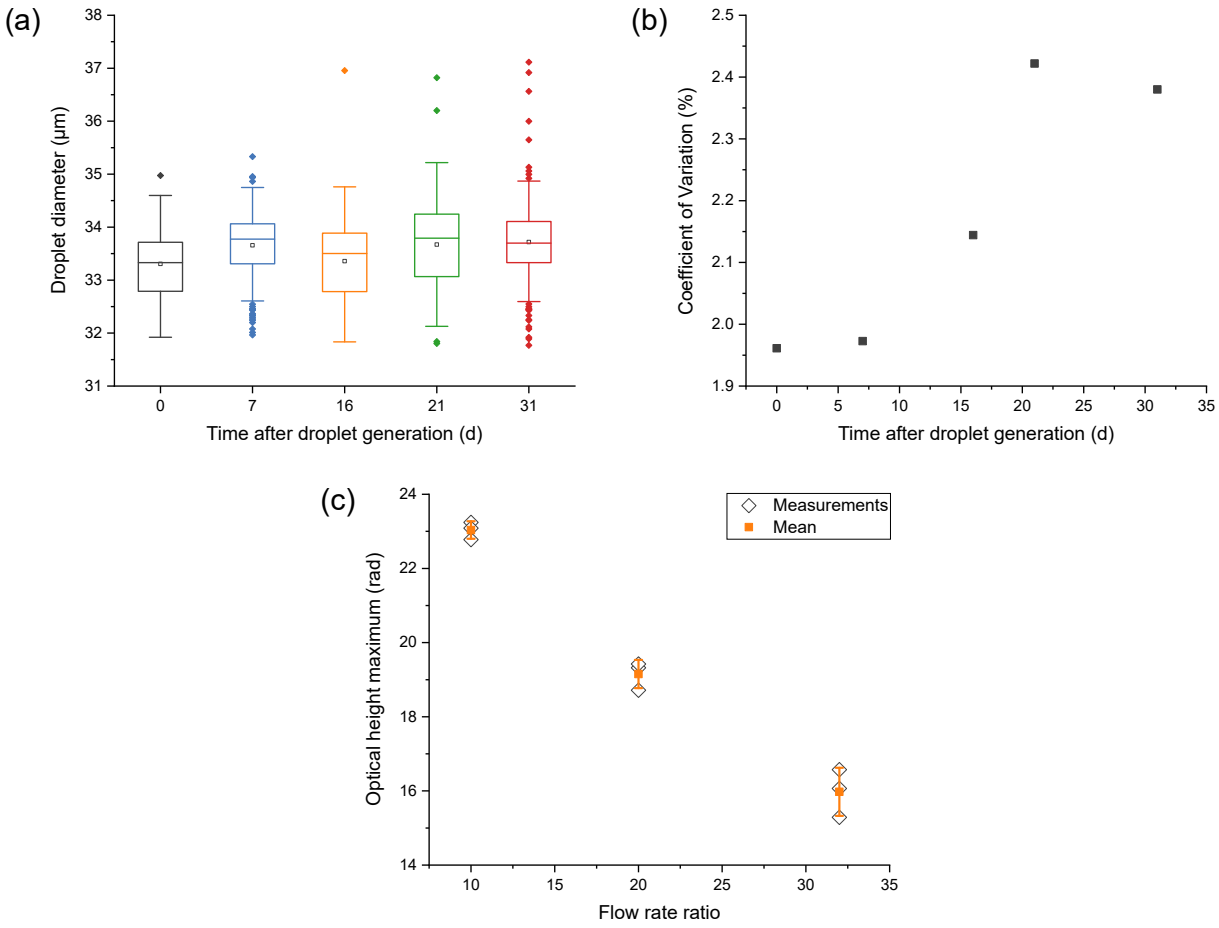

Figure 3.14: Properties of droplets as a calibrator for quantitative phase imaging. **(a)** Droplet diameters ($n = 171$) plotted against the storage time within a duration of 31 days. Each data point represents one outlier droplet, whereby the centerline represents the median and the framed black square represents the mean distribution. **(b)** Coefficient of variation of the droplet diameter within the 31 days of storage. **(c)** Optical height maximum of droplets plotted against the flow rate ratio Q_C/Q_D.

measurement setup. Images are analysed using the DHM Analyser from Siemens to extract the morphological features and Kaluza Analysis Software from Beckman Coulter for gating strategies and further analysis. Prior to the labeling experiments, the induced phase shift of the beads was measured and plotted in table 3.4. This included magnetic polystyrene beads with 2 µm, 4 µm and 8 µm which induced a mean phase shift in OHM of 1.07 rad, 3.69 rad, and 8.09 rad. For comparison, a population of $CD4^+$ and B cells were measured and showed a mean OHM of 2.97 rad and 2.98 rad, exceeding the value of 2 µm beads.

For the labeling with **2 µm beads**, $CD4^+$ cells were extracted using a MACSxpress® Whole Blood CD4 T Cell Isolation Kit (Miltenyi Biotec) as described in chapter 3.2.5. The $CD4^+$ cells were stained with CD4-Biotin antibodies and subsequently labeled with 2 µm streptavidin beads. Not all $CD4^+$ cells were labeled with beads, resulting in a

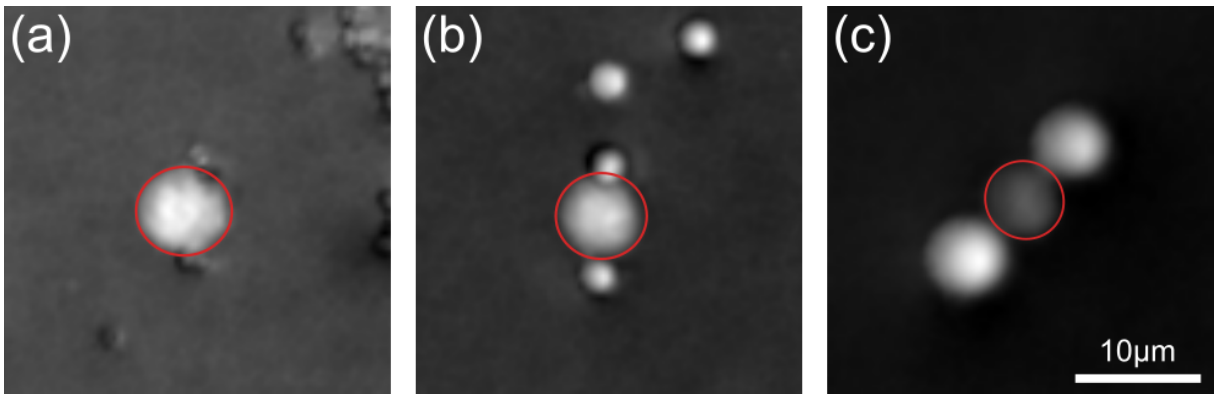

Figure 3.15: Quantitative phase contrast images of CD4$^+$ T-helper cells labeled with polystyrene beads of different sizes. **(a)** The CD4$^+$ cell, highlighted in red, is labled with multiple 2 µm beads. **(b)** Two 4 µm beads are connected to the CD4$^+$ cell in the centre of the image. **(c)** One example of a CD4$^+$ cell labeled with two 8 µm beads. For better distinguishability, the cell is again highlighted in red.

Table 3.4: Properties of different labeling beads, CD4$^+$ and B cells.

	Diameter	Material	Optical height maximum
2 µm Beads	2 µm	Polystyrene	1.07 rad
4 µm Beads	4 µm	Polystyrene	3.69 rad
8 µm Beads	8 µm	Polystyrene	8.09 rad
CD4$^+$ cells	7 µm	Biological	2.97 rad
B cells	7 µm	Biological	2.98 rad

labeled and non-labeled population that could be compared. Once the morphological features had been extracted, the different populations were analysed for their inherent characteristics. Smaller unbound beads could be separated from CD4$^+$ cells using a size filter with ED $5 - 16$ µm. Here, unbound cells had a high circularity of > 0.75, whereas aggregates showed values between $0.25 - 0.75$. The aggregate population included the desired cell-bead aggregates and undesired bead-bead aggregates. Those two populations could then be separated using a filter for ED and homogeneity. Bead-bead aggregates showed a higher homogeneity with a threshold of 0.4 while being slightly smaller. To see whether the use of 2 µm beads for labeling is feasible, the morphological properties of labeled and non-labeled CD4$^+$ cells were compared. Here, the ED was plotted against the OHM to see possible changes in size and phase shift. A total of two measurements were performed, containing 2,500 cells for each population. As shown in Figure 3.16a and d, no significant difference between both populations could be observed. The median OHM of non-labled cells is at 2.90 rad compared to the 2.91 rad for CD4$^+$ cells labeled with 2 µm beads.

For the labeling with **4 µm magnetic polystyrene beads**, the protocol was similar to for the 2 µm beads. Again, isolated CD4$^+$ cells were stained with biotin antibodies and labeled with streptavidin beads. This resulted in non-labeled and labeled CD4$^+$ cell

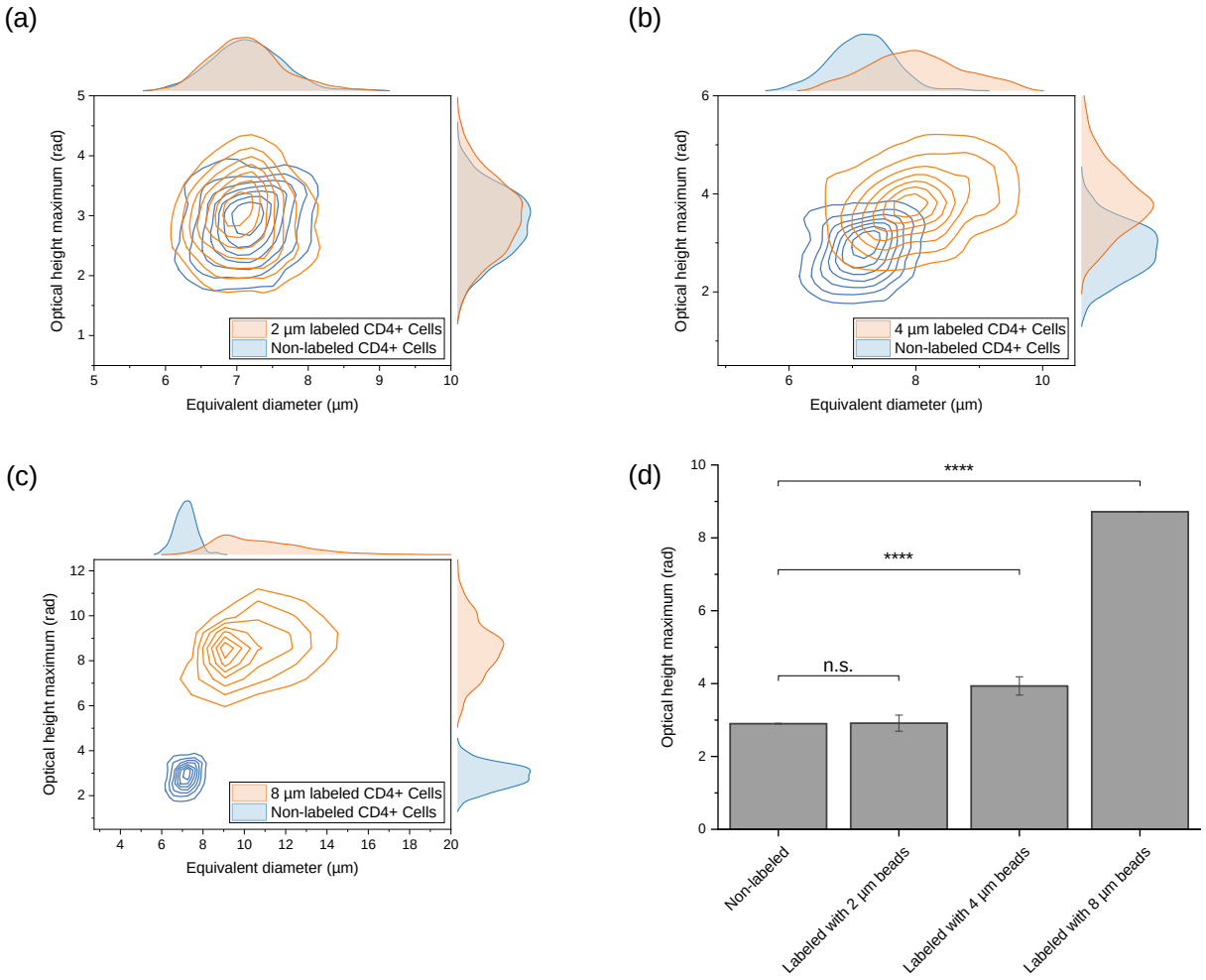

Figure 3.16: Labeling of CD4$^+$ T-cells with micrometre beads for cell differentiation. **(a)** Equivalent diameter and optical height maximum population of unlabeled cells (blue) and labeled cells with 2 µm magnetic polystyrene beads (orange). **(b)** Comparison of unlabled CD4$^+$ cells (blue) with CD4$^+$ cells labeled with 4 µm magnetic polystyrene beads (orange). **(c)** Induced equivalent diameter and optical height maximum change through labeling with 8 µm magnetic polystyrene beads compared to unlabeled cells. **(d)** Difference in average median maximum optical height of the non-labeled and labeled population. Significant differences between unlabeled cells and labeling of 4 µm ($p < 0.0001$) and 8 µm ($p < 0.0001$) could be observed. Significant levels are indicated by asterisks, with $^* = p < 0.05$; $^{**} = p < 0.01$; $^{***} = p < 0.001$, and $^{****} = p < 0.0001$.

populations. The single groups were extracted by differences in circularity, homogeneity, ED, and OHM. In five independent measurements, a total of 1275 non-labeled and labeled CD4$^+$ cells were analysed and compared in Figure 3.16b and d. The labeled population showed an increase in both the ED and OHM compared to the untouched cells while still containing an overlap of both populations. The median OHM increased from 2.91 rad

for untouched to 3.94 rad for labeled $CD4^+$ cells resulting in a significant difference with $p < 0.0001$.

Lastly, labeling with **8 µm magnetic polystyrene beads** was also analysed in the same way as beads of other sizes. However, another difficulty arose in the preprocessing of the population due to the similar size of the target cells and the beads. This problem could be tackled for single objects by the differences in OHM and for aggregates by looking at the homogeneity and optical volume of the accumulation. Cell-bead aggregates showed a homogeneity smaller than 0.45 and an optical volume of 10 to 60 μm^3. In two independent measurements, 1160 objects for each population were analysed in Figure 3.16c. Similar to the previous labeling experiment, differences between the non-labeled and labeled populations could be seen. This time, not only a slight increase but a clear separation was observable. This is also emphasised in 3.16d where the median OHM rose from 2.91 rad for untouched to 8.72 rad for labeled $CD4^+$ cells. Again, the difference is highly significant with $p < 0.0001$. A patent application has been filed describing the results of the investigations [217].

3.8 Discussion

3.8.1 Microfluidic Cell Manipulation

An unprecedented effort has been made to understand the advantageous and disadvantageous influences of the microfluidic system on blood cells. While the benefits of introducing such a system are undeniable, it is also important to localise negative effects in order to minimise them. One of them is the **shear rate induced activation** of blood cells, which can lead to falsification of the sample. It was shown that certain shear rates regularly induce a natural deformation of the blood cells in the human body [153]. However, these shear rates should not be too high as this can lead to undesirable effects. Platelets can be activated by high shear rates, subsequently leading to the formation of aggregates and thrombi [154, 155], and in extreme cases, high shear rates can lead to fragmentation of blood cells [156]. Lipowsky et al. showed great shear rate differences in the physiological conditions of various blood vessels. For large veins this value was below $100\,s^{-1}$, for the ascending aorta at $250\,s^{-1}$, and for arterioles higher than $1{,}500\,s^{-1}$ [157, 158]. A similar broad distribution can also be observed when looking at the blood flow velocity in the human body. The mean blood flow velocity in cerebral capillaries was found to be at a low $0.79 \pm 0.03\,mm/s$ [159] compared to peak velocities in ventricular systole from $300 - 450\,mm/s$ [160]. In FEM simulations for this system, a maximum flow velocity of $103\,mm/s$ and centre shear rate of around $600\,s^{-1}$ could be obtained. This lies within the highlighted physiological range.

Additionally, the **influence of the measurement medium** on the platelet activation was investigated. This was performed at two levels, measuring the expression of platelet activation markers and measuring the aggregates that are a result of the activation. Platelets stored in lower PEO concentrations showed no formation of additional aggregates within a time frame of 120 minutes. This was in line with reference results, where platelets were stored in PBS. It can therefore be assumed that the storage of blood platelets in low PEO solutions has no additional influence compared to PBS. This assumption is supported by the measurement of P-selectin, where no difference between PEO and PBS could be seen either. In contrast, for higher PEO concentrations with $0.15\,\%$ and $0.2\,\%$, a steep increase of P-Aggregates could be observed. These dynamics were comparable to experiments where a platelet-activating substance was used, which will be evaluated in the following chapters.

The measurement of the activation markers before and after the sample passes the fluidic chip allows a characterisation of the whole **fluidic setup**. This includes influences of the fluidic, the measurement media, and other factors. If the system has an influence, the fluorescence values of the individual activation markers should increase. For P-selectin, the opposite was the case. Here, the values decreased compared to before the fluidics. The slight decrease in the values can only be explained by measurement inaccuracies. In the case of CD71, which is a T-cell activation marker, a slight increase of fluorescence intensity compared to before the fluidic could be observed. However, it is debatable whether this increase from $1.77\,\%$ to $2.35\,\%$ is significant.

A high cell density in the sample can lead to **overlapping cells** that are mistakenly detected as aggregates. To counter this, a suitable dilution factor was investigated, allowing for the detection of single platelets while not introducing a too sparse cell distribution. By looking at the number of single platelets, it could be seen that for a dilution of 1:75 or 1:100 stable value was reached. Without overlapping, a stable value of single platelets is expected independently of the dilution. In contrast, a reduction of detected single platelets indicates a loss through overlapping. Since the cell numbers can increase in patients with specific diseases [161], a higher dilution of 1:100 was chosen for further experiments.

Viscoelastic cell focusing can also be used for the **uniformed alignment of erythrocytes** [162]. This is of high importance when analysing diseases that influence the red blood cell morphology, as in the case of malaria [163], hereditary disorders [164], and sickle cell anaemia [165]. If no uniform alignment is possible, additional time-consuming sample preparation methods are needed to compensate for it [22]. In this work, two polymer solutions were tested regarding their erythrocyte alignment performance. Here, the 0.05 % PEO solution showed better results than the 0.9 % PVP solution. This finding is in line with the work of Asghari et al., where they simulated three different polymer solutions for the viscoelastic focusing [166]. Here they stated that PVP has a lower N_1 gradient and, with that, induces a lower elastic force than PEO. This resulted in a worse cell focusing, which properties can be compared to the alignment of erythrocytes. In addition to the orientation of the erythrocytes, the focusing of all the blood cells in one focal plane is important for measurements without the need for autofocus readjustment. As discussed by Asghari et al., PEO performs here superior to PVP. This fact, together with the activability of blood cells, led to the use of a 0.05 % PEO solution to focus the cells. The mean value of 92.09 % of cells in focus was reached by combining the viscoelastic medium with the hydrodynamic focusing geometry of the Fraunhofer channel. Here, it should be noted that an objective classification of cells in or out of focus is difficult. In this work, the threshold of the mean focus measure was set by comparing cell images with associated different values. The decision criteria were the cell contrast and the contour sharpness.

3.8.2 Cell Concentration Measurements

Cell concentration measurements of erythrocytes without using reference beads showed moderate results. On the one side, the mean results over four experiments showed a good correlation between the dilution factor and the erythrocytes per frame. On the other side, this needed precise pipetting of skilled personnel. Additionally, even when this requirement was met, some outliers still occurred. This is also visible when looking at the standard deviation between all four measurements. While the problem of outliers can be handled through automation of the system and multiple measurements, another error source can occur due to the system's ageing. Several factors can influence the number of cells per image when using a microfluidic geometry. Examples are the clotting of tubes, the sedimentation of cells, the wear and tear of the syringe pumps, and increased

amounts of air bubbles through leakages. One possibility for bypassing these problems is introducing a reference system to the sample. Every preprocessing error will then influence not only the sample but also the reference in the same way. Decreased numbers of cells through clotted tubes occur in parallel with lower counts of reference beads. The overall concentration, which is dependent on the ratio between cells and beads, will not be affected. The introduction of such a reference bead allowed a high correlation between the measured concentration between the here presented method and the values obtained by a reference method. This was especially dominant for leukocytes ($R^2 = 0.99$) and platelets ($R^2 = 0.98$). A slightly smaller coefficient of determination ($R^2 = 0.96$) was seen for erythrocytes. Differences in performance may be explained by the fixed concentration of $7.45 \cdot 10^3\,\mu L^{-1}$ for the reference beads in all samples. This concentration approximately meets the concentration of leukocytes in whole blood while being roughly a fiftieth of platelets and one-thousandths of erythrocytes. Additionally, a slight difference in absolute concentration numbers between both measurement methods could be seen. This might be explained by using different sample preparation and imaging methods. Even between established haematology analysers, an absolute number comparison shows considerable differences [145].

3.8.3 Influence of Sample Preparation on Cell Morphologies

Erythrocyte lysis buffers are commonly used in cell analysis to simply remove predominant erythrocytes in a sample [167]. However, so far, the impact of lysis buffer on cells has only been studied for the qualitative change of flow cytometry parameters, such as the fluorescence intensity [139]. Here, we looked at the morphological changes of leukocytes when using different extraction methods and lysis incubation times. It could be seen that with increasing incubation time, leukocytes seem to be more affected. Intracellular uptake of lysis buffer and efflux of intracellular components may explain the increase in ED and decrease in OHM in granulocytes and monocytes over time. One explanation why lymphocytes, compared to other leukocytes, were less affected could be the higher ratio of nucleus to plasma, which limits the uptake of lysis buffer. In contrast, granulocytes and monocytes with a lower nucleus/plasma ratio were more affected. A higher uptake of lysis buffer could lead to cell swelling and therefore increase in size and decrease in their induced optical phase shift. While using a lysis buffer induced morphological changes in the leukocytes, no significant influence on the relative percentages of the different populations could be observed. However, a small difference could be observed when comparing the percentages of the three leukocyte subpopulations measured in the fluorescent flow cytometer with the numbers obtained by a Sysmex XN-350. Especially for monocytes, this difference was noteworthy. One explanation for the offset could again be the usage of different preanalytical and analytical methods. This starts with using varying lysis buffers, continues with other microfluidic geometries, and ends with different sensors.

3.8.4 Development of a Calibrator System

Calibrator systems for haematology analysers usually have similar properties and origins as the actual sample. As previously discussed, in many cases, the use of blood samples of healthy donors is still state of the art [148, 149]. The here presented **sphered erythrocytes** showing similar characteristics. They are also obtained from the blood of a healthy donor and are one blood cell type of a whole blood sample. Three different samples have been measured over a duration of 33 days. Quality criteria for the suitability as calibrator were the similarity to the actual samples and the long time stability of morphological properties measured by the optical volume. Since the similarity is given just by looking at the sample's origin, here, the main focus is on the changes in optical volume. The optical volume showed similar properties for all three samples, whereby it should be noted that for sample 2, a lower range of the mean values could be seen. Nevertheless, no trend in increasing or decreasing optical volume over time could be observed, highlighting the stability of sphered erythrocytes. However, a slight increase in the coefficient of variation throughout 33 was seen, which indicates an increased heterogeneity of the sample.

In contrast to human erythrocytes, **chicken erythrocytes** contain a nucleus. This allows a three-point calibration between the medium (n_1), the cytoplasm (n_2), and the nucleus (n_3). In this work, it was shown that chicken erythrocytes induce a phase shift similar to human blood cells. The OHM of the cytoplasm with 2.30 rad is comparable to human erythrocytes and the nucleus with 3.25 rad to human lymphocytes. This may prove the similarity to the measurement sample, but no ageing measurements showing the stability of the cells were performed in this work. To be able to consider chicken erythrocytes as a reliable calibrator, such measurements need to be completed in future work. Due to the high availability of chicken erythrocytes, it could provide an alternative to human blood samples.

Lastly, **droplets** were tested as possible calibrator material. These synthetic structures showed no direct similarity to the biological samples. However, for QPI, mainly two properties of the sample influence the induced phase shift: the refraction index and the height. Both parameters can be adjusted for droplets by the choice of liquids and geometry for the droplet creation. In this and other works, it could be shown that both a single droplet with one phase shift and droplets in droplets with multiple phase shifts can be created. One is similar to sphered human erythrocytes, the other is similar to cells with a nucleus like chicken erythrocytes. However, stability measurements were only performed for single droplets. This time, the morphology of the calibrator was characterised by looking at the object's diameter. Again, the sample was stored for over 30 days at room temperature. Throughout storage, no big changes in the mean diameter occurred. However, an increased amount of outliers, combined with an increase in the coefficient of variation, indicated a higher sample heterogeneity. The coefficient of variation between 1.96 % and 2.42 % cannot directly be compared to the one of sphered erythrocytes which refers to a volumetric size. A rough estimation can be achieved by calculating the third root of the values. Considering this, the adjusted coefficient of variation for sphered erythrocytes is between 2.63 % and 3.22 %. Even with the outliers of droplet diameter after 31 days, still, a similar homogeneity of the sample as for sphered erythrocytes can be

seen, highlighting the stability of the marker within this time frame. However, a significant difference in the biological sample is still seen when looking at the induced phase shift of the analysed droplets. For some blood cells, the OHM can go up to a value of 6.00 rad compared to the minimum OHM of 15.29 rad for smaller droplets. This discrepancy can be explained by size difference and the use of an oil with a refractive index of 1.467. For further work, both a reduction of size to a diameter of approximately 10 µm and using an oil or oil suspension with a lower refractive index can improve the results in this regard. Using a synthetically created calibrator has many advantages compared to its biological counterparts. It allows high reproducibility, a fast adjustment for different samples, and independence from human or animal donors.

3.8.5 Improved Leukocyte Subtyping through Targeted Cell Labeling

The usage of DHM allows a label-free detection of parasitic infections [22] and haematological diseases such as leukaemia [23]. This can be achieved by the high contrast, allowing even for a five-part differential, including monocytes, lymphocytes, neutrophils, eosinophils, and basophils [23]. However, some blood cells are not distinguishable because of their similar morphological properties. One example are subtypes of lymphocytes, including $CD4^+$ T, $CD8^+$ T, and B cells, which are important for the adaptive immune response and can therefore serve as a crucial marker for understanding pathophysiological processing in human diseases [168]. To broaden the application of DHM and make it even more beneficial for clinical diagnostics, a new labeling method was investigated that allows a high throughput differentiation of, e.g., lymphocytes. $CD4^+$ cells were labeled using magnetic polystyrene beads with a diameter of 2, 4, and 8 µm. As non-labeled reference served $CD4^+$ of the same sample to ensure comparability. Using 2 µm beads for labeling did not lead to a significant difference in ED or OHM. This was somehow expectable because the induced phase shift of these beads was a factor 0.36 lower than that of $CD4^+$ T cells. However, using bigger beads with a diameter of 4 µm and 8 µm induced a clear increase, both in ED and in OHM. 4 µm beads led to 33.15 % higher OHM values, whereas for 8 µm this growth was at 194.82 %. Again these results were expected as the mean optical height of the 4 µm and 8 µm beads was 1.24 and 2.72 times higher than that of the $CD4^+$ cells. However, when looking at the cell populations in Figure 3.16, it can be seen that for labeling with 4 µm cells, both populations are still overlapping. Only for labeling with 8 µm beads a clear differentiation between non-labeled and labeled beads is observable. Since no morphological differences between unlabeled $CD4^+$ and B cells could be observed, similar pictures are expected when comparing B cells to the labeled sample. As a result, it is possible to differentiate between subtypes of lymphocytes when using such a labeling approach.

4 Influences on Blood Cell Aggregates as a new Biomarker Class

4.1 Motivation and Problem Statement

The analysis of processes in haemostasis is a crucial field for medical diagnostics. Results can be used for patient treatment, intervention monitoring, or simple disease detection [169, 170]. By understanding these physiological mechanisms, dysfunctions can be detected and traced back to a possible cause.

There are many approaches to haemostaseological diagnostics, ranging from the measurement of plasmatic coagulation to the study of primary haemostasis and fibrinolysis. These include the measurement of plasmatic coagulation factors such as Factor II, V, VII, VIII, IX, X, XI, and XII and simple whole blood coagulation measurements such as the prothrombin time [171]. In addition, the primary haemostasis can be analysed by factors such as the von Willebrand factor [172]. As sample material usually serves venous blood and is either measured directly or after the extraction of platelet-rich plasma [173]. But also platelet functions can be analysed with various techniques. Alan D. Michelson discussed in his work the advantages and disadvantages of suitable methods [174]. Here, he looked at optical measurement techniques like platelet aggregometry, cost-efficient and fast approaches like impedance aggregometry, techniques to measure surface proteins like P-selectin, and measurements of LP-Aggregates with a fluorescence flow cytometer. He concluded his work by saying that every method has its advantages and disadvantages. However, a closer look at the drawbacks reveals that many of the presented techniques that Michelson investigated suffer from similar problems. One of them is that an excessive amount of sample preparation is needed. In many cases, additionally, the physiological processes can only be measured after an agonist is added. Direct measurement of haemostaseological processes with small volumes of blood is limited. P-selectin enables a direct measurement of platelet aggregation but has the disadvantage that P-selectin-positive platelets bind very rapidly to leukocytes via their expressed counter receptors. This instability limits the sensitivity of the marker. Therefore, the direct measurement of circulating aggregates promises to be are more sensitive marker than P-selectin–positive platelets [174]. Additionally, aggregates can also serve as a marker in inflammatory and infectious processes.

Aggregates can be measured using different techniques. The gold standard is the use of the so-called blood smear analysis [97]. Here, blood cells are presented on a glass slide in

a mononuclear layer, labeled by different kinds of stains, and examined under a transmission microscope. This method provides suitable contrast and high spatial resolution while requiring trained personnel and time-consuming sample preparation. Another disadvantage is the low number of examined cells through this manual process. The number of leucocytes examined usually never exceeds 200 [175]. Fluorescent flow cytometry allows rapid cell analysis and, therefore, a statistically relevant number of tens of thousands of cells within a few minutes. The specific binding of fluorescent dye-labeled antibodies to the respective surface proteins of the target cells allows an accurate cell identification [14]. This allows a qualitative analysis of LP-Aggregates, but the low spatial resolution of the system makes the detection of small P-Aggregates and a quantitative analysis of all aggregates difficult. The AMNIS imaging flow cytometer combines a brightfield microscope with a fluorescent flow cytometer, enabling high spatial information with suitable throughout of around 20,000 cells per minute [176]. The main disadvantage is the system's high cost and the need for fluorescent antibodies to detect aggregates. These drawbacks, in combination with its complexity, hinder its use in routine diagnostics.

This chapter discusses the use of the previously described measurement setup for measuring **blood cell aggregates**. Similar to the AMNIS approach, a combination of a microscope with a microfluidic system combines the high spatial resolution of an imaging technique with the level of automation in fluorescent flow cytometry. Using a quantitative phase imaging device enables a suitable contrast that overcomes tedious sample preparation, such as fluorescent labeling by trained users. An additional combination with an adapted image analysis allows a quantitative and qualitative analysis of blood cell aggregates. Down the road, this allows an in-depth characterisation of the new biomarker class. It is essential to measure dynamics in the formation and decay as well as influencing variables. Only when such a characterisation was performed precise statements about the biomarker in a clinical question can be made.

The arguments and findings presented in this chapter are partly based on our previously published work [208].

4.2 Methodology

The setup used for measuring blood cell aggregates was described in previous chapters 3.2.2. The medium for cell analysis contains 0.05 % (w/v) of PEO in PBS. The microscopic and microfluidic chip design is the same as in previous chapters. This methodology section begins with a description of the sample preparation followed by an in-depth specification of the protocols used to activate platelets. To analyse aggregate images, a combination of common image analysis combined with machine learning approaches is needed. This part is highlighted in the last chapter of the methodology.

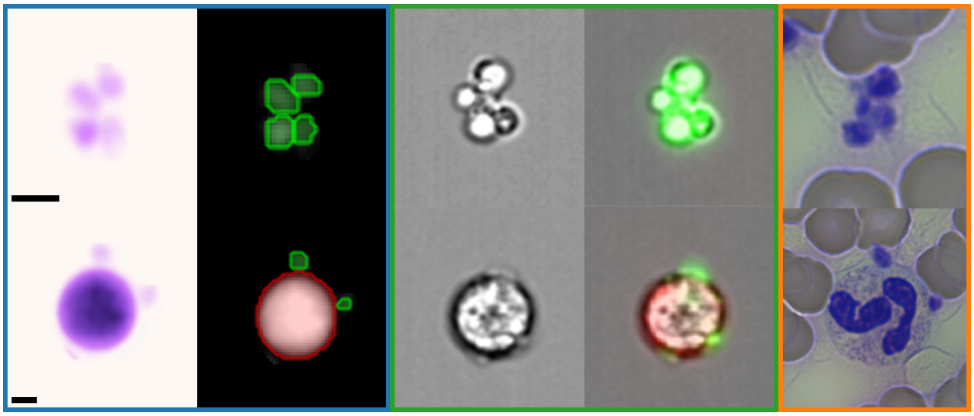

Figure 4.1: Example images of platelet aggregates (top row) and leukocyte-platelet aggregates (bottom row) captured with different imaging devices. In the blue box, patches of quantitative phase contrast images are shown in false colour (left) and after classification (right). The red circles correspond to a classified and segmented leukocyte, while the green is linked to platelets. In the green box are images obtained with an AMNIS imaging flow cytometer. Here, on the left are brightfield images, and on the right, merged brightfield images with the corresponding fluorescence patches. Green is the excited fluorescent signal of platelets (CD61), and red is those of leukocytes (CD45). In the orange box are shown example pictures obtained by blood smear analysis. Both scale bars correspond to 5 µm. Image adapted from [207].

4.2.1 Sample Preparation

Venous blood samples were collected from healthy donors using EDTA, citrate, heparin, and hirudin S-Monovette® tubes from Sarstedt. Samples were measured either as diluted whole blood samples or after extraction of platelets. For the **whole blood measurements**, blood was diluted in the medium for cell analysis to a final dilution of 1:100. **Platelets** were extracted by a two-step protocol. First, 1.50 mL of whole blood was centrifuged for five minutes at $200 \times g$. After this step, red and white blood cells are located at the bottom of the tube, whereas the plasma and platelets lie above the sedimented cells. Second, the supernatant is transferred to another tube and centrifuged at $800 \times g$ for another five minutes. After this step, the platelets are located in the pellet at the bottom of the tube. Third, the supernatant is removed, and the pellet is resuspended in 2.25 mL of the cell analysis medium.

Additionally to the blood sample also **platelet concentrates** were analysed. These concentrates were excluded from the clinical storage due to exceeding the expiration date. For the reference measurements with a Fluorescence-Activated Cell Sorting (FACS), the concentrates were diluted 1:10 in PBS. For DHM measurements, the same dilution was applied but with the 0.05 % PEO measurements solution. Because the samples were measured over a duration of several days, the concentrates were stored in citrate-coated

bags at room temperature. The additional usage of a moving plate with a low velocity prevents cell sedimentation and aggregation.

4.2.2 Activation Protocol for Platelets

Several preparation steps were needed for the in-vitro activation of whole blood samples (Figure 4.2). After the blood draw, the sample was diluted in PBS with a concentration of 1:2 and mixed at a temperature of 37 °C for three minutes to obtain a homogeneous solution at physiological conditions. ADP with a final concentration of 0.33 µM, 1.61 µM or 6.45 µM was added as a activator. These steps were adapted from previously published work to achieve comparability to state-of-the-art analyser [78]. Afterwards, a final concentration of blood cells of 1:100 needs to be met. This is achieved by an additional 1:50 dilution step of the activated sample with the measurement solution.

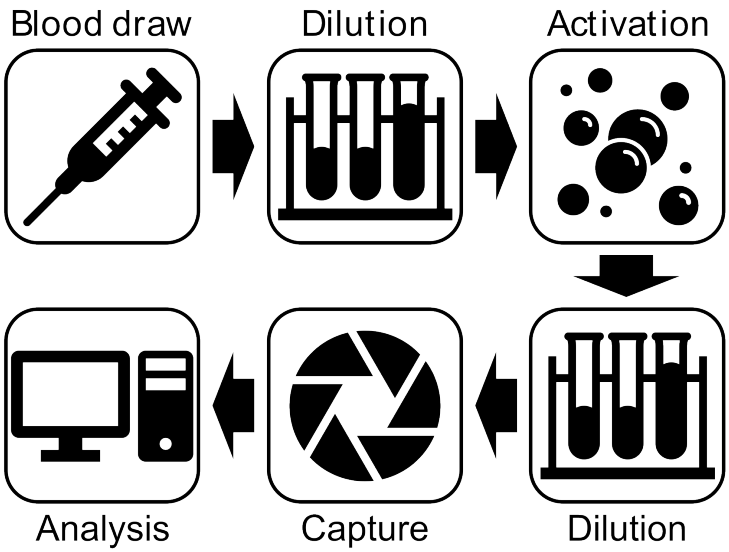

Figure 4.2: Sample preparation steps for the in-vitro activation of whole blood samples. Figure adapted from [208].

4.2.3 Image Analysis of Single Cells and Aggregates

The subsequent image analysis of the obtained images was performed in three distinct steps: preprocessing, segmentation & classification of cells, and the analysis of the detected objects.

- The raw images obtained from the measurement still contain many artefacts and unwanted properties. Therefore, first, a **background subtraction** similar as in chapter 3.2.4 is performed. Also, here the median of the first images, which results in the background of the capture, is subtracted from each image. Single or clustered objects are detected by using a **threshold segmentation** with a value of 0.45.

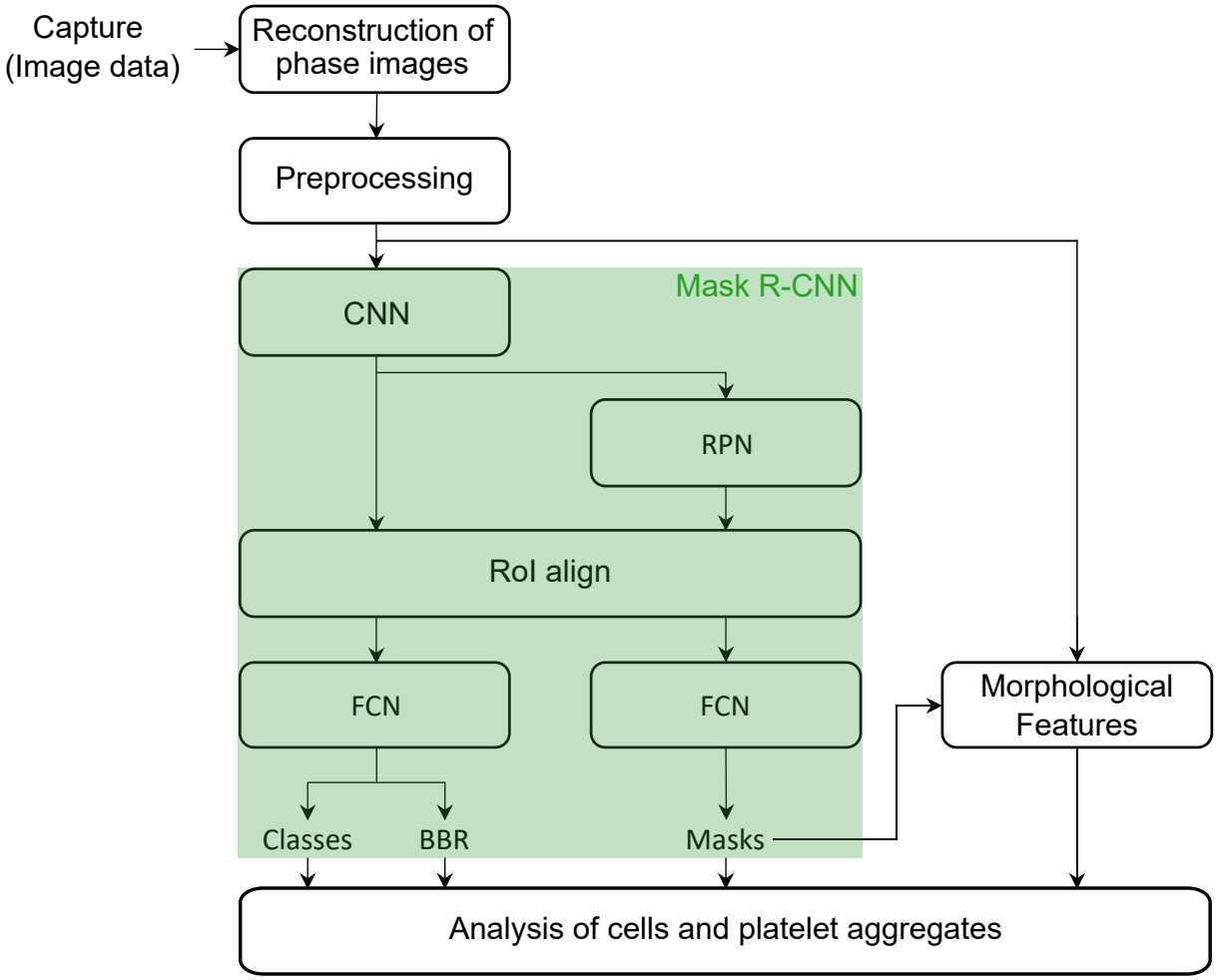

Figure 4.3: Flow diagram of the image analysis. After reconstruction of the phase images, preprocessing steps like noise reduction and rescaling are performed. Then a Mask R-CNN approach, highlighted in green, in combination with the calculation of morphological features, is used for an in-depth analysis of cells and blood cell aggregates. Figure adapted from [208].

Similar to the work of Suzuki et al. [177], the contours of the detected objects were extracted. Each component (represented by a contour) was then saved as a smaller image section for further processing. In order to filter out remaining small artefacts or debris, a suitable **size filter** was implemented and applied to the contours. The last essential preprocessing step is the **normalization**. First, the value range of the images is clipped to limit the unlimited value range of DHM phase images. Then, a min-max normalisation is used to transform the image values into the range $0-1$. This is then a suitable format for neural networks.

- **Segmentation and classification** allows the identification of single cells, aggregates, and their components. Here, based on the rough threshold segmentation contours, a second stage Mask R-CNN model [178] is used for refining the individual subobjects. **Mask R-CNN** performs both object detection and object mask

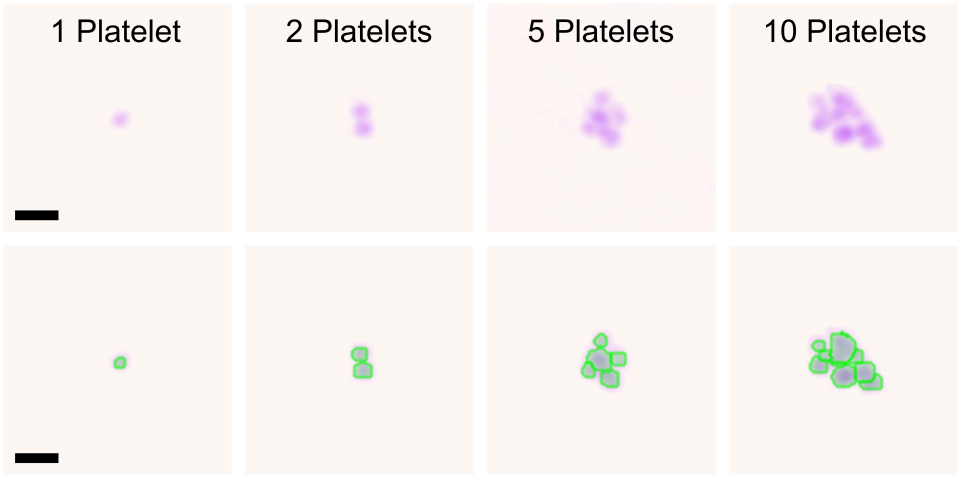

Figure 4.4: Example patches showing single platelets and platelet aggregates of various sizes. In the top row are quantitative phase contrast images in false colour. The bottom row shows the same patches overlaid by the segmentation and classification results. The highlighted edges represent one segmented cell's borders, while green corresponds with a classified platelet. The scale bar is 5 µm. Figure adapted from [208].

computation simultaneously and is based on the Faster R-CNN [179]. This method operates in four stages: first, a convolutional network (backbone) provides a convolutional feature map based on the input images. For the classification of blood cells in this work, a ResNet50 [180] is used as the backbone. In the second step, a Region Proposal Network (RPN) provides Regions of Interest (RoI). This can be achieved by sliding a small network over the convolutional feature map. As a third step, a RoI align layer provides feature maps in the same size as the RoI by bilinear interpolation. These maps can then be used for classification and bounding box regression. In parallel, a small Fully Convolutional Network (FCN) is applied to each RoI to predict the individual object masks on a pixel-by-pixel scale. The performance and reliability of the neural network are highly dependent on the quality, amount, and selection of training data. Therefore, a high amount of ground truth **training data** is needed. However, manually labeling cell patches is time-consuming and, in some cases, not possible because of the low-contrast images. Therefore training data was generated in two steps. First, subpopulations of blood cells were extracted out of whole blood. In the case of platelets, this was performed as described in chapter 4.2.1. Erythrocytes were extracted by measurement of whole blood samples combined with a suitable size filter. This allows the removal of small platelets and bigger doublets and triplets. The remaining cells have more than 99 % purity erythrocytes. Subtypes of white blood cells could be extracted using Miltenyi Biotec MACSxpress® kits as described in chapter 3.2.5. The different cells were measured within one hour after the successful extraction. Secondly, after creating a labeled dataset of single cells, synthetic aggregates were created by composing multiple classified single-cell images together. These synthetic aggregates, together with the

single cells, were used to train the network. In total, there were 200,000 cells in the training dataset. The performance of the trained network was evaluated on both computer-generated aggregates as well as manually labeled images. Parallel to the evaluation with the Mask R-CNN approach, simple morphological features of the cells are also calculated. This is performed based on the simple threshold segmentation but also based on the contours provided by the Mask R-CNN. The morphological feature extraction process is described in more detail in chapter 3.2.4.

- The last step of the processing pipeline is the **analysis of the single cells and aggregates**. Here, the segmentation and classification results were combined with the information provided by the morphological features. This allows the categorisation of each patch as a single cell or an aggregate. Additionally, the amount, the category, and the morphology of the involved cells can be extracted for each patch. All image analysis tools were written in Python 3.8.8 8 (Python Software Foundation), morphological features were adapted from OpenCV 4.5.5 [181], and the neural network components were created in Tensorflow 2.8 [182].

4.2.4 Fluorescence Flow Cytometry Measurements

Fluorescence flow cytometry measurements were performed with the MACSQuant Analyzer 10 from Miltenyi Biotec B.V. & CO. KG. Cells were labeled with human CD41, CD61, and CD62P antibodies. Those correspond to Integrin α-IIb, Integrin β-3, and P-selectin, which are expressed by platelets. In the unactivated state, P-selectin is stored in the α-granules of the platelets and is only expressed to the platelet surface when an activation of them occurs. First, a suitable amount of antibodies was determined by performing titration experiments where a saturation of the titration curve was reached. Using the titration curves, a value of 1 µL per 25 µL of the sample with a cell count of 50,000 was used for CD41 and CD61. For CD62P, half the volume of antibodies was used, resulting in 0.5 µL per 25 µL of sample.

Cell labeling includes adding antibodies to the sample, followed by a 15-minute incubation at 4 °C. Afterwards, the excess antibodies are removed by a washing step. Here, the cell suspension is centrifuged at $2,000 \times g$. After this step, a cell pellet is formed at the bottom of the tube. The supernatant, together with the excess of antibodies, is removed, and fresh PBS is used as media to resuspend the cell pellet. This step is repeated once before performing the fluorescence flow cytometry measurements. Measurement files were exported in the FCS format and analysed using Kaluza Analysis 2.1.

4.3 Effect of Sample Ageing on Platelet Aggregates

This chapter evaluates the influence of the sample age on the P-Aggregates. This can be performed on several levels and for different kinds of samples. Platelet concentrates after expiry and freshly drawn whole blood samples from healthy donors served as the

two case studies. The measured target variables include the number and composition of P-Aggregates.

4.3.1 Ageing of Platelet Concentrates

For patients with a low platelet concentration or no proper platelet function, the transfusion of platelet concentrates is important to reduce the risk of internal and external bleeding events. This can occur, for example, in patients treated with chemotherapeutics [183]. Dependent on the definition, these platelet concentrates have a limited shelf life of 72 - 120 hours. Afterwards, biochemical and physiological changes that occur during storage have a negative influence on patients' outcomes after transfusion [184].

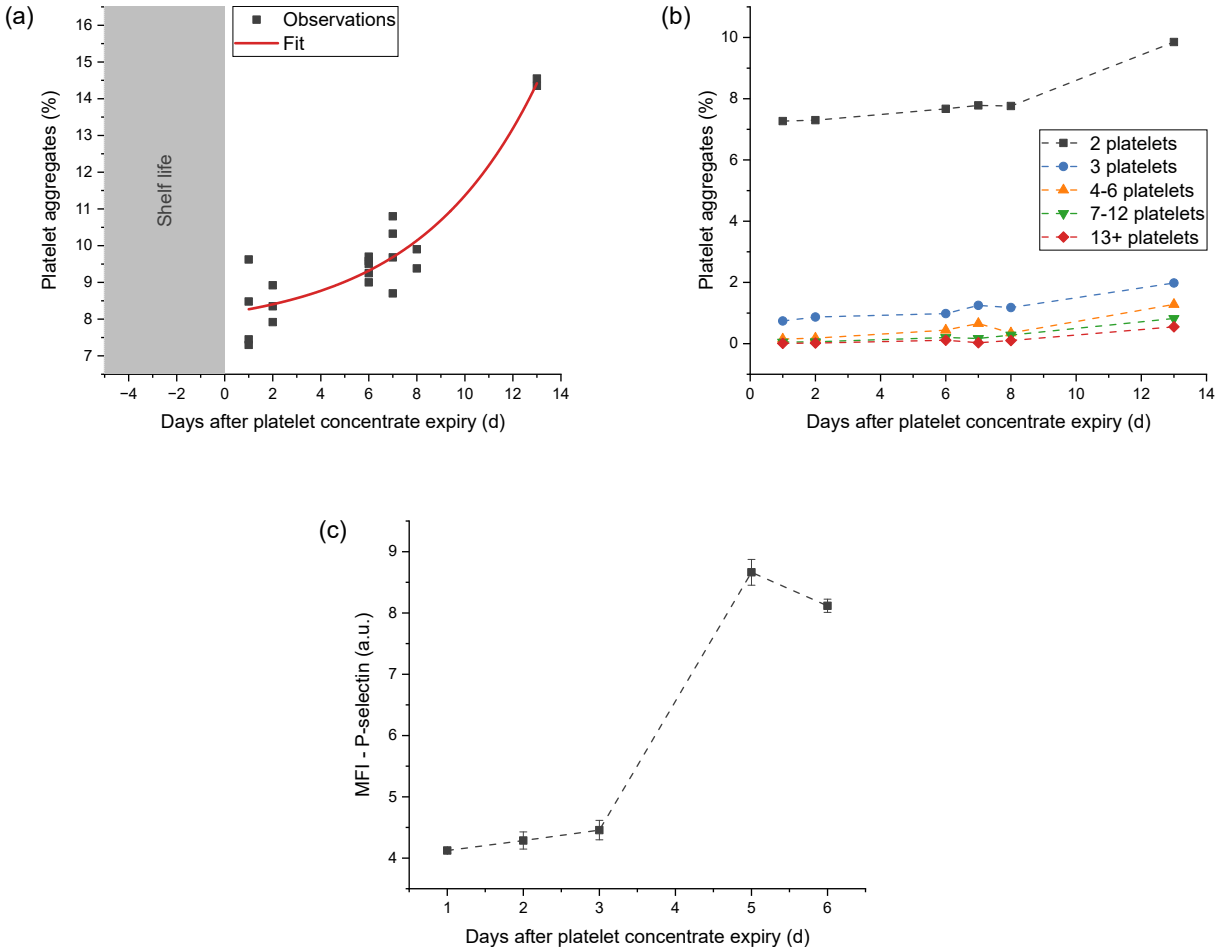

Figure 4.5: Ageing effects of platelet concentrates on platelet aggregate formation and platelet activation. **(a)** Increase in the measured amount of platelet aggregates over a storage time of 13 days with the corresponding exponential fit function. **(b)** Subdivision of the aggregates in (a) according to their composition. **(c)** The Mean fluorescent index (MFI) of the platelet activation marker P-selectin measured with a fluorescent flow cytometer.

Such changes in physiological properties, namely the development of P-Aggregates, were monitored in this experiment after the 120-hour shelf life of the concentrates had been reached. For this, platelet concentrates were measured on days 1, 2, 6, 7, 8, and 13 after expiry. For each day, three to five captures were recorded, each containing approximately $30,000$ platelets. In Figure 4.5a, the P-Aggregates are plotted against the days after concentrate expiry. The number of P-Aggregates describes the fraction of P-Aggregates compared to the total number of platelets. Each dot represents one single measurement. An exponential growth fit was performed based on the function of $y = y_0 + a \cdot exp((x - x_0)/b)$. The fitted model was $y = 7.66 + 0.03 \cdot exp((x + 13.70)/4.98)$. The coefficient of determination of $R^2 = 0.89$ and the p-value of $9.44 \cdot 10^{-8}$ showed a good fit to the obtained measurement data. Within the first 12 days after expiry, an exponential growth of P-Aggregates could be observed. The values increased from a medium of 8.21 % at day 1 to a value of 14.45 % at day 13. When comparing the mean composition of the aggregates over all captures, it could be seen that the main population of aggregates contained two platelets (Figure 4.5b). This effect was especially significant for the first two measurements where only 0.01 % and 0.02 % of all aggregates contained 13 or more platelets. Over the duration of the 13 measurement days, this number increased to 0.55 %. A similar trend could also be observed for aggregates containing 3, 4-6, and 7-12 platelets, whereby the increase was especially dominant for bigger P-Aggregates.

The rise in platelet activation over time could not only be monitored by measuring P-Aggregates but also by direct measurement of P-selectin on the platelet's surface. In Figure 4.5c, the MFI of P-selectin is plotted against the days after platelet concentrate expiry. Similar to the previous findings, also the MFI of P-selection increased in the first days only by a small margin. However, a steep spike in platelet activation could be seen after five days. Although there was an increase in both values over the measurement period, there are differences in timing and dynamics.

4.3.2 Influence of used Anticoagulants on Sample Ageing

In the previous chapter, solely the influence of the ageing on a citrated platelet sample was analysed by looking at the platelet activation and P-Aggregates. Here, the influence of different anticoagulants is also considered while measuring P-Aggregates. Additionally, the focus of this experiment was more on the highly dynamic processes after blood is drawn instead of monitoring a sample over a long period. For this, blood from four independent donors was anticoagulated in EDTA, citrate, heparin, and hirudin tubes. Measurements were performed over a duration of two hours while the sample was stored at room temperature. In Figure 4.6a, the progression for one exemplary donor is shown. The amount of P-Aggregates was measured after 0, 30, 60, 120, and 240 minutes, whereby the different anticoagulants are shown in different colours. 0 minutes was the defined starting point of the experiments, which was within a time window of 30 minutes after blood collection. For citrate, hirudin, and EDTA, all P-Aggregate values within the 240 minutes stably ranged between $0.50 - 3.00$ %. There were only two outliers for this donor: blood stored in heparin at minute 30 (5.71 %) and minute 60 (8.94 %). Results in Figure 4.6b

showed a similar pattern. In this figure, the aggregates of the ageing measurements were compared with the respective 0-min measurement. Differences of all patients were plotted on the Y-axis. Here, each plot represents a single measurement. In addition, the normal distribution fitted over all captures of a single group is displayed. For hirudin and EDTA, an expected distribution around the origin value could be observed. Similarly, as for donor one, heparin showed an increased aggregation compared to their 0-min measurements. In contrast, citrate showed a reduced aggregate number over time.

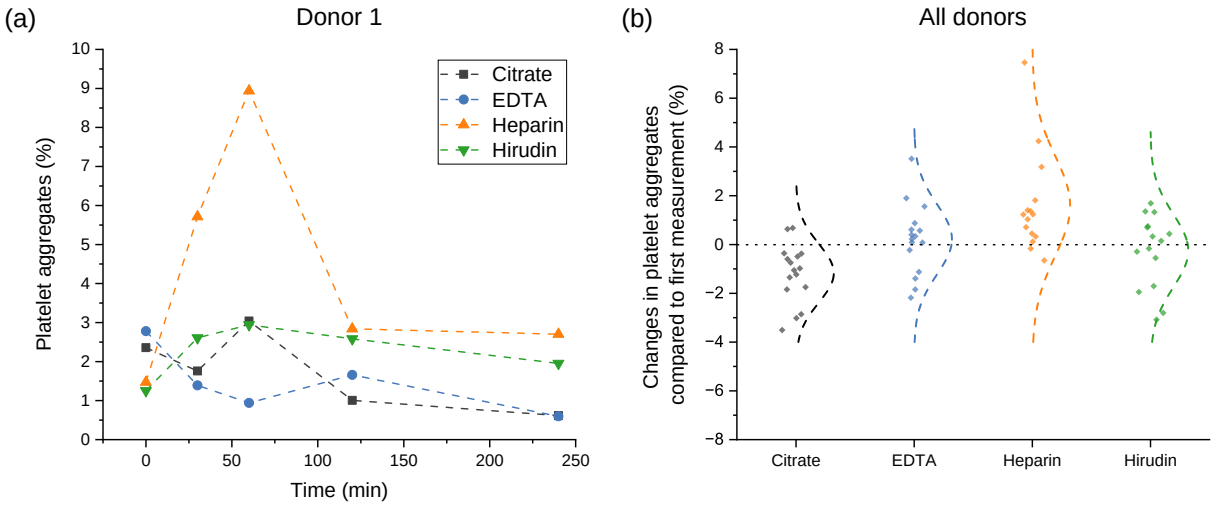

Figure 4.6: Ageing effects of whole blood samples stored in different blood collection tubes on platelet aggregate formation. **(a)** Exemplary data of P-Aggregates from the blood of one donor over a period of 240 minutes. **(b)** Difference in P-Aggregates for all donors of the 30-, 60-, 120-, and 240-minute captures compared to their respective 0-minute reference. Image adapted from [208].

4.4 In-vitro Activation of Platelets

This section analyses the effect of in-vitro activation assays on blood. For this purpose, the blood of three independent donors was stored in tubes with different anticoagulants before a subsequent activation with varying amounts of ADP. Observed target values were the number and composition of P-Aggregates both in formation and decay.

4.4.1 Effect of ADP Concentration

In a first step, the concentration of the activating substance ADP was varied to see if differences in platelet aggregation occurred and if the imaging device could monitor them. For this purpose a starting concentration of 6.45 µM was diluted to 1.61 µM and 0.33 µM. Hirudin was used as an anticoagulant for all samples. Captures were performed shortly

before activation (0 min) and on different points after activation (3, 7, and 12 min). At the start of the experiment, the blood sample had been taken no more than an hour earlier. Regardless of the used ADP concentration, an increase after activation can be observed at minute 3 (Figure 4.7a. This effect is especially dominant for 1.61 µM (24.28 %) and 6.45 µM (25.15 %) compared to the initial value (1.56 %). For 0.33 µM, only a small increase to 4.13 % was measured. At the third minute after activation, a peak in all concentrations was reached. Afterwards, the values decreased over time. A similar behaviour could also be observed when looking at the aggregate composition. In Figure 4.7b, the size distribution of the aggregates at minutes 0, 3, and 7 are shown for activation with 6.45 µM ADP. Before activation, most of the aggregates consisted of two or three platelets. Only a small fraction of 4.10 % consisted of more than three platelets. Directly after activation, this number increased to 21.10 %. Even big clots with ten or more platelets accounted for 2.20 % of the total aggregate number. During the decay of aggregates at minute 7, also the size distribution developed towards initial values. Here, already 84.70 % of all aggregates had two or three platelets, and the number of big aggregates disintegrated especially fast. At this point, no aggregates with ten or more platelets could be observed. The 12-minute measurement continues this trend.

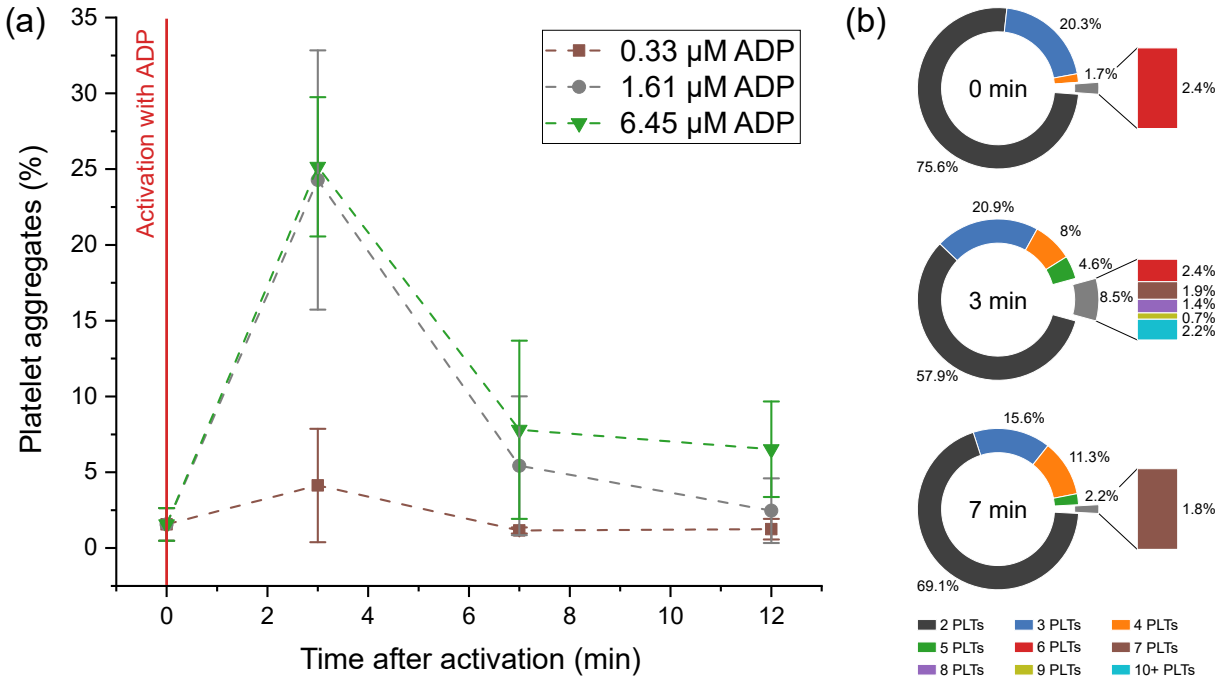

Figure 4.7: Impact of ADP concentration variation on the measured number and composition of P-Aggregates. **(a)** The dynamic process in the aggregate formation and decay over time varies dependent on the concentration of the used activator. **(b)** Composition of the P-Aggregates are shown for three different time points (0, 3, and 7 min) and an ADP concentration of 6.45 µM. Image adapted from [208].

4.4.2 Effect of Anticoagulants

As described in chapter 2.3.3, the choice of anticoagulants influences the activatability of blood cells. This is due to their intervention at different points of the coagulation cascade, which is true both for the direct activation after a blood draw and for an in-vitro activation with ADP or TRAP. To test whether these effects can also be observed when measuring P-Aggregates, differently anticoagulated blood samples were activated using a total ADP concentration of 6.45 µM. Again the blood samples were collected in tubes with either EDTA, citrate, heparin, and hirudin. In Figure 4.8a, the difference between the single measurement points and their respective zero measurements is plotted against the time after activation. Using this kind of illustration allows a direct observation of differences caused by the activation. When comparing the four different anticoagulants, one clear distinction between EDTA and the other anticoagulants could be seen. No significant increase in P-Aggregates through ADP activation was visible. In all three measurement points the increase ranged between 0.16 % and 0.66 %. This contrasted with the other measurements, where a sharp increase could be observed. Three minutes after activation, hirudin, heparin, and citrate values were close to each other, with values ranging between 21.68 % to 23.59 %. As shown before, this increase was followed by a drop at minutes seven and twelve. However, it is notable that this drop was most dominant in hirudin with 73.55 % reduction at seven and 78.89 % at twelve minutes, followed by citrate (62.23 % and 69.07 %) and heparin (37.33 % and 42.79 %).

4.4.3 Decay of Platelet Aggregates

The decay occurring after the initial spike can also be characterised by looking at the composition of aggregates. Since the decay effect was only visible for citrate, heparin, and hirudin, all those measurements were pooled. Figure 4.8b shows the disintegrated portion of P-Aggregates broken down by their size. Aggregates were analysed at the peak at minute three and compared to the last measurement at minute 12. Through this comparison, the number of decayed aggregates within nine minutes was obtained. Since only a fraction of the aggregates contain 11 or more platelets, only aggregates between two and ten platelets were considered. Within the nine minutes of analysis, the majority of P-Aggregates decayed for all sizes. Still, this effect was especially dominant for larger structures. The number of remaining clots with two, three, four, or five platelets ranged between 41.03 % and 45.59 %. In contrast, aggregates ranging from six to nine platelets showed a linear increase in disintegration, starting from 77.40 % and ending at 100.00 %. A deviation from this trend was observed for clots with ten platelets where only 95.58 % of the aggregates decayed. This may be due to a small amount of such large structures after 12 minutes and the associated measurement inaccuracy.

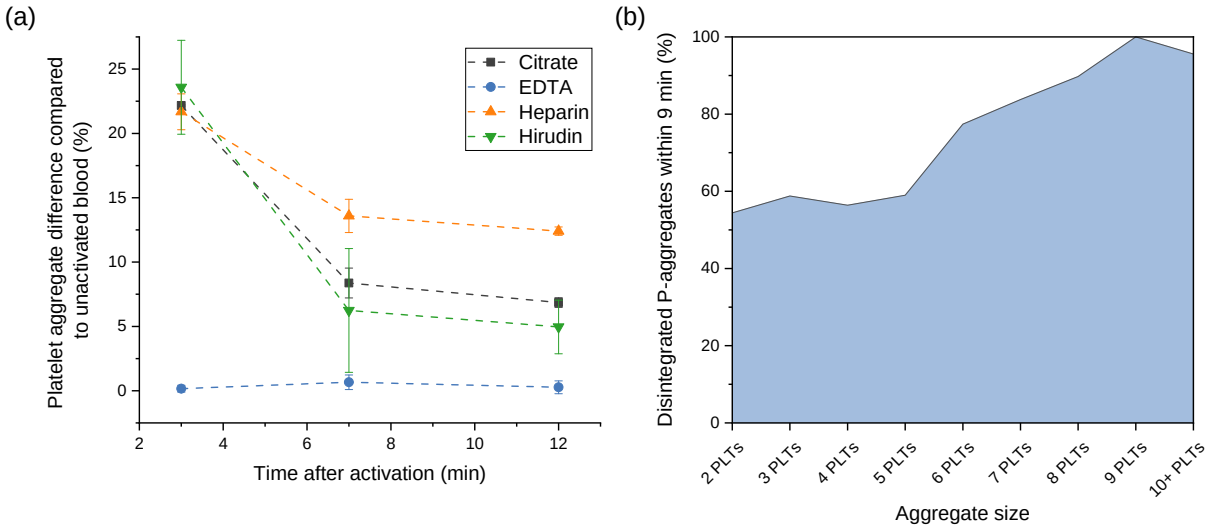

Figure 4.8: Influence of in-vitro activation on aggregate formation and decay while using differently anticoagulated blood samples. **(a)** P-Aggregates difference after activation compared to their respective unactivated blood measurement. Data contains measurements of three independent donors. **(b)** Aggregate decay by size between minutes three and twelve of the activation experiments. All measurements of heparin, hirudin, and citrate are pooled and then analysed together. Image adapted from [208].

4.5 Discussion

In this chapter, we proposed using our previously described measurement system to detect highly dynamic processes in aggregate formation and decay. First, the behaviour of a **platelet concentrate** was investigated when storing the sample over a duration of 13 days after expiry (Figure 4.5). The increase in P-Aggregates during storage followed an exponential growth, closely matching the results of the P-selectin measurements. However, the two values are not identical with respect to the time of increase and must therefore be considered independently. Result in P-Aggregates, and P-selectin also match previous publications [185, 186]. Here, the authors measured different platelet membrane proteins during a period of seven and ten days after donation. The exponential growth of the aggregates was visible for clots of all different sizes, although the dominant population was small clots containing only two platelets. Also noteworthy was the amount of aggregates with 13 or more platelets. On day one, after expiry, they only contributed to 0.01 % of all platelets. On the last measurement day, it increased to 0.55 %. These clots had a higher diameter than common blood cells and could block smaller vessels. This highlights why concentrates should not be used for transfusion after such a long storage.

Furthermore, the stability of the measurement was investigated for **freshly drawn blood** and over a duration of four hours. As shown in Figure 4.6 and 4.7, stable and reproducible measurements of blood were archived. Directly after the blood draw, the P-Aggregates laid between 0.50 % and 3.00 %, which showed similar results as in previously published data [187]. Here, Leytin et al. analysed the amount of P-selectin-positive platelets in the blood of healthy donors. These values correlated directly with the number of activated platelets and showed values of 1.02 ± 0.49 % for unactivated blood. Their obtained lower values can be explained by using different analysis techniques and measuring another marker. The number of measured P-Aggregates, and P-selectin-positive platelets are directly related, but this does not allow a direct comparability of the values. Michelson postulated that through the fast consumption of P-selectin-positive platelets into aggregates, the direct measurement of aggregates has a higher sensitivity [174, 188]. It can therefore be assumed that this higher sensitivity of aggregates also leads to slightly higher values compared to the P-selectin-positive platelets.

Blood samples stored in EDTA and hirudin showed stable behaviour without notable ageing effects within the 240 minutes. The measured P-Aggregates values only varied between ± 2.00 % and showed a normal distribution around their respective zero measurements (Figure 4.6b). For blood stored in heparin, an increased aggregate formation due to the sample's ageing could be seen. These effects were mostly observed shortly after blood was drawn (30 and 60 min, Figure 4.6a) and could therefore be due to the effects of the blood collection and subsequent lower anticoagulation with heparin. Blood stored in citrate, however, showed an opposite trend. Here, a disintegration of aggregates over time could be seen. For the four patient samples shown here, a clear trend for all four anticoagulants was observable. However, a higher statistical number of samples is needed to trace back fundamental processes.

To evaluate characteristics in P-Aggregate formation and decay, the **in-vitro activation**

experiment with ADP was performed. This allows insides into how fast these processes take place. When activating the same hirudin blood sample with different concentrations of ADP, an increased amount of aggregates could be seen for higher concentrations. However, it is noteworthy that the differences between 6.45 µM and 1.61 µM, shown in Figure 4.7, were much smaller than compared to the differences with 0.33 µM. This fact may be explained by a saturation that was reached for higher ADP concentrations. When a certain threshold is reached, no more platelets can be activated. It should also be emphasised that even at low concentrations of ADP, a formation of P-Aggregates can be seen. This is the case for ADP concentrations of 0.33 µM and 1.61 µM, which a significantly lower the 6.40 µM used in the microplate protocol. This indicates a possible higher sensitivity of the presented method compared to the established reference method. In addition, a higher temporal resolution can be considered as the test takes only 2 minutes. After initial activation, however, higher ADP concentrations lead to a slower decay of aggregates. When looking at the aggregate sizes, it could be seen that not only the amount of platelet changed but also the number of involved platelets. P-Aggregates in the measurement before the activation mainly consisted of two and three platelets. This changed considerably after activation. Therefore, it can be assumed that the ADP promoted platelet cohesion by fibrinogen, supporting the formation of small and even large aggregates.

A closer look at the effect of ADP **activation on anticoagulated blood** shows differences between the anticoagulants when comparing the measured P-Aggregates. Citrate, heparin, and hirudin allowed an in-vitro activation of blood with ADP. In contrast, when exposed to the activator, blood anticoagulated with EDTA showed no effect. These results align with the literature described in chapter 2.3.3. When investigating the speed of disintegration, dependent on the anticoagulant between 42.79 % to 79.98 % of all P-Aggregates decayed within nine minutes (Figure 4.7a and 4.8). The result can be compared to a study by Michelson et al. [188]. In this work, they activated platelet concentrates of baboons in-vitro, infused them into the animals, and measured the number of LP-Aggregates in the peripheral blood. 72.73 % of monocyte-platelet aggregates disintegrated in a time frame of ten minutes. Although the experimental setup, the analysed species, and the measured aggregates can not directly be compared to these results, similar physiological dynamics can be observed. When looking at the size of the decaying aggregates (Figure 4.8b), it could be seen that the proportion of large aggregates with more than six platelets dissolved faster than smaller aggregates. This behaviour can be explained by a homogeneous decay of all aggregates but a disintegration of bigger structures into smaller ones. From the results can be deduced that time-consuming sample preparation is not reliable for measuring these fast dynamics. To a more considerable extent, it can even induce a sample activation through sample handling and preparation [154, 155].

5 Clinical Study on Aggregates in COVID-19

5.1 Motivation and Problem Statement

COVID-19-associated coagulopathy leads to the formation of blood cell aggregates such as P-Aggregates and LP-Aggregates. Among others, this increased aggregate formation subsequently leads to life-threatening thromboembolic events. Early detection of increased numbers of aggregates in patients' blood may allow a quantitative evaluation of worsening conditions way before the complication occurs. More clinical studies need to be performed to validate if this biomarker has a diagnostic or even prognostic value. However, as described in chapter 4.1, there are many physiological and technological challenges when measuring these aggregates, like the ageing effect and the vulnerability of the biomarker. For this reason, not many publications show the correlation between blood cell aggregates and COVID-19 severity by measuring a statistically relevant amount of events [118]. Instead, mainly established biomarkers have been tested to evaluate the patient's health. Most of them were shown to be of limited informative value, which can be explained by a highly diverse patient cohort, especially at the Intensive Care Unit (ICU). Even the addition of modern data processing techniques to combine different established markers did not improve the results [107]. This highlights the need for novel diagnostic parameters such as blood cell aggregates. New biomarkers should be able to show an association with the patient's health status while at the same time allowing rapid near-patient testing. This is important to reflect the dynamic processes in the ICU and allow fast decision-making in life-threatening situations.

This chapter discusses how the previously described measurement setup was applied to measure and analyse blood cell aggregates in patients with COVID-19. Patients are sorted into different cohorts dependent on the WHO ordinal scale for clinical improvement for hospitalised patients with COVID-19. Additionally, a healthy cohort served as an internal reference. Eventually, the number of aggregates and their composition were analysed and compared for all cohorts.

The arguments and findings presented in this chapter are partly based on our previously submitted work [207] and part of a patent application [216].

5.2 Methodology

The setup, consisting of a microscope, a microfluidic channel, and subsequent image analysis, has already been described in previous chapters. As before, the measurement medium contains 0.05 % of PEO and 99.95 % of PBS. This methodology section begins by describing the study design and the involved steps in sample collection and transport. It ends with an in-depth description of the statistical analysis performed for biomarker correlation and significance evaluation.

5.2.1 Study Design

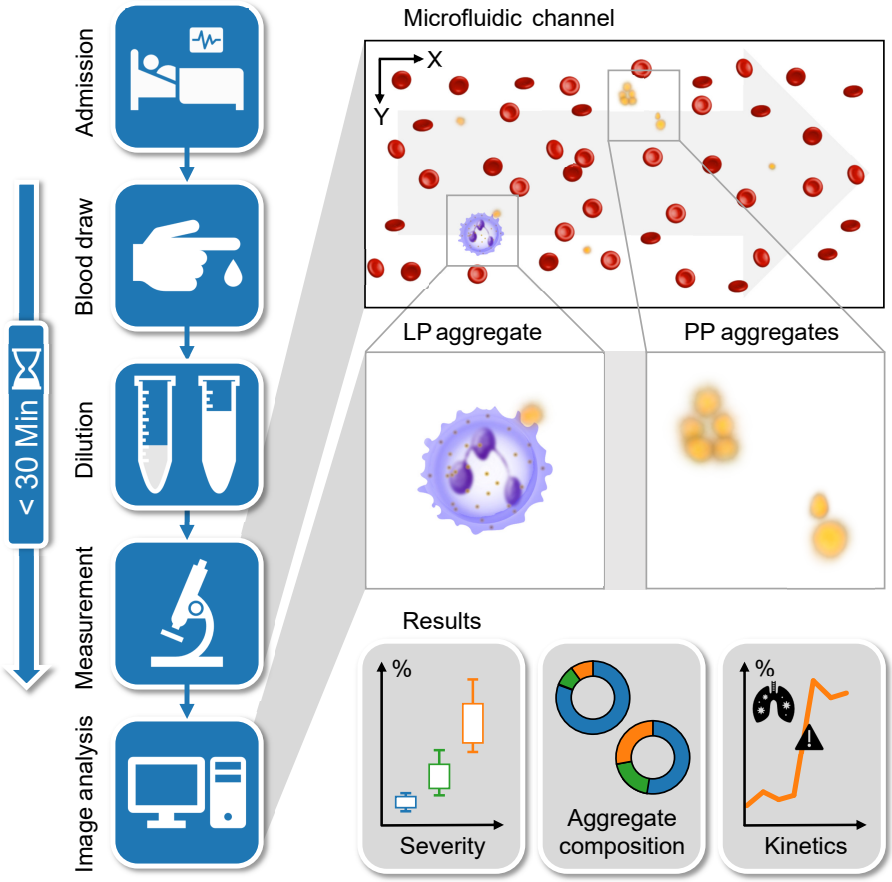

Figure 5.1: Schematic overview of the study workflow. After the admission of the patient to the hospital and as early as possible, blood was drawn, transported to the prototype, and diluted. The end of the measurement was still within the 30-minute time frame, with the measurement itself taking two minutes. Image analysis is divided into aggregate and single cell detection, classification analysis of single components, and a presentation of the results. Figure adapted from [207].

Blood from 36 patients between the ages of 32 to 83 was measured between November 2020 and 2021. The inclusion criteria involved a confirmed SARS-CoV-2 infection and a declaration of consent. For longitudinal measurements, every 2 to 5 days, fresh arterial or venous blood samples were collected using 2 mL Blood Gas-Monovettes® from Sarstedt. Here, 50 IU of calcium-balanced lithium heparin per millilitre of blood is used as the anticoagulant. Large-diameter cannulas were chosen to reduce shear rates during blood sampling. A catheter with a tube diameter of 1.6 mm was chosen for ICU patients with arterial access. For patients with moderate disease progression and healthy controls, venous blood was collected using 0.8 mm cannula and 2.3 mm tubing. Experiments were performed up to a maximum of 5 times, while the first measurement was planned early as possible from admission to the ICU. A total of about 50,000 cells were measured in one test. In a healthy patient, this means an analysis of $\approx 45,000$ erythrocytes, $\approx 5,000$ platelets, and ≈ 50 leukocytes. As described in chapter 4, aggregates tend to be unstable over time and, when exposed to environmental conditions change. For this reason, blood was analysed within 30 minutes after the blood draw and transported carefully to the prototype to minimise the mechanical stress on cells. The only sample preparation step was diluting the blood sample 1:100 in the measurement medium (Figure 5.1). Clinical, laboratory, and demographic data were additionally collected for further data analysis. The different patient cohorts were classified based on the WHO ordinal scale for clinical improvement for hospitalised patients with COVID-19 [189]. Patients with a score of 4 or 5 are classified as moderate COVID-19 cases and require no oxygen therapy or only oxygen by mask. Patients with a score between 6 and 10 are defined as severe COVID-19 cases and include individuals needing different invasive oxygen therapies and fatal cases. For the healthy cohort, a total of 15 individuals between the age of 29 to 67 donated blood. Similar demographic characteristics were used in the different cohorts to ensure comparability. A more detailed overview can be found in tables 5.1 and 5.2, where the high variance in co-infections of the patient cohort can also be observed. The study was approved by the ethics committee of the University Hospital Rechts der Isar (appendix A.1).

Table 5.1: Baseline characteristics of the healthy reference cohort. Data are presented as median with the corresponding range. The nominal data is given as n/N (%), where n is the exact number of participants, and N is the total number.

Baseline characteristics of healthy donors	**Mean (SD) or Median (Range)**	**n/N (%)**	**missing data**
Age (years)	50 (29-67)		0
Female		5/15 (33.3)	0
Male		10/15 (66.7)	0

Table 5.2: Baseline characteristics of the patient cohorts. If the Shapiro-Wilk normality test was passed, data are presented as mean with standard deviation. Alternatively, the median with the corresponding range is given.

Baseline characteristics of COVID-19 patients	**Mean (SD) or Median (Range)**	**n/N (%)**	**missing data**
Age (years)	65 (32-83)		0
Female		12/36 (33.3)	0
Male		24/36 (66.7)	0
COVID-19			
WHO clinical progression score	9 (4-10)		0
Variants - Wildtype - B.1.617.2 - B.1.1.7 - B.1.351		 10/36 (27.8) 21/36 (58.3) 4/36 (11.1) 1/36 (2.8)	0
Therapeutic details			
Oxygen (nasal cannula or mask)		33/36 (91.7)	0
Non-invasive ventilation		15/36 (41.7)	0
Mechanical ventilation		26/36 (72.2)	0
Length of mechanical ventilation (days)	18 (1-43)		1
Prone positioning		20/36 (55.6)	0
Extracorporeal CO2 elimination		10/36 (27.8)	0
ECMO therapy		4/36 (11.1)	0
Renal replacement therapy		10/36 (27.8)	0
COVID-19 directed therapy			
Remdesivir		5/36 (13.9)	0
Dexamethasone		32/36 (88.9)	0
Casirivimab/Imdevimab		9/36 (25.0)	0
Tocilizumab		2/36 (5.6)	0
Comorbidities			
Arterial hypertension		20/36 (55.6)	0
Diabetes mellitus		10/36 (27.8)	0
Coronary heart disease		6/36 (16.7)	0
Congestive heart failure		4/36 (11.1)	0
COPD		2/36 (5.6)	0
Malignant disease		5/36 (13.9)	0
Chronic kidney disease		6/36 (16.7)	0

5.2.2 Statistical Analysis

In this study, statistical analysis were performed using OriginPro (2021b), R (4.0.2), and IBM SPSS Statistics 25. The Shapiro-Wilk test was applied to test whether a normal distribution is given for the data set. Since the data obtained here is non-normal distributed, the significance was analysed using the non-parametric Kruskal-Wallis-ANOVA with a subsequent Dunn's test. Significant levels are indicated by asterisks, with $p < 0.05$ (*); $p < 0.01$ (**); $p < 0.001$ (***), and $p < 0.0001$ (****). Additionally, correlation values between aggregates and established biomarkers were calculated using Spearman's rank correlation. Under consideration that for most patients, there were multiple measurements, a within- and between-subject correlation was introduced. As the name suggests, within-subject correlation considers correlations from one patient across multiple measurement days. In contrast, the between-subject correlation investigates solely the correlation between multiple patients or cohorts. Both linear and exponential growth function fits were executed to describe certain patterns.

5.3 Correlation between Blood Cell Aggregates and COVID-19 Severity and Mortality

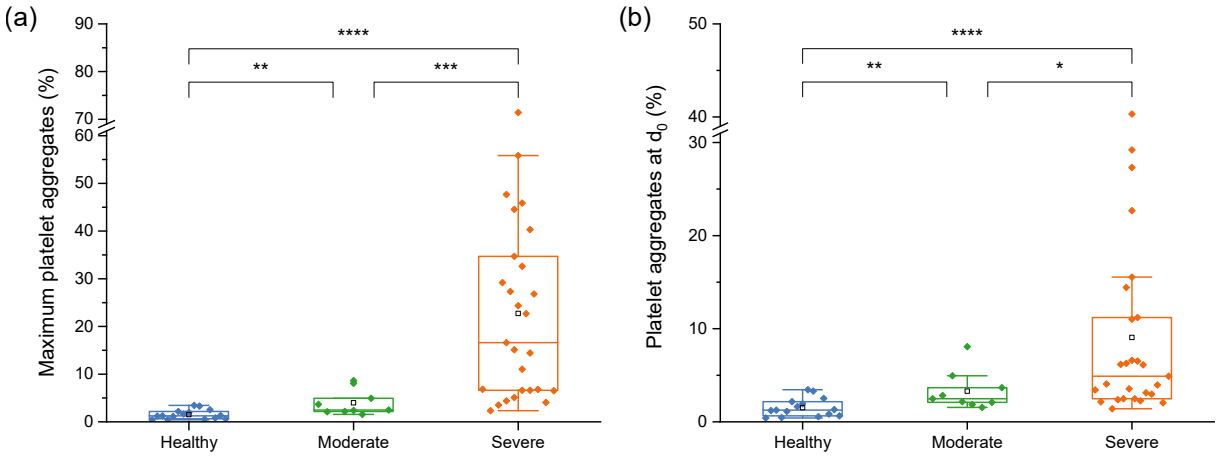

Figure 5.2: COVID-19 severity and platelet aggregate formation. Boxplots of the P-Aggregate distribution for healthy references ($n = 15$), moderate ($n = 9$), and severe ($n = 27$) COVID-19 patients. Shown are the percentages of P-Aggregates compared to the total amount of platelets for (a) the maximum day and (b) the first measurement. Each data point represents one patient. **(a)** Significant P-Aggregate differences between healthy vs. moderate ($p = 0.0046$), moderate vs. severe ($p = 0.0006$), and healthy vs. severe ($p < 0.0001$). **(b)** Comparing the values for the first measurement for healthy vs. severe ($p < 0.0001$), healthy vs. moderate ($p = 0.0095$), and in moderate COVID-19 patients vs. severe cases ($p = 0.0326$). Figure adapted from [207].

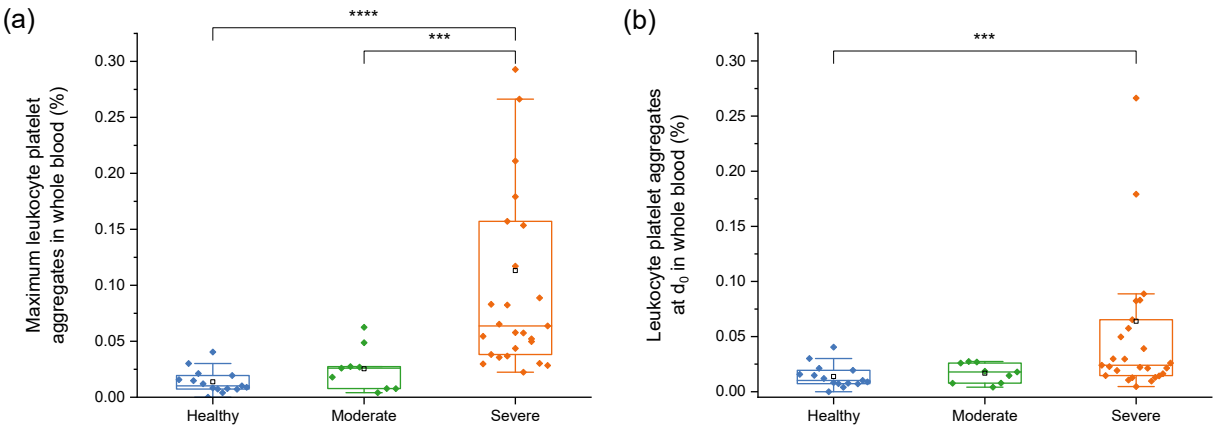

Figure 5.3: COVID-19 severity and leukocyte-platelet aggregate formation. Boxplots of the LP-Aggregate distribution for healthy references ($n = 15$), moderate ($n = 9$), and severe ($n = 27$) COVID-19 patients. Shown are the percentages of LP-Aggregates compared to the total amount of all blood cells for (a) the maximum day and (b) the first measurement. **(a)** Significant LP-Aggregate differences between healthy vs. severe ($p < 0.0001$) and moderate vs. severe ($p = 0.0004$). **(b)** Comparing the values for the first measurement for healthy vs. severe ($p = 0.0009$). All other comparisons show no significant differences. Figure adapted from [207].

The number of **P-Aggregate** levels of each patient between the different cohorts were compared. In a first step, the maximum value of the longitudinal study of each patient was considered. It could be observed that the P-Aggregate formation was significantly higher with increasing severity levels (Figure 5.2a). Here, the mean values of P-Aggregates ranged from 1.52 % for healthy, 4.00 % for moderate to 22.71 % for severe cases. The healthy range is comparable to previous experiments (Figure 4.6). To test whether this biomarker is suitable for predicting the severity of COVID-19, the values of the initial measurement were compared (Figure 5.2b). Similar to the previous results, the mean values of the cohorts rise depending on the severity with healthy, moderate, and severe cohort values of 1.52 %, 3.29 %, and 9.06 % respectively. A significant difference between all cohorts presented here could be observed with significant levels according to the previously described definition (chapter 5.2.2).

Similar trends could also be seen for the **LP-Aggregates** numbers (Figure 5.3). For the maximum measurement day, the highest values of LP-Aggregates could be observed for severe patients with a mean value of 0.1131 % followed by 0.0254 % for the moderate, and 0.0138 % for the healthy cohort. The number of LP-Aggregates describes the fraction of LP-Aggregates compared to the total number of blood cells. It is noteworthy that while the significance levels between severe and moderate as well as between severe and healthy were comparable to the P-Aggregates results, there was no significant observable difference between the healthy and moderate group. This effect was even more substantial on the first measurement day (Figure 5.3b). Here, the mean values of severe, moderate, and healthy were 0.0639 %, 0.0168 %, and 0.0138 %, respectively. Only one significant difference between the cohorts could be observed between severe and healthy, showing a

worse discrimination power than the results stated in Figure 5.2b.

In line with the results shown in Figure 5.2, was a significantly higher P-Aggregates occurrence in fatal COVID-19 cases with a mean value of 25.60 % compared to survivors with a mean value of 13.76 %. Still, both cohorts showed a higher frequency of P-Aggregate compared to the reference with a mean of 1.52 %.

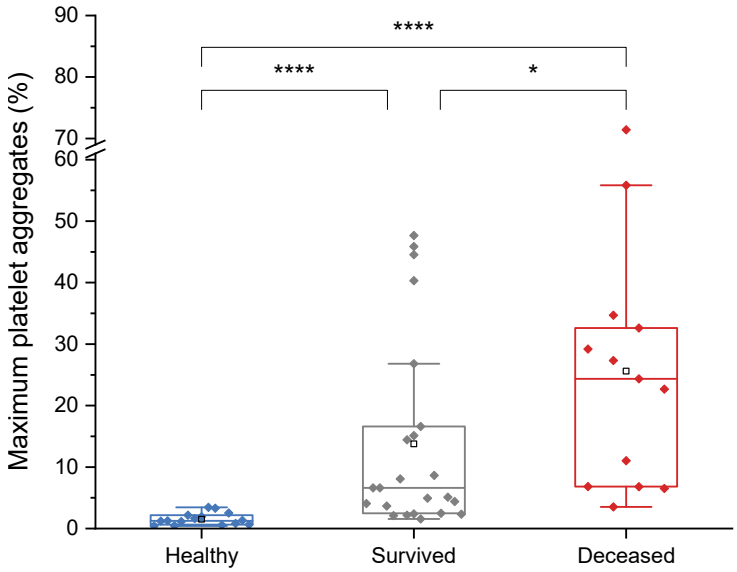

Figure 5.4: COVID-19 mortality and platelet aggregate formation. Boxplot of the maximum P-Aggregate distribution for healthy references ($n = 15$), survivors ($n = 23$), and patients with a fatal course ($n = 13$). Significant P-Aggregate differences between survived vs. deceased ($p = 0.0285$), healthy vs. survived ($p < 0.0001$), and healthy vs. deceased ($p < 0.0001$). Figure adapted from [207].

5.4 Platelet Aggregates and Established Clinical Biomarker

When comparing P-Aggregates in patients infected with the SARS-CoV-2 wild-type to patients infected with variants, which includes alpha (B.1.1.7, $n = 4$), beta (B.1.351, $n = 1$), and delta (B.1.617.2, $n = 21$), a significant difference could be seen. The mean values of the distributions were 11.80 % for SARS-CoV-2 variants and 3.57 % for wild-type SARS-CoV-2. Again, both cohorts were significantly higher than the healthy reference, with a mean value of 1.52 %.

Next, the P-Aggregates at day 0 are plotted against the viral load on the measurement day (Figure 5.5b). Patients with moderate and severe disease are shown in green and orange, respectively, while orange stars highlight outliers. Outliers are defined by a relatively low viral load compared to a highly severe disease course (e.g., fatal course). Moderate, severe,

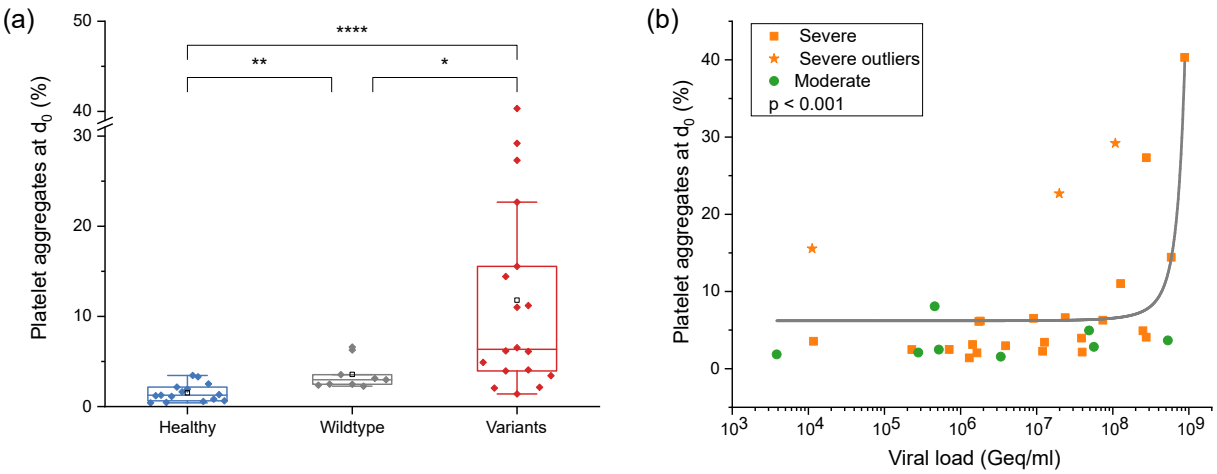

Figure 5.5: Connection between P-Aggregates at day 0 with SARS-CoV-2 variants and viral load. **(a)** Boxplots of the P-Aggregate distribution for healthy references ($n = 15$), patients infected by SARS-CoV-2 wild-type ($n = 10$), and variants ($n = 26$, B.1.1.7, B.1.617.2, with AY lineages, and B.1.351). Significant differences could be observed between wild-type vs. variants ($p = 0.0397$), wild-type vs. healthy ($p = 0.0021$), and variants vs. healthy ($p < 0.0001$). **(b)** Association between the viral load in the alveolar fluid and the P-Aggregates at day 0. Highlighted are severe outliers (orange stars), severe (orange squares), and moderate (green circles). Figure adapted from [207].

and severe outliers were equally distributed for the viral load, while P-Aggregates showed the previously described distribution power. Nevertheless, a significant correlation was found between the two biomarkers, although large differences were observed for outlier and moderate patients.

Further established biochemical parameters which are broadly used in diagnostics are D-Dimer and PCT. Increased D-Dimer levels have been associated with coagulopathy and suggested as a potential biomarker to predict mortality in COVID-19 [190]. A moderate but significant between-subject correlation could be seen when plotting the longitudinal P-Aggregates measurements against the corresponding D-Dimer levels. This indicated high D-Dimer levels in patients with high levels of P-Aggregates. However, it should be noted that the within-subject correlation was not significant ($r = 0.24$; $p = 0.0920$). Furthermore, a significant within-subject correlation was observed between P-Aggregates and Procalcitonin (PCT), which is a marker for hyperinflammation used to monitor bacterial infections. Even though the presented data did not indicate a positive between-subject correlation of P-Aggregates and PCT, this still suggests that dynamic changes may be monitored using serial measurements of P-Aggregates. Lastly, no correlation between P-Aggregates, and the inflammatory markers CRP and Interleukin-6 were seen.

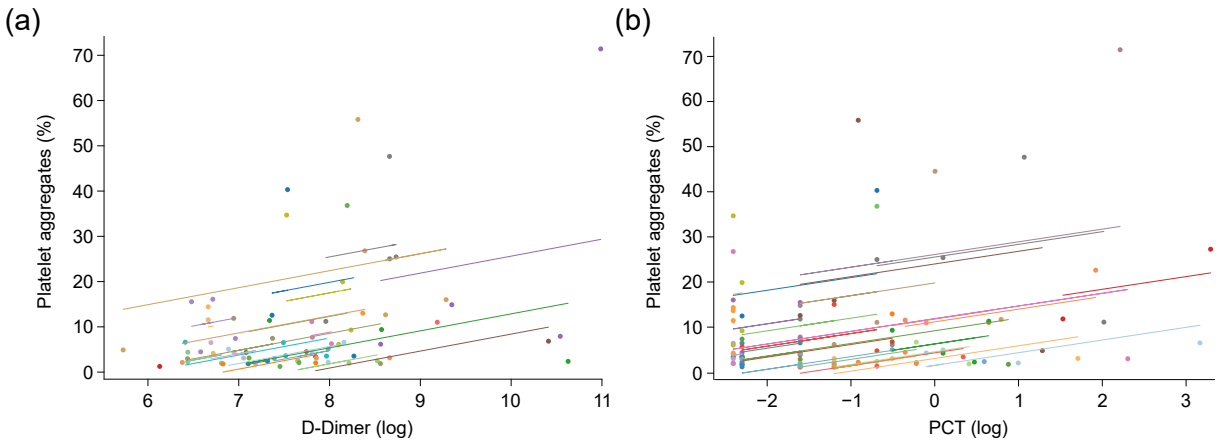

Figure 5.6: Connection between P-Aggregates with D-Dimer and PCT. (a) Correlation of P-Aggregates and the corresponding D-Dimer levels (in µg/L, logarithmical, $reference < 500\,\mu g/L$) with an between subject correlation of $r = 0.46$ and $p = 0.0131$. Each colour represents one patient. **(b)** Correlation of P-Aggregates and the corresponding PCT levels (in ng/mL, logarithmical, $reference \leq 0.1\,ng/mL$) with a within-subject correlation of $r = 0.26$ and $p = 0.0279$. Figure adapted from [207].

5.5 Differences in Aggregate Composition Dependent on COVID-19 Severity

The method presented here allows not only an analysis of aggregate numbers but also an insight into aggregate composition. First, this was used to compare the number of involved platelets per aggregate for different patients. Figure 5.7 shows a direct comparison of aggregate sizes up to ten platelets for exemplary donors. As in previous experiments (Figure 4.7b), P-Aggregates from healthy donors were mainly composed of two and three platelets. A higher amount of big aggregates ranging up to ten platelets could be seen for moderate and severe patients. In line with these examples was the statistical analysis of aggregate sizes in the different cohorts (Figure 5.8). For the healthy reference, 81.3 % of detected P-Aggregates consist of two platelets, compared to 73.2 % in moderate and 59.8 % in patients with a severe COVID-19 infections. Consequently, the amount of larger aggregates was in this cohort higher. The proportion of triplets was 14.6 %, 15.9 %, and 26.6 % for healthy, moderate, and severe, respectively. Especially noteworthy were differences in bigger clusters composed of four or more platelets. Here, only 4.1 % could be observed for healthy references compared to the 10.9 % for moderate and 13.6 % for severe. Exemplary images of two-, three-, and four-platelet aggregates were displayed in the centres of the chart.

The size distribution of the involved platelets in an aggregate was analysed further. Again, the three different cohorts were compared, whereby a distinction was made between individual platelets and platelets in an aggregate for each of the groups. In each histogram shown in Figure 5.9, the number of platelets is plotted against their corresponding diame-

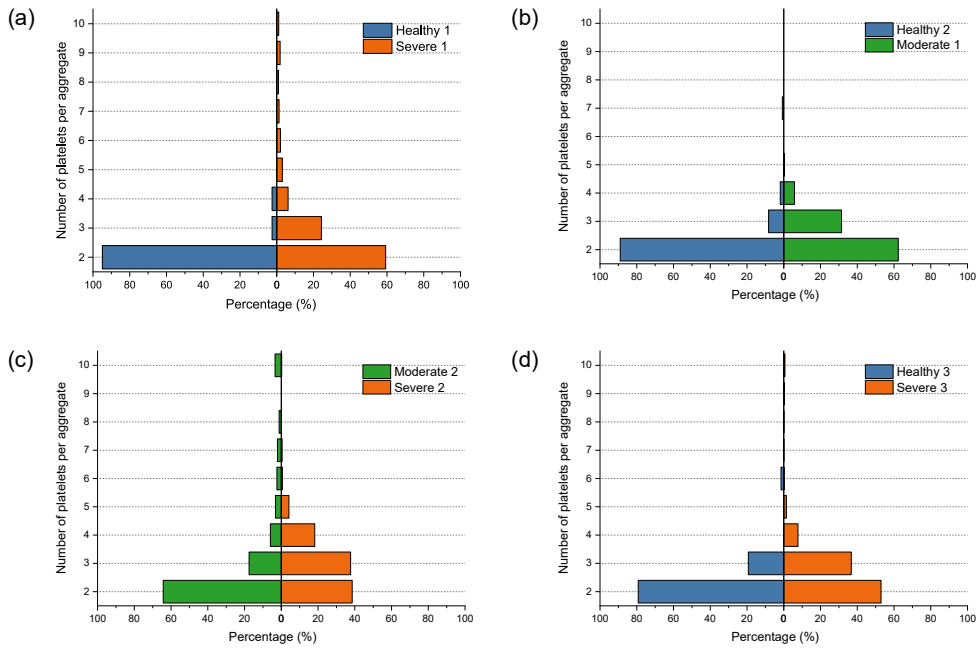

Figure 5.7: Exemplary size distribution of P-Aggregates in different donors. Healthy references are displayed in blue **(a, b, d)**, while moderate **(b, c)** and severe **(a,c, d)** COVID-19 cases are highlighted in green and orange, respectively. Figure adapted from [207].

ter. The mean diameter is highlighted as a red line. When comparing the single platelets of the different cohorts, it could be seen that the mean diameter increased slightly with the increasing severity. The diameter distribution of the main population was around 2 µm and stayed the same over all groups. The difference in mean diameter arose due to an appearance of a second platelet population at 5 µm. The effect was even more dominant, looking at platelets in aggregates. Here, a small fraction of this population was already visible for healthy donors. This pattern was even more evident for moderate and severe COVID-19 progressions. Finally, it resulted in a shift of the mean platelet diameter over the cohorts from 1.9 µm, over 2.2 µm up to 3.0 µm.

In addition to the (1) number and (2) size of aggregates, and the (3) size distribution of individual platelets, (4) phase-related properties of single platelets were analysed. For this, the refractive index dependent size of the **optical height** was considered. The mean value over all pixels within a platelet was taken. Again, a distinction was made between individual platelets and platelets in an aggregate. In Figure 5.10a-c, the optical height mean values between single and aggregated platelets were compared for the three different cohorts. To ensure comparability with previous analyses, the day with the highest number of P-Aggregates was used. In all three cohorts, the aggregated platelets had higher optical height mean values than the individual platelets, but only for the healthy and severe population, a significance could be observed. In healthy references, the mean value of the single cell population is 0.0671 rad, while the mean of the aggregated population is 0.0799 rad. For the moderate and severe cohort it was 0.0712 rad vs. 0.0800 rad and 0.0763 rad vs. 0.1052 rad. Furthermore, a comparison between the cohorts was made for

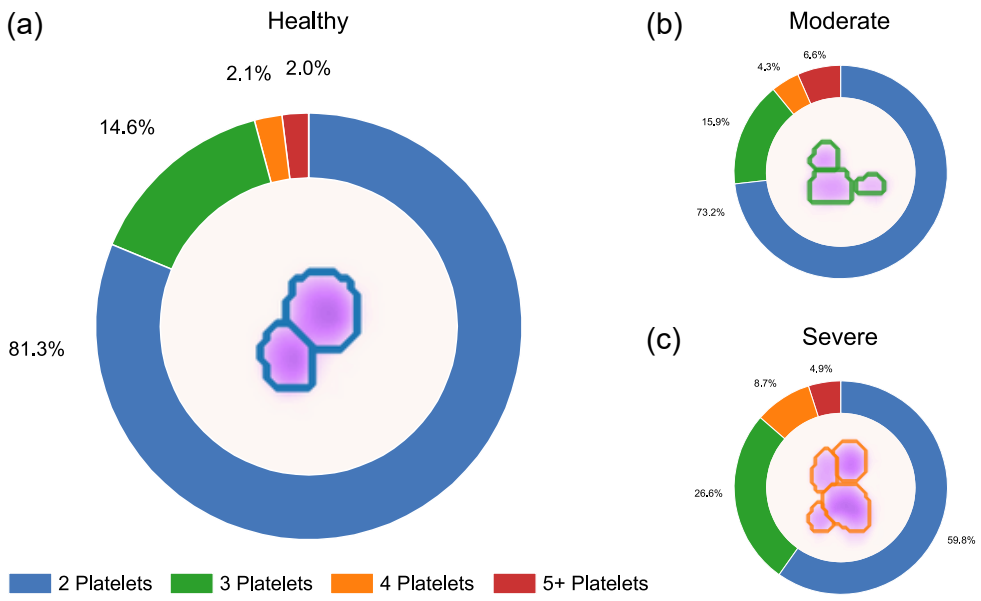

Figure 5.8: P-Aggregate size distribution over the different cohorts. Mean values of the aggregate sizes on the maximum measurement day for healthy **(a)**, moderate **(b)**, and severe **(c)**. Images in the centres show exemplary aggregates containing two, three, and four platelets as well as their respective segmentation (coloured lines). Figure adapted from [207].

individual and aggregated platelets (Figure 5.10d-e). For single platelets, a significant difference could be observed between healthy and moderate as well as healthy and severe. For aggregated platelets, a significant distinction was seen between severe patients and the other two cohorts.

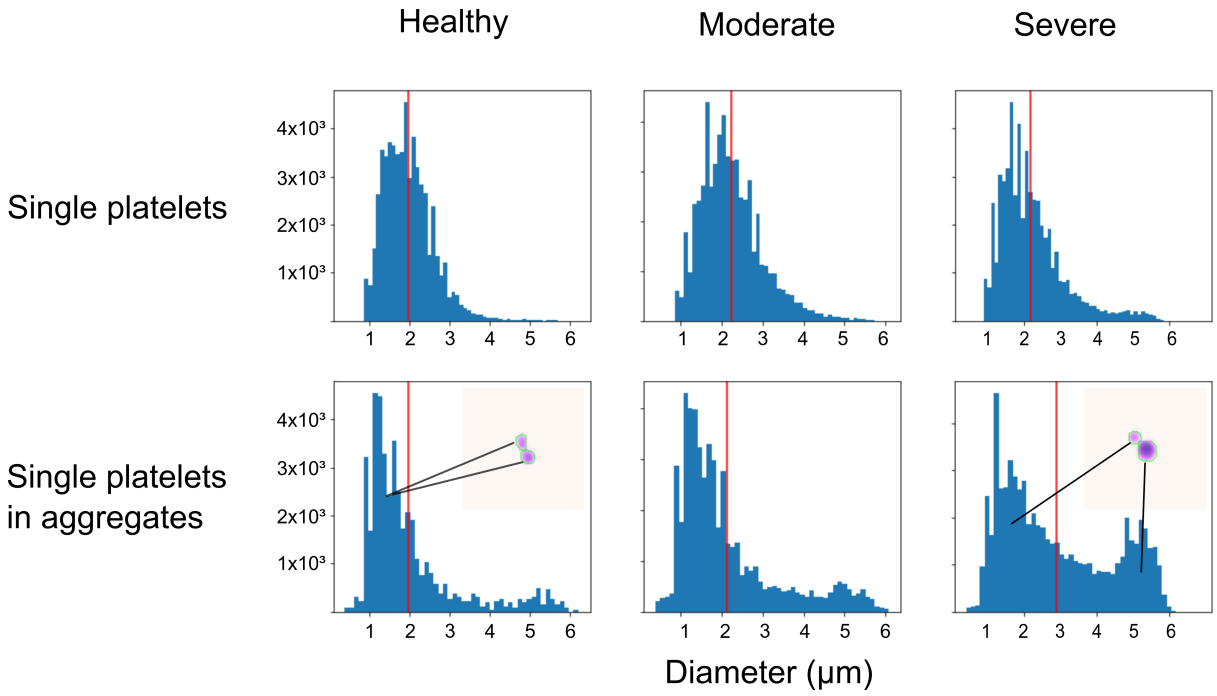

Figure 5.9: Diameter of platelets as single cells and in aggregates. Histograms of the diameter distribution of single platelets (top row) and platelets in aggregates (bottom row) grouped into healthy (left panel), moderate (middle panel), and severe (right panel). The mean of all cells is highlighted in red. Two exemplary images show one aggregate only containing platelets of the same size and an aggregate that contains both platelet types. Figure adapted from [207].

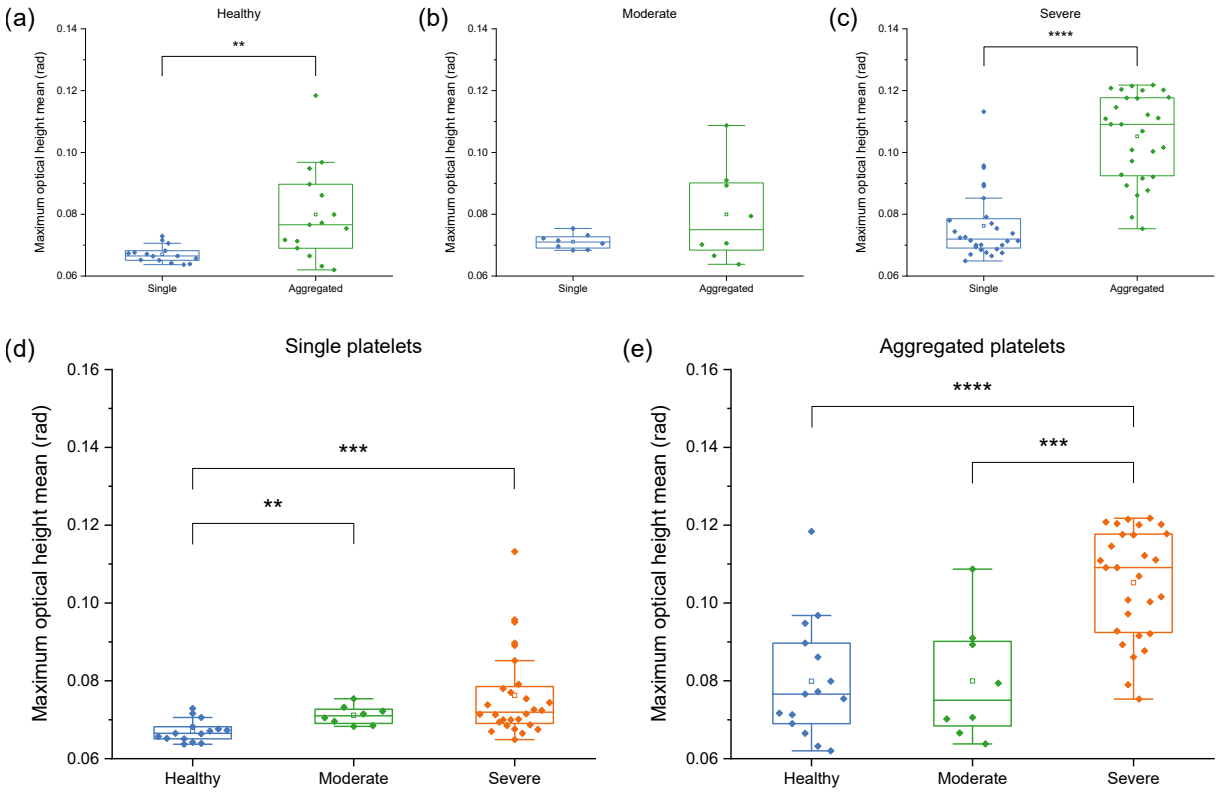

Figure 5.10: Optical height mean for single platelets and in aggregates. (a-c) Comparison between the optical height mean values of individual platelets and platelets in aggregates. Data were taken from the measurement with the maximum number of aggregates. Significant value differences could be seen for the (a) healthy ($p = 0.0042$) and (c) severe cohorts ($p < 0.0001$) but not for the (b) moderate group ($p = 0.4500$). **(d)** When comparing the single platelets of all cohorts, a significant difference can be seen for healthy vs. moderate ($p = 0.0037$) and healthy vs. severe ($p = 0.0002$). **(e)** For aggregated platelets, a significant difference was observable between healthy vs. severe ($p < 0.0001$) and moderate vs. severe ($p = 0.0009$).

5.6 Longitudinal Measurement of Aggregates in the Acute Phase of COVID-19

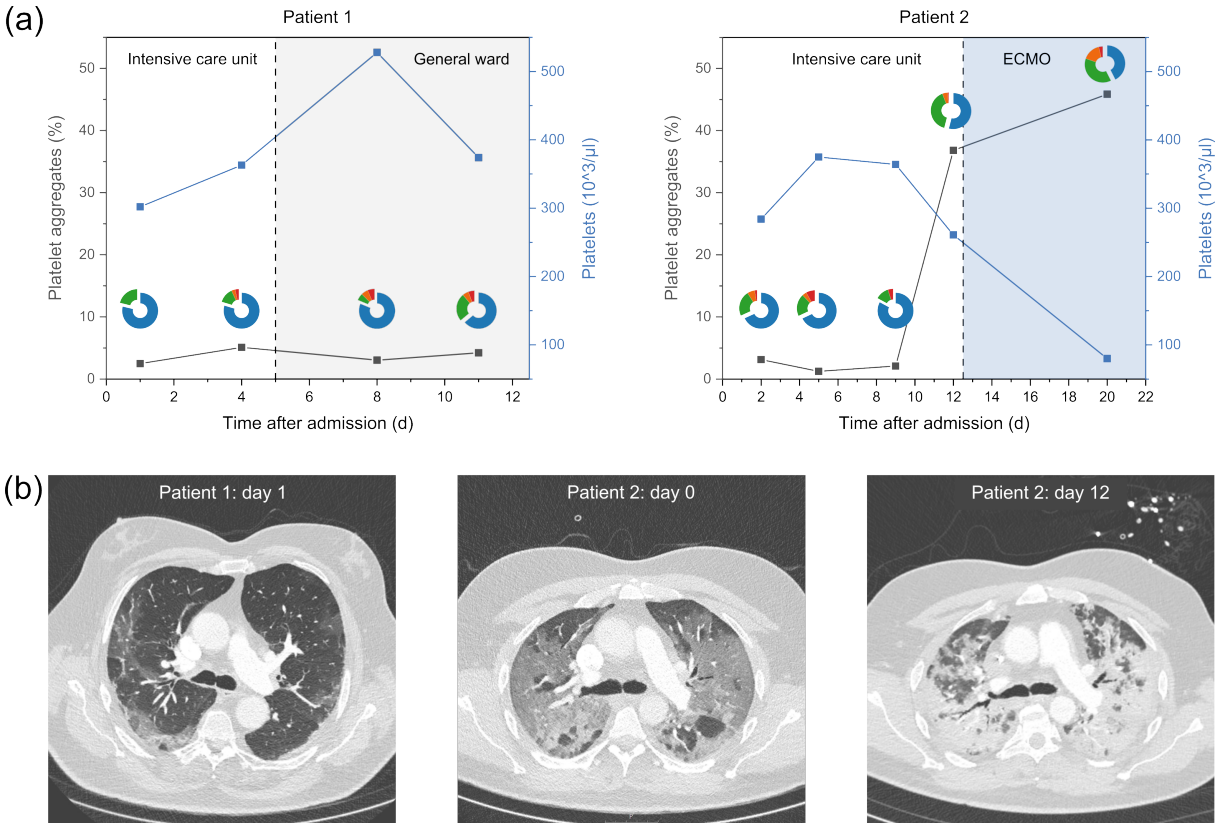

Figure 5.11: Longitudinal assessment of platelet concentration, P-Aggregate numbers, and composition in two exemplary patients. **(a)** P-Aggregate share (blue squares) and composition (pie chart) plotted against the time after admission. Colours in the pie chart indicate the fraction of aggregates with two (blue), three (green), four (orange), and more than four (red) platelets. Additionally, the platelet concentration (black squares) is measured with a commercial haematology analyser. **(b)** Representative computer tomography (CT) scans from patient 1 on the day after admission to the ICU (left, day 1), from patient 2 on the day of admission to the ICU (middle, day 0), and the day of the initiation of extracorporeal membrane oxygenation (ECMO) therapy (right, day 12). Figure adapted from [207].

Up until now, no reliable biomarker for clinical deterioration has been established for hospitalised COVID-19 patients. Therefore, platelet aggregates were measured in a longitudinal study to assess whether aggregate formation changes during the acute phase of COVID-19 disease. Results of platelet aggregate number and composition were then plotted against the corresponding platelet concentration obtained by a commercial haematology analyser. These findings and representative computed tomography (CT) scans were

shown for two severe patients in Figure 5.11. Patient 1 was admitted to the ICU on day 0 because of an increased oxygen demand. The patient was stabilised and transferred to the regular ward on day 5, with no need for invasive or non-invasive ventilation. This is also reflected by the aggregate measurements where the number of P-Aggregates remained under 5 % throughout the measurement period of 11 days. Similar patterns could be observed for the aggregate size distribution, whereby a marginal increase was seen for day 11. Also, the platelet concentration remained in the reference range ($150,000 - 450{,}000\,\mu L^{-1}$) with only one exception on day 8 ($528{,}000\,\mu L^{-1}$). The corresponding CT scan on day 1 showed typical, moderate ground glass opacities. In contrast, patient 2 required intubation and mechanical ventilation nine days after ICU admission. Additionally, venovenous extracorporeal membrane oxygenation (ECMO) treatment was needed on day 12 due to the rapid deterioration of respiratory function. While the total platelet count was within the reference range and no increase in P-Aggregates was observed during the first nine days, there was a significant increase in P-Aggregates with a large proportion of aggregates containing three or more platelets on day 12, just before the start of the ECMO therapy. Due to the clinical deterioration on that day, another CT scan was performed, showing dramatic progression compared to the first scan on day 0. Following the initiation of the ECMO therapy, the total platelet count decreased to $261{,}000\,\mu L^{-1}$. This was particularly evident on day 20 when the platelet concentration fell to $80{,}000\,\mu L^{-1}$, which is below the reference range. Interestingly and in line with the patient's further clinical deterioration, the number of P-Aggregates, and the size of the aggregates increased significantly within the same time frame. Due to the protocol limitations, no further analysis exceeded the 20 days. However, the patient gradually recovered, was weaned and subsequently removed from ECMO and ventilation, and was eventually discharged.

Other biomarkers such as D-Dimer, PCT, CRP, IL-6, and the leukocyte count for both patients are shown in Table 5.3. In addition, also P-Aggregates number, P-Aggregates with more than two platelets, and optical height mean values of single platelets were added. Values outside of the respective reference range of healthy individuals were marked in red. Consistent with previous results, most biomarkers in patient 1 showed no abnormality. Only the D-dimer levels within the first four days and the white blood cell count from day 4 onwards deviated from the pattern. Patient 2 had a much more variable pattern. All the biomarkers of the phase imaging flow cytometer follow the course of the P-Aggregate numbers. D-Dimer and CRP show an elevated value over the entire progression, as does PCT, with the exception of the first measurement. However, it is important to note that the D-Dimer levels are strongly elevated at the last two measurement points and thus show a similar behaviour to the platelet aggregation. On the other hand, IL-6, platelet count, and WBC count do not follow a clear pattern, which is related to the patient's state of health.

Table 5.3: Biomarkers throughout the longitudinal measurement of patients 1 and 2. Values outside of the respective reference ranges of healthy individuals are highlighted in red.

Patient 1	Day 1	Day 4	Day 8	Day 11	
# P-Aggregates (%)	2.48	5.11	3.3	4.21	
P-Aggregates > 2 platelets (%)	21.21	17.54	13.33	32.35	
OHM single platelets (rad)	0.077	0.077	0.075	0.073	
OHM aggregated platelets (rad)	0.101	0.101	0.082	0.100	
D-Dimer (µg/L)	1,217	1,506	nan	nan	
PCT (ng/mL)	0.10	0.10	0.10	nan	
CRP (mg/dL)	4.10	0.80	0.30	nan	
IL-6 (pg/mL)	6.90	8.10	1.60	nan	
# Platelets ($10^3\,\mu L^{-1}$)	302	363	528	374	
# Leukocytes ($10^3\,\mu L^{-1}$)	7.63	13.84	19.75	20.85	
Patient 2	Day 2	Day 5	Day 9	Day 12	Day 20
# P-Aggregates (%)	3.12	1.25	2.10	36.82	45.86
P-Aggregates > 2 platelets (%)	32.35	32.00	17.07	46,00	57,47
OHM single platelets (rad)	0.067	0.072	0.074	0.096	0.085
OHM aggregated platelets (rad)	0.095	0.076	0.081	0.120	0.114
D-Dimer (µg/L)	1,228	1,726	2,128	3,620	6,794
PCT (ng/mL)	0.10	0.30	0.20	0.50	0.20
CRP (mg/dL)	8.40	28.50	9.30	25.40	10.80
IL-6 (pg/mL)	22.50	128.00	67.00	152.00	7.40
# Platelets ($10^3\,\mu L^{-1}$)	284	375	364	261	80
# Leukocytes ($10^3\,\mu L^{-1}$)	17.12	15.57	16.37	18.64	6.62

5.7 Possible Confounding Variables on Measurement Results

There are many sources of confounding variables that can affect the results of a study. Potential sources of confounding include study design, patient medication, and baseline characteristics of the cohort. In this chapter, the corresponding study design and properties of the patient cohort are evaluated regarding their influence on aggregate formation.

Delay in the analysis of unfixed blood samples due to preanalytical steps, incubation, or other **storage times** is known to activate platelets within two hours [191], which subsequently can lead to artificial aggregation. To investigate these changes, we obtained blood samples from nine severe COVID-19 patients and three healthy reference subjects and assessed the percentage of P-Aggregates in each sample at 0, 60, and 120 minutes. Similar to previous results, a significant difference could be seen between both cohorts directly after the blood draw. With increasing storage times, both populations' mean number of aggregates and the corresponding standard deviation rose. For the healthy reference, within 120 minutes, the aggregates got from 1.69 % up to 16.01 % while the

severe group went from 8.91 % to 22.81 %. This shows that it may be challenging to differentiate between the two clusters at higher storage times.

Many hospitalised COVID-19 patients are treated with an antithrombotic therapy. Dependent on prevalent thromboembolism, underlying conditions, individual risk factors, and local recommendations, the dosage will vary depending on the anticoagulant type and the amount. In the patient cohorts, including moderate and severe cases, 32 of 36 received unfractionated or low molecular weight heparin at least once during admission. To rule out any effect of **intravenous heparin** on aggregate stability, we assessed the anticoagulant treatment administered at the time of blood collection. Figure 5.12b shows the comparison between P-Aggregates and the corresponding administered heparin dosage on the day of sample collection. No significant influence of administered heparin on the P-Aggregates could be observed. In addition, from the first day in the ICU, eight patients were treated with **acetylsalicylic acid**. To compare whether this influences the P-Aggregate number, P-Aggregates were measured at d_0 but after the initialisation of the treatment. As shown in Figure 5.12c, acetylsalicylic acid treatment had no significant influence on the amount of P-Aggregates. Additionally, some patients were **intubated** while staying in the normal ward or ICU. To see whether this is a confounding variable on the measurement results, the number of P-Aggregates were plotted against the corresponding intubation status on the measurement day. Comparing the resulting two populations for all patients, measurements showed no significant difference between patients intubated during their stay and those not intubated.

After it could be shown that the type of treatment was not significantly relevant for the measured number of aggregates, in a final step, prominent patient characteristics were examined. First, the influence of a **patient's age** was analysed. In the patient's cohort, blood samples of subjects from 32 up to 83 years were measured. Despite the big age differences, no correlation between patients' age and the amount of P-Aggregates at d_0 could be seen. A similar picture was observable when looking at the patient's **Body-Mass-Index**. Here, the values ranged between 22.53 and 53.13. When plotting the Body-Mass-Index of each patient against the corresponding P-Aggregate measurement at d_0, no correlation is observable.

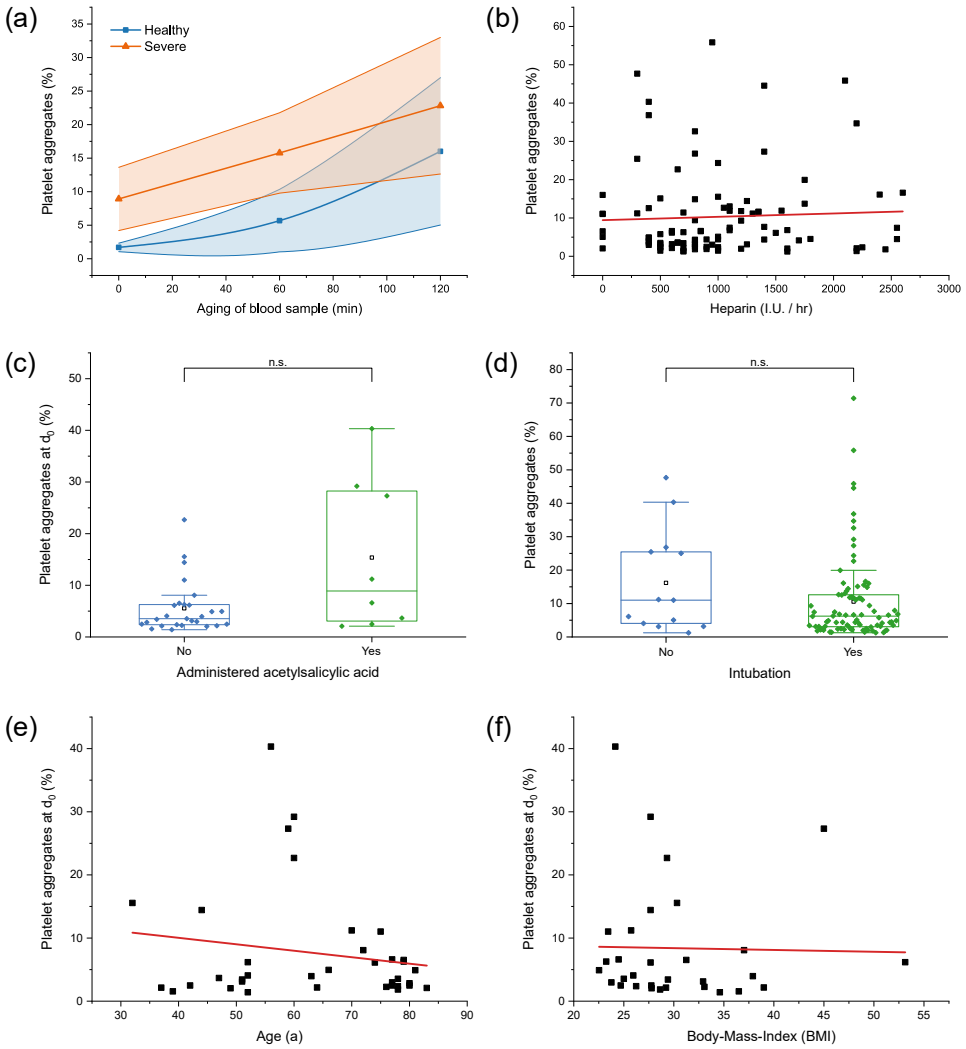

Figure 5.12: Possible confounders of P-Aggregates in the COVID-19 study. **(a)** Ageing of the blood sample is analysed by measuring P-Aggregates of healthy (blue) and severe COVID-19 patients (orange) at 0, 60, and 120 minutes. Squares and triangles show the mean values, while the coloured area indicates the standard deviation. For 0 and 60 minutes, a significant difference of $p = 0.0074$ and $p = 0.0185$ can be observed. **(b)** Correlation between P-Aggregates and the intravenous unfractionated heparin dosage administered at the time of sample collection shows no significance ($n = 98$, $r = 0.05$, $p = 0.6268$). **(c)** Comparison between P-Aggregates at day 0 and if they are treated with acetylsalicylic acid shows no significant correlation ($p = 0.0771$). **(d)** P-Aggregate distribution for severe patients both intubated and not intubated showing no significant difference ($p = 0.2456$). **(e)** Correlation between P-Aggregates and the patients age shows no significance ($r = -0.05$, $p = 0.7523$). **(f)** Correlation between P-Aggregates and the patients Body-Mass-Index shows no significance ($r = -0.20$, $p = 0.2815$). Figure adapted from [207].

5.8 Discussion

An unprecedented effort has been made to understand the mechanism of CAC. CAC is considered to be a major life-threatening complication and a critical pathogenic factor in COVID-19 [103]. But still, many pathophysiological mechanisms and therapeutic approaches remain elusive. Clinical parameters and biomarkers are essential for risk stratification, therapy, and prognosis. Although a wide range of biomarkers has been used for clinical practice before the emergence of COVID-19, only three have recently been recommended in a consensus statement for routine use. These are the platelet count, D-Dimer levels, and CRP [107]. Other biomarkers developed based on mechanisms in CAC mostly lack perspective and are therefore not yet recommended for clinical practice. Even the addition of modern data analysis tools, such as machine learning approaches, did not solve the problem. Furthermore, some of those biomarkers were only measured once during the disease, limiting the analysis of dynamic changes. This was, in many cases, due to the complexity of the assays required to asses the novel parameters, which also hampers large-scale validation studies [107]. Preferable for clinical practice are readily accessible devices which are preferable POC diagnostic tools allowing the measurement of large cohorts without excessive sample preparation.

This chapter discusses the label-free measurement of blood cell aggregates as one future solution. The methodology allowed a quantitative analysis of blood cell aggregates at four levels. The study of **(1)** aggregate numbers, **(2)** the analysis of the aggregate composition, **(3)** the evaluation of individual cell diameters, and **(4)** the investigation of quantitative phase values of a single object. In addition to the informational depth of this approach through a high contrast, the measured phenomena have a fast response time. In the previous chapter, a response could be seen 3 minutes after the activation of a blood sample. To validate this novel approach, an exemplary study, including 36 COVID-19 patients and 15 healthy references, was conducted. As in previous chapters, a combination of microfluidics, QPI, and suitable image analysis was used to detect LP-Aggregates and P-Aggregates. To minimise unintentional influencing factors by the measurement system, blood vessel flow conditions were mimicked by reducing the shear rates acting on the cells [192] (see chapter 3.3). Still, high-throughput measurement of $500 - 2,000\,cells/s$ was achieved by parallel analysis of more than one cell per image. By limiting the time between sample collection and measurement to less than 30 minutes, the sample quality was secured, and unwanted ageing effects were avoided.

It could be shown that **P-Aggregate numbers** significantly correlate with COVID-19 severity and mortality. These results align with recently published work [97, 103, 111, 117, 118]. For example, Nishikawa et al. also used an imaging flow cytometry approach to show the correlation between P-Aggregates and disease severity. Additionally, the link between this novel biomarker and COVID-19 mortality was observed. However, it should be noted that blood samples in their study were undertaken extensive preparation steps before analysis, which was performed within four hours of sample collection. On the contrary, the presented work here suggests that an intermediate measurement after blood collection is needed to enhance the discrimination power between different cohorts (Figure 5.12a). While ageing characteristics of healthy blood are characterised for four

different anticoagulants (Figure 4.6) for infected patients, only Blood Gas Monovettes® from Sarstedt were examined. On the contrary, Nishikawa et al. used citrated blood samples, which are physiologically different. Similar as for the P-Aggregate numbers, we were able to see differences between patient severity levels in the LP-Aggregate count. However, the differences between the cohorts were not as significant as for P-Aggregates. This fact may be explained by the low statistical number of captured leukocytes during a measurement. Since the study design was planned to reduce sample preparation by avoiding the depletion of erythrocytes, the biggest population of measured cells are erythrocytes, followed by platelets. Only a small fraction of cells were actual leukocytes. This resulted in around 50 detected leukocytes per capture. This data indicates that **SARS-CoV-2 variants** showed a significantly higher number of P-Aggregates than patients infected by the wild-type. Here, the variant cohort consisted mainly of 21 Delta (B.1.617.2) and four alpha (B.1.1.7) infections. Both variants are known to be more virulent compared to the wild-type [193, 194]. It could be argued that the increase of P-Aggregates mirrors primarily disease severity and cannot be attributed to specific variants. Furthermore, a positive correlation between viral load in the alveolar fluid and the P-Aggregates in blood could be shown for the cohort. Across many viral infections like HIV, Ebola, and influenza, the extent of the viral load has been a predictor of disease severity. However, for SARS-CoV-2, its role in pathogenesis and ability to predict clinical outcomes remains unresolved [195]. This is also reflected in this study cohort, where the moderate cohort was equally distributed over the range of the detected viral load. Additionally to the viral load, also other **clinical routine biomarkers** were correlated to P-Aggregates. One example of such a routine marker is the D-Dimers, which result from fibrin degradation in thrombi. As thrombus formation is a highly dynamic process, this marker can be used for coagulation and fibrinolysis and has been strongly associated with the severity of COVID-19 [106]. However, an optimal cut-off value for therapeutic or diagnostic decisions remains controversial [196]. A positive between-subject correlation for D-Dimer and P-Aggregates could be observed, aligning with both parameters' prognostic power. In contrast, longitudinal measurements of other biomarkers did not correlate. This is also in line with previous reports [118]. The prognostic value of PCT in COVID-19 is controversial and mainly associated with a bacterial co-infection and not with the primary viral infection [197, 198]. Therefore, it is only consequential that several assessments of PCT levels are recommended to identify secondary bacterial infections, which often require antibiotic treatment [199]. Interestingly, a significant within-subject correlation between P-Aggregates, and corresponding PCT levels ($r = 0.26$; $p = 0.028$) was found, suggesting a possible association of P-Aggregates with superinfections, which may be interesting to explore in future projects. There is no direct correlation between P-Aggregates and inflammatory biomarkers such as CRP and Interleukin-6, showing a difference in the informational value of the aggregates compared to values that primarily indicate inflammation.

For the evaluation of **P-Aggregates composition**, it could be observed that in healthy donors, most aggregates were composed of two platelets ($> 80\,\%$). The possibility of that occurrence cannot be solely explained by an overlap of the cells, as the percentage of platelets in whole blood compared to erythrocytes is low. Additionally, as described in

chapter 3.3, the dilution was adjusted to reduce spatial coincidences. P-Aggregates may thus appear physiologically in the body or as a side product of the blood draw. Patients infected with COVID-19 tended to have higher numbers of larger aggregates, consisting of up to ten platelets. These findings align with published results from Rampotas et al. [97], who observed large platelet aggregates of up to 30 platelets in blood films from COVID-19 patients.

In addition, Rampotas et al. found macrothrombocytes, a larger platelet subpopulation, indicating increased platelet activity in COVID-19 patients. These macrothrombocytes could also explain the formation of a second **platelet population with a higher diameter** around 5 µm that was especially dominant in severe COVID-19 cases and aggregates (Figure 5.9). In the findings presented here, severity influenced the number of large platelets. Additionally, it could also be seen that they occur more often in aggregates than in single cells. Guthikonda et al. and other groups showed that reticulated platelets, which are young platelets, tended to have a higher diameter and are more active than non-reticulated platelets [200, 201]. In another publication, this group also showed a decreased antiplatelet effect on reticulated platelets [202], which may explain the observed difference in activity.

To analyse **quantitative phase values**, the optical height mean was calculated for each cell. A distinction was made between individual platelets and platelets in an aggregate. In all cohorts, the aggregated group showed higher optical height mean values than the individual cells. In addition, the optical height mean was higher in severe patients compared to healthy individuals. This was particularly dominant for aggregated platelets. Activated platelets tend to form aggregates [203], so a higher proportion of activated platelets can be expected compared to the single cell population. Macey et al. showed that a higher activation state of platelets correlates with a reduction in the refractive index. At first sight, this seems to contradict the results presented in this study. This is because the optical height mean correlates directly with the refractive index. However, it should be noted that Macey et al. used blood from healthy donors in combination with an activation assay. They compared the activation state of platelets within the same blood sample. In contrast, we analysed different patients with high biological variability. The presence of macrothrombocytes with a denser intracellular structure can explain why platelets from patients in the severe group tend to have a higher optical height mean. In further steps, the platelet population should be divided into two populations, the regular platelets and the macrothrombocytes. The mean optical height can then be calculated independently for both groups.

In two **exemplary patient cases**, a correlation between the longitudinal assessment of P-Aggregates, and the clinical course could be shown. Both patients were treated in the ICU at the beginning but showed two completely different courses. While P-Aggregate numbers and composition did not greatly vary in patient 1, a reversed trend could be seen for patient 2. Simultaneously with the clinical deterioration of patient 2 on day 12, P-Aggregates increased dramatically and were even higher on day 20. This trend was also true for the number of bigger aggregates and the optical height mean values of platelets. While the increased consumption of platelets in the extracorporeal blood circuit prob-

ably contributes to the observed decrease in the total platelet count after initiation of ECMO therapy, the reduction of platelets on day 12 is probably caused by the formation of P-Aggregates, as the blood sample was taken before initiation of ECMO therapy. The decrease in platelets on day 12 is comparable to the values on day 2 when there was no rapid deterioration of the patient's condition. These findings suggest that P-Aggregates could be used to differentiate the causes of platelet consumption. **Other biomarkers** showed highly varying patterns for these two patients. As expected, markers that have been shown not to correlate with the severity of COVID-19 presented inconsistent results. The leukocyte count was almost consistently elevated in both patients, but at the peak of patient's 2 disease, it was within the reference range ($6.62 \times 10^3\,\mu L^{-1}$). Similar could be observed for IL-6 on the last measurement day. PCT levels, on the other hand, were significantly elevated in the acute phase and followed the patient's condition. However, this trend only worked qualitatively, not when analysing the exact trend of the values. Discrepancies were also observed with established COVID-19 markers. CRP was elevated throughout the course of patient 2 and for the first measurement point of patient 1 but didn't allow a quantitative analysis. For example, the CRP value for patient 2 was higher on day 4 (28.50 mg/dL) than on day 12 (25.40 mg/dL) when the actual complication occurred. By day 20, it had dropped to 10.80 mg/dL, while there was still no improvement in the patient's condition. Lastly, D-Dimer seemed to be a highly sensitive marker for COVID-19, which led to constant high values outside of the reference range for both patients. Again, it should be mentioned that there is no uniformly defined threshold for this marker. Nevertheless, the quantitative analysis of the values allowed for a differentiation of the severity. Patient 1 always showed values between $1,000 - 2{,}500\,\mu g/L$, which is also true for the first 9 days of patient 2. After the deterioration of the patient's condition, values increase to 3,620 on day 12 and 6,794 on day 20. In this limited case study, it is the only established biomarker that corresponds to the courses of the disease. However, it should be emphasised that these are only two examples, and therefore no general conclusions can be drawn.

Several possible **confounders** were evaluated to rule out that P-Aggregates are just a by-product of patients' other health conditions or treatment. One example is the age of patients. Various publications have shown that age has a significant impact on the severity of disease progression [119, 204]. Although P-Aggregates also correlates significantly with the severity of COVID-19 infection, there is no direct relationship between P-Aggregates and the age of patients. Therefore, it cannot be assumed that older people necessarily have a higher number of aggregates or that aggregates only occur because of the patient's age. There was also no significant correlation between any of the other observed variables like administered anticoagulant, intubation, or patient Body-Mass-Index. This underlines the hypothesis that the here observed elevated P-Aggregate count is caused by the severity of the COVID-19 infection.

6 Summary

6.1 Conclusion

Research and development of haematology analysers to study clinical biomarkers is an ongoing process. Both the analysis of established markers with higher accuracy and the testing of new markers can contribute to the improvement of personalised medicine. Many steps must be taken before a new measurement approach reaches the maturity level for such a medical analyser. In this thesis, a DHM was combined with a microfluidic system and a suitable image analysis to meet the requirements in haematological diagnostics. The three main objectives encompassed the *process from a laboratory prototype towards a medical technology device*, the *investigation of blood cell aggregates as a potential new biomarker in clinical diagnostics*, and the *application of this biomarker in a clinical COVID-19 study.*

The *steps towards a medical technology device* were taken in many ways. Advances in fluidics made it possible to precisely manipulate cells without altering their functions. This was achieved by understanding the factors that affected them. By adding reference particles to the sample, it was possible to accurately measure the concentration of cells. Such microspheres could also enhance the discriminatory power of cell differentiation through targeted cell labeling. Three possible calibrator systems with different degrees of similarity to human blood cells were used as quality control material. Finally, automating the washing and measurement protocol allowed for high reproducibility while reducing inter-observer variability.

The investigation of *blood cell aggregates as a new biomarker* was carried out by evaluating dynamics in formation and decay as well as analysing possible influencing variables. The effect of sample ageing on P-Aggregates varied widely depending on the anticoagulants used. In addition, storage of platelet concentrates for several days inevitably led to the formation of larger aggregates. The introduction of an in-vitro platelet activator helped to understand the dynamic processes involved in the formation and decay of aggregates. Once again, the choice of anticoagulant was shown to have a major impact on these dynamics.

A *clinical study on aggregates in COVID-19* was carried out to investigate the performance and suitability of this novel biomarker for clinical diagnostics. A high statistical significance between the number of P-Aggregates and the severity of the disease could be shown from the first day on. This highlights its potential as a diagnostic biomarker. With this novel phase imaging flow cytometer, not only numbers of P-Aggregates could be observed. Instead, the analysis of cells and aggregates was performed on four levels:

(1) P-Aggregate numbers, (2) P-Aggregate compositions, (3) individual and aggregated platelet diameters, and (4) individual and aggregated platelet phase related properties. All these parameters showed a good correlation with the patients' state of health. Also, LP-Aggregates showed a close connection to patients' severity levels but with lower significance than P-Aggregates. Furthermore, P-Aggregates were correlated with established biomarkers like D-Dimers and PCT, indicating a moderate connection. The behaviour of P-Aggregates was monitored longitudinally over 20 days using two patient examples. In both cases, a change in health status significantly impacted the measured parameters.

6.2 Outlook

In addition to this work, further extensions to the addressed objectives could be identified:

Steps towards a medical technology device: Besides the integrated automation for washing and measurement, an automated sample uptake would further reduce the complexity of operating the instrument. Within this automation, the developed autofocus showed promising results for homogeneous samples such as diluted blood. An extension of this approach would be beneficial for more heterogeneous samples to obtain a similar accuracy. The quality control materials presented in this work can be further evaluated. These include stability measurements for chicken erythrocytes, the reduction of phase shifts induced by droplet systems, and the investigation of droplet-in-droplet systems. For the labling of cells with micrometre-sized particles, additional materials of the beads with different refractive indices can be tested. Depending on the material, this would introduce a different phase shift, allowing parallel staining with more than one type of bead. This would enable something like a multicolour staining in fluorescence flow cytometry.

Blood cell aggregates as a new biomarker: Within this thesis, basic characteristics could be evaluated for a deeper understanding of the biomarkers, in particular for P-Aggregates. Due to the limited number of events, LP-Aggregates could not be characterised in depth. In future work, the protocol presented here could be extended to include a pre-processing step for the enrichment of LP-Aggregates. This can be achieved by reducing erythrocytes through chemical or microfluidic separation techniques. This thesis primarily analysed the aggregate formation and decay dynamics for healthy donors. Evaluating patient samples with a physiologically high number of aggregates could be the next step to further understanding this biomarker.

Clinical study on aggregates in COVID-19: The study presented here analysed the number and composition of aggregates as well as the morphologies of the involved cells. Based on the longitudinal measurements of two patients, the first indications of a possible prognostic power of this marker could be demonstrated. This prognostic validity and a potential predictive significance should be investigated in future studies. A validation of study results with established reference methods could provide further support. One example is the molecular analysis of macrothrombocytes to better understand their physiology. COVID-19 is not the only clinical case where blood cell aggregates are of high diagnostic

relevance. In a initial exploratory study, the impact of late sequelae of COVID-19 disease on the measured number of aggregates was observed. This was evident even after four months where the P-Aggregate number of 14.66 % were well above the reference range (Figure 6.1a). But also, in a patient with a predisposition to myocardial infarction, changes in the number of aggregates were seen. Finally, initial research has been carried out to see if increased immune responses affect the formation of blood cell aggregates. For this purpose, blood samples from three patients were taken just before and after vaccination, showing a significant increase of up to 900 % one hour after vaccination (Figure 6.1b). After 24 hours, most of the aggregates had disintegrated, and two out of three patients had levels within the healthy range. These first results appear promising and show the versatility of P-Aggregates as a new biomarker. However, further clinical studies with higher case numbers need to verify these findings. In summary, a first step was made to show the applicability of P-Aggregates in different fields. Additional studies in areas of sepsis, oncology, and cardiovascular diagnostics may help to further understand the patients' individual disease progressions. This may even be a step towards early detection of thrombosis.

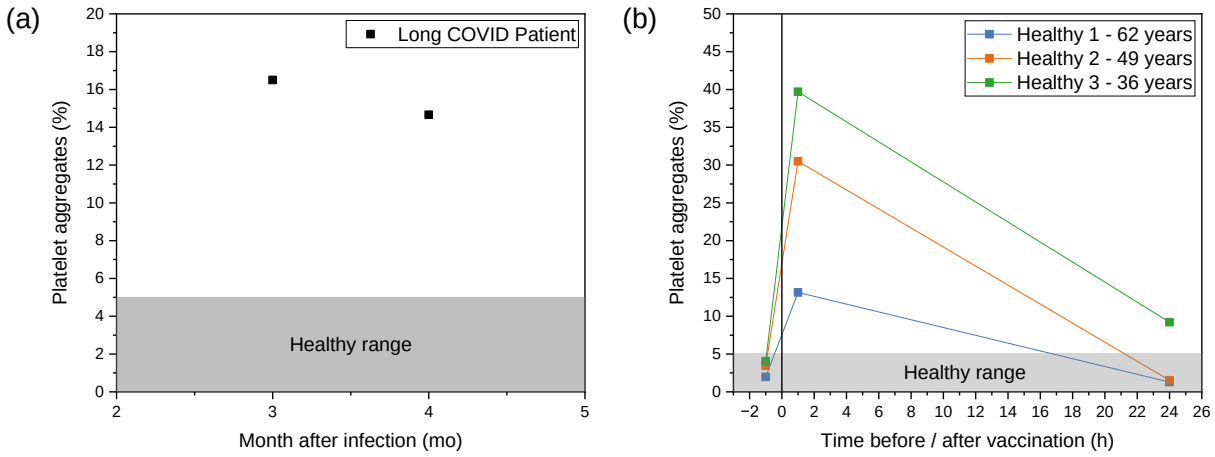

Figure 6.1: Exploratory studies for the application of P-Aggregates. **(a)** Measurement of P-Aggregates number of a patient with long-term problems after a COVID-19 infection. **(b)** P-Aggregate numbers before and after the vaccination of three healthy individuals with the COMIRNATY® vaccine.

A Appendix

A.1 Ethical Approval

The experiments were conducted in accordance with the declaration of Helsinki and approved by the ethics committee of the University Hospital rechts der Isar (221/20 S-SR and 620/21 S-KK). Informed consent was obtained from all subjects or their legal representatives.

A.2 Automation of the Measurement Setup

This chapter gives an overview of the automated steps, and top-level workflows are illustrated as flow diagrams. A more detailed description of the individual sub-programs and defined variables can be found in the bachelor's thesis by Thu Nguyen [205] and the master's thesis by Özgün Turgut [206]. Thu Nguyen's bachelor's thesis focused mainly on the automation of the washing and measurement, while Özgün Turgut added an additional autofocus and calibration for the stage. The automation of the setup was mainly done using LabView 2018. Python 3.6 was used for some image reconstruction steps and the implementation of the autofocus. At the time of writing, Python files up to version 3.6 can be executed within a LabView program, allowing the integration of both methods.

The automation of the setup can be divided into three main points: 1. sashing between each sample, 2. initialisation of the setup, and 3. measurement. The components used are a syringe pump, the DHM, a peristaltic pump, an injection valve, a 6-port valve, and tubings.

- The CETONI **syringe pump** system used consists of the base module "Base 120" and five low-pressure syringe pumps "Nemesys 290N". The base module contains the interface to the control PC and supplies power to the plugged-in modules. The syringe pumps can generate the microfluidic flow with the required high precision. The flow generated is pulsation-free and highly uniform in the mL/s to nL/s range. This is ensured by a PID-controlled drive unit that powers the syringe piston. To control the syringe pump system in LabVIEW, CETONI has created a separate LabVIEW sub-program for all Windows DLL function blocks. These so-called Virtual Instruments (VIs) are similar to a C function call of a Windows DLL. The provided VIs can be added to LabVIEW.

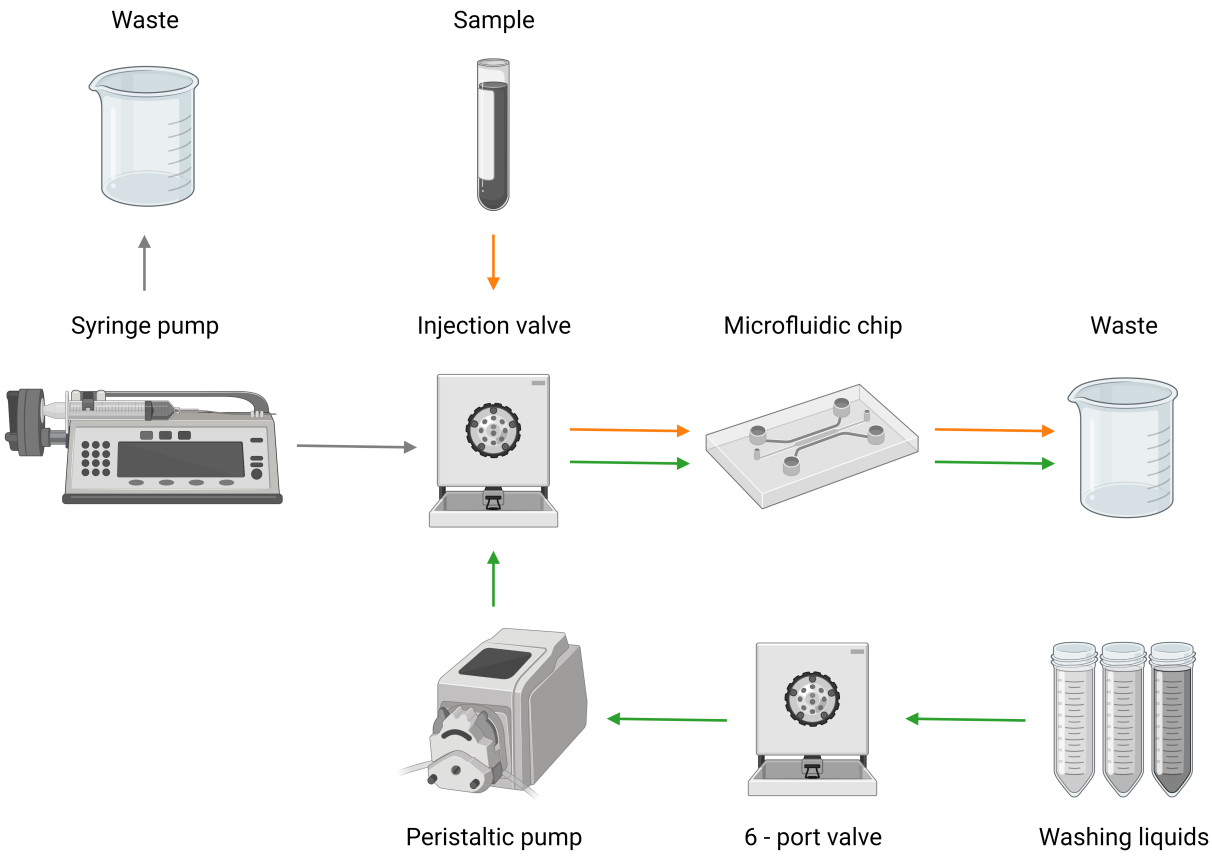

Figure A.1: Overview of the components used for the automated measurement setup. This includes washing liquids, a 6-port valve, a peristaltic pump, an injection valve, a microfluidic chip, a syringe pump, a sample and two different wastes. The coloured arrows indicate the direction of the workflow. Green arrows highlight the washing protocol, orange arrows the measurement protocol and grey arrows function of the syringe pump used in all protocols. The image was created with BioRender.com.

- The **DHM** has already been described in detail in chapter 3.2.1. Ovizio Imaging Systems has provided two different interfaces to control the microscope. These are a Web Service API and a Python API. The Web Service API provided is a RESTful web service. Ovizio Imaging Systems provides a Swagger document for the API. This RESTful web service can perform operations on four main resources. These are the *Image Reconstruction*, *Microscope*, *Project* and *Tasks*. The first enables the real-time reconstruction of the hologram images into phase and intensity images. The second allows microscope data and settings to be read or changed. It can also be used to start image acquisition. The third facilitates the creation of new folders and the organisation of previously acquired projects. The fourth allows the control of running processes. The Python API allows, among others, the reconstruction of phase and intensity images after a completed experiment.
- The **peristaltic pump** used is the "Ismatec IPC-N ISM936". This is a planetary

gear pump that actively drives eight stainless steel cylinders. The required tubes can be clamped onto CA Clock'n'go cassettes and placed on the stainless steel cylinders. The rotating cylinders push the liquid in the tubes from one side to the other. The pump can be used in different modes, such as pumping by rotations per minute, pumping by flow rate or dosing by volume. The manufacturer provides several VIs to control the peristaltic pump. This includes one VI for controlling the start and stop of the pump, one for selecting an operating mode and one for setting parameters.

- The Rheodyne **injection valve** can be operated in two modes, the "load" and "inject" modes. In "load", the sample loop is connected to a sample inlet and the waste, allowing it to be filled with a target solution. In "inject", the sample loop is connected to a syringe pump and the microfluidic channel. This causes the sample to be pumped into the channel at the flow rate of the syringe pump. As the valve switches between the two circuits in an airtight manner, the formation of air bubbles in the channel is avoided.
- The Rheodyne **6-way valve** is used to select the required cleaning fluid during the cleaning process. As the name suggests, the valve has six inputs and one output. Only three inputs are used for the three washing liquids in the cleaning protocol. As with the peristaltic pump, Rheodyne valve systems are supplied by the manufacturer with VIs for operating.
- Perfluoroalkoxyalkane (PFA) tubing with an inner diameter of 0.50 mm was used for the fluidic connection between the devices. The resulting dead volume between the sample inlet and the microfluidic chip of 49.09 µL results from the inner radius of 0.25 mm and the total length of the tubes of 250 mm.

A.2.1 Washing protocol

The washing protocol mainly solves the problem of cleaning the injection valve and microfluidic chip between two samples. It uses the 6-port valve, the peristaltic pump, the injection valve and the syringe pump. Figure A.2 shows the sequence as a flow diagram. Each shape colour represents a device, with green, brown, blue and orange representing the syringe pump, 6-way valve, injection valve and peristaltic pump, respectively. The sequence starts with the initialisation of the syringe pump flow. The flow rate of each syringe is set to 1 µL/s. The sequence of steps needed for the washing is similar for all three liquids. Only the number of repetitions is different. Usually, 2.5 % hypochlorite is used three times, 0.1 mol HCl two times and PBS once. Each sequence starts with setting the right washing liquid by changing the input of the 6-way valve. In addition, the injection valve is set to "load", allowing the sample loop to be loaded. The wash solution is delivered to the sample loop by starting the peristaltic pump. Once the sample loop is filled, the injection valve is set to "inject", connecting the sample loop to the syringe pump and the microfluidic channel. At this point, the peristaltic pump stops and the flow of the syringe pump push the washing liquid in the sample loop through the microfluidic chip. When all three wash liquids have been used, the script terminates.

Figure A.2: Flow diagram of the washing protocol. The washing protocol includes three washing steps with 2.5 % hypochlorite, two steps with 0.1 mol HCl and one with PBS. Each colour represents a different device.

A.2.2 Initialise protocol

The initialisation process should be carried out the first time the measurement setup is started. The protocol consists of two parallel processes. First, the removal of air bubbles in the tubing and microfluidic channel. Second, the prefilling of the washing liquids.

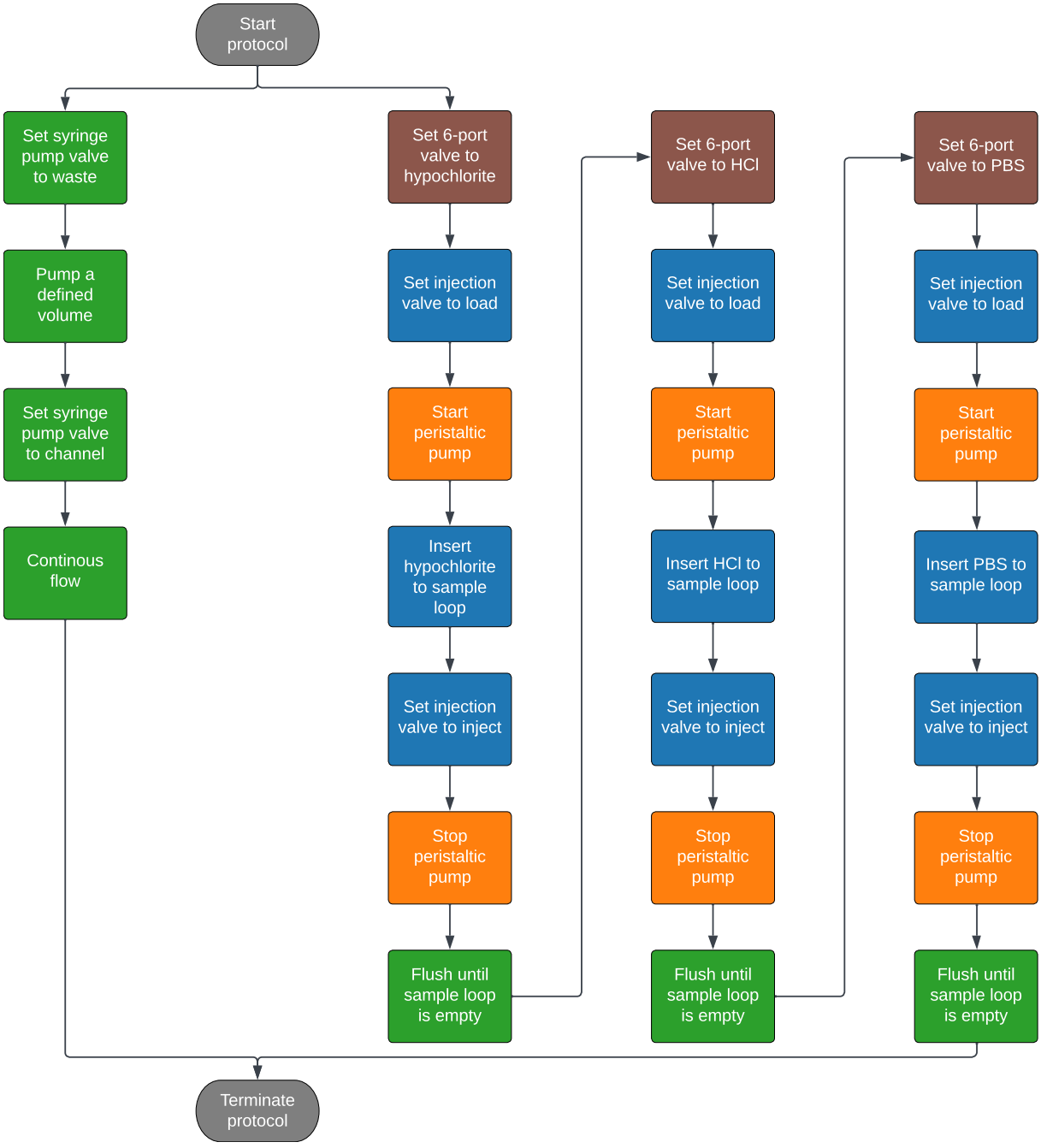

Figure A.3: Flow diagram of the initialise protocol. The initialise protocol includes two parallel processes. The removal of air in the microfluidic channel and washing of the sample loop. Each colour represents a different device.

The first protocol involves pumping a defined volume of 60 uL into the waste. For this, the syringe pump valve is set to "waste", and the syringes pump 60 s at a flow rate of 1 µL/s. This allows the removal of air bubbles that occur when fresh syringes are connected. The channel is flushed by setting the syringe pump valve to "channel" and pumping 300 uL for each syringe. This step should remove any remaining air bubbles in the tubing or the microfluidic channel.

In parallel, the washing liquids are filled into the sample loop. This sequence is similar to the steps in the washing protocol, but this time each washing liquid is used only once. Only after the finalisation of all steps, the syringe pump flow will be stopped and the protocol terminated.

A.2.3 Measurement protocol

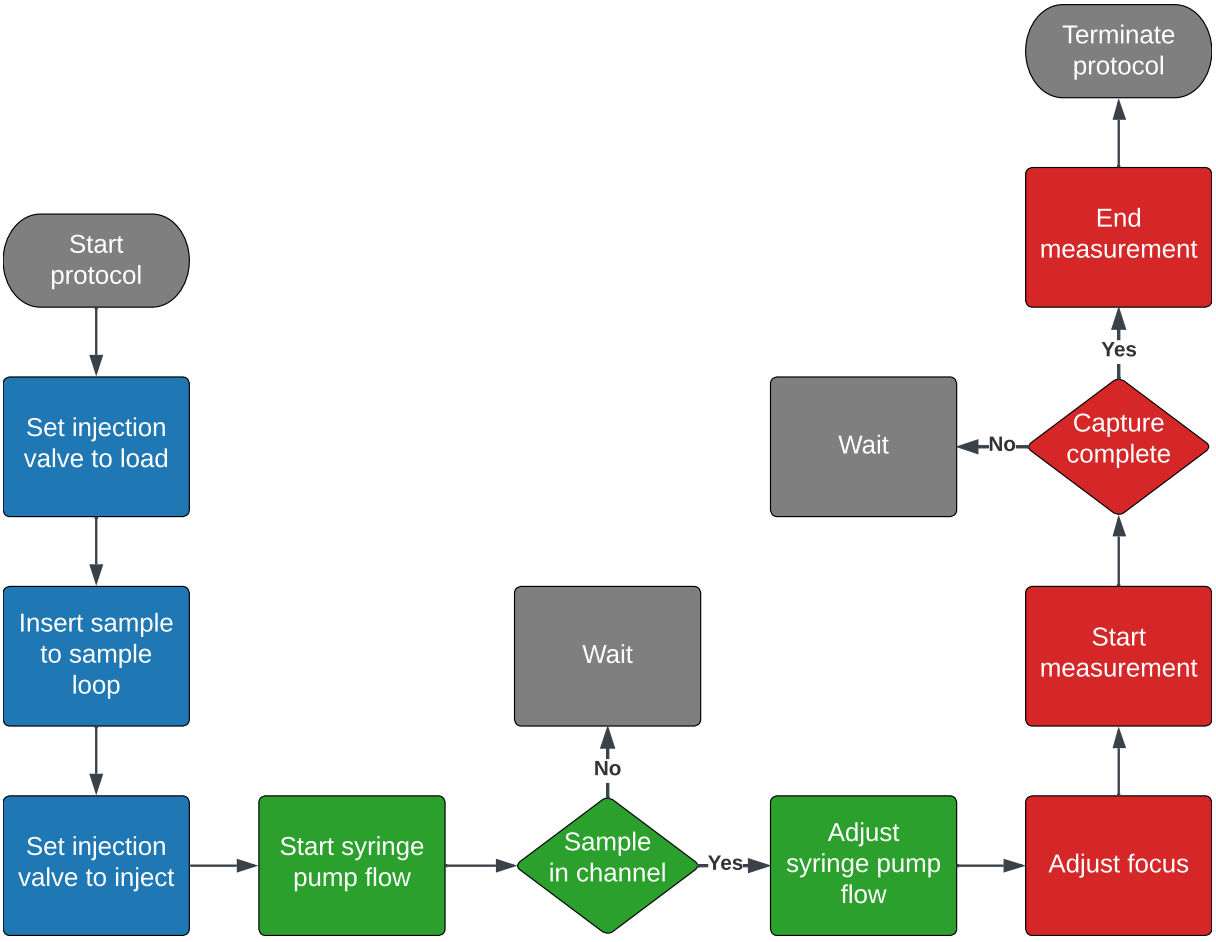

Figure A.4: Flow diagram of the measurement protocol. The measurement protocol includes the loading of the sample, injection into the channel and the performed measurement. Each colour represents a different device.

The measurement protocol consists of three steps: 1. injection of the sample, 2. flow of the sample towards the microfluidic chip, and 3. measurement of the sample. The first

two steps are performed by the injection valve (blue) and the syringe pump (green), while the last step is performed by the microscope (red). The time it takes for the sample to flow from the sample loop to the microfluidic chip has been theoretically calculated and experimentally tested. The main dependencies are the diameter and length of the tubing between the sample loop outlet and the chip. Since this distance doesn't change for the same setup, a fixed value estimates when the sample reaches the channel and the measurement can be started. A sample flow rate of 0.5 µL/s, side sheath flow rates of 0.5 µL/s, and top and bottom flow rates of 0.2 µL/s are used for the Fraunhofer channel. When the sample is in the channel, the sample flow rate is set to 0.2 µL/s to avoid motion blur effects. All other flow rates remain unchanged. A crucial point for a well-performed measurement is to use an appropriate z-position of the objective where the cells are in focus. Images can be read in real-time using the microscope's supplied APIs. Determining the sharpness function over the whole image, as shown in chapter 3.2.4, provides information on the proportion of cells in focus. The autofocus is now implemented so that the user can specify a range of objective positions where he expects the optimal focus point to be. It now iterates through all the values step by step whereby on step corresponds to 500 nm. For each lens position, nine images are taken, and the average of the Sobel gradient values is calculated. Nine images proved to be a good compromise between accuracy and time efficiency. The point with the highest sharpness value is determined and used for the measurement. The measurement is then performed automatically. A regular experiment consists of 10,000 images, allowing the user to change this value if required. After the defined number of images, the measurement is stopped, and the protocol is terminated.

A.3 List of Figures

A.4 List of Tables

Bibliography

[1] Narla Mohandas and Patrick G Gallagher. "Red cell membrane: past, present, and future". In: *Blood, The Journal of the American Society of Hematology* 112.10 (2008), pp. 3939–3948.

[2] Elkin Simson. "Historical perspective on cellular analysis". In: *Laboratory Hematology Practice* (2012), pp. 1–9.

[3] Peter Doherty. "The Red and white: ancient history". In: *Nature Reviews Immunology* 16.2 (2016), pp. 77–77.

[4] Bradley C Gehrs and Richard C Friedberg. "Autoimmune hemolytic anemia". In: *American journal of hematology* 69.4 (2002), pp. 258–271.

[5] Mariangela Palladino. "Complete blood count alterations in COVID-19 patients: A narrative review". In: *Biochemia medica* 31.3 (2021).

[6] Lindsay A Williams, Jun J Yang, Betsy A Hirsch, Erin L Marcotte, and Logan G Spector. "Is There Etiologic Heterogeneity between Subtypes of Childhood Acute Lymphoblastic Leukemia? A Review of Variation in Risk by SubtypeLiterature Review of Childhood ALL Risk Variation by Subtype". In: *Cancer Epidemiology, Biomarkers & Prevention* 28.5 (2019), pp. 846–856.

[7] Busadee Pratumvinit, Preechaya Wongkrajang, Kanit Reesukumal, Cherdsak Klinbua, and Patama Niamjoy. "Validation and optimization of criteria for manual smear review following automated blood cell analysis in a large university hospital". In: *Archives of Pathology & Laboratory Medicine* 137.3 (2013), pp. 408–414.

[8] Lisa Meintker, Jürgen Ringwald, Manfred Rauh, and Stefan W Krause. "Comparison of automated differential blood cell counts from Abbott Sapphire, Siemens Advia 120, Beckman Coulter DxH 800, and Sysmex XE-2100 in normal and pathologic samples". In: *American journal of clinical pathology* 139.5 (2013), pp. 641–650.

[9] Juan J Barcia. "The Giemsa stain: its history and applications". In: *International journal of surgical pathology* 15.3 (2007), pp. 292–296.

[10] K Dunning and AO Safo. "The ultimate Wright-Giemsa stain: 60 years in the making". In: *Biotechnic & Histochemistry* 86.2 (2011), pp. 69–75.

[11] Wim Van Der Meer, Warry Van Gelder, Ries de Keijzer, and Hans Willems. "The divergent morphological classification of variant lymphocytes in blood smears". In: *Journal of clinical pathology* 60.7 (2007), pp. 838–839.

[12] Robert V Pierre. "Peripheral blood film review: the demise of the eyecount leukocyte differential". In: *Clinics in laboratory medicine* 22.1 (2002), pp. 279–297.

[13] James W Bacus. “The observer error in peripheral blood cell classification”. In: *American Journal of Clinical Pathology* 59.2 (1973), pp. 223–230.

[14] Leonore A Herzenberg, Stephen C De Rosa, and Leonard A Herzenberg. “Monoclonal antibodies and the FACS: complementary tools for immunobiology and medicine”. In: *Immunology today* 21.8 (2000), pp. 383–390.

[15] David A Basiji. “Principles of Amnis imaging flow cytometry”. In: *Imaging Flow Cytometry: Methods and Protocols* (2016), pp. 13–21.

[16] Hideharu Mikami, Makoto Kawaguchi, Chun-Jung Huang, Hiroki Matsumura, Takeaki Sugimura, Kangrui Huang, Cheng Lei, et al. “Virtual-freezing fluorescence imaging flow cytometry”. In: *Nature communications* 11.1 (2020), p. 1162.

[17] Mazin Z Othman, Thabit S Mohammed, and Alaa B Ali. “Neural network classification of white blood cell using microscopic images”. In: *International Journal of Advanced Computer Science and Applications* 8.5 (2017).

[18] Md Zahangir Alom, Chris Yakopcic, Tarek M Taha, and Vijayan K Asari. “Microscopic blood cell classification using inception recurrent residual convolutional neural networks”. In: *NAECON 2018-IEEE National Aerospace and Electronics Conference*. IEEE. 2018, pp. 222–227.

[19] T Lavanya and S Sushritha. “Detection of sickle cell anemia and thalassemia using image processing techniques”. In: *International Journal of Innovative Science and Research Technology* 2.12 (2017), pp. 399–405.

[20] Mahdieh Poostchi, Kamolrat Silamut, Richard J Maude, Stefan Jaeger, and George Thoma. “Image analysis and machine learning for detecting malaria”. In: *Translational Research* 194 (2018), pp. 36–55.

[21] FE Al-Tahhan, Ali A Sakr, Doaa A Aladle, and ME Fares. “Improved image segmentation algorithms for detecting types of acute lymphatic leukaemia”. In: *IET Image Processing* 13.13 (2019), pp. 2595–2603.

[22] Matthias Ugele, Markus Weniger, Maria Leidenberger, Yiwei Huang, Michael Bassler, Oliver Friedrich, Barbara Kappes, et al. “Label-free, high-throughput detection of P. falciparum infection in sphered erythrocytes with digital holographic microscopy”. In: *Lab on a Chip* 18.12 (2018), pp. 1704–1712.

[23] Matthias Ugele, Markus Weniger, Manfred Stanzel, Michael Bassler, Stefan W Krause, Oliver Friedrich, Oliver Hayden, et al. “Label-free high-throughput leukemia detection by holographic microscopy”. In: *Advanced Science* 5.12 (2018), p. 1800761.

[24] YongKeun Park, Christian Depeursinge, and Gabriel Popescu. “Quantitative phase imaging in biomedicine”. In: *Nature photonics* 12.10 (2018), pp. 578–589.

[25] William J Croft. *Under the microscope: a brief history of microscopy*. Vol. 5. World Scientific, 2006.

[26] A Anand, V Chhaniwal, and B Javidi. “Tutorial: common path self-referencing digital holographic microscopy”. In: *APL Photonics* 3.7 (2018), p. 071101.

[27] Pinhas Girshovitz and Natan T Shaked. “Real-time quantitative phase reconstruction in off-axis digital holography using multiplexing”. In: *Optics Letters* 39.8 (2014), pp. 2262–2265.

[28] Frits Zernike. “How I discovered phase contrast”. In: *Science* 121.3141 (1955), pp. 345–349.

[29] Dennis Gabor. “A new microscopic principle”. In: *nature* 161 (1948), pp. 777–778.

[30] Adolf Lohmann. “Optische einseitenbandübertragung angewandt auf das Gabor-Mikroskop”. In: *Optica Acta: International Journal of Optics* 3.2 (1956), pp. 97–99.

[31] Emmett N Leith and Juris Upatnieks. “Reconstructed wavefronts and communication theory”. In: *JOSA* 52.10 (1962), pp. 1123–1130.

[32] Pietro Ferraro, Adam Wax, and Zeev Zalevsky. *Coherent light microscopy: Imaging and quantitative phase analysis*. Vol. 46. Springer Science & Business Media, 2011.

[33] Basanta Bhaduri and Gabriel Popescu. “Derivative method for phase retrieval in off-axis quantitative phase imaging”. In: *Optics letters* 37.11 (2012), pp. 1868–1870.

[34] B Kemper, A Bauwens, D Bettenworth, M Götte, B Greve, L Kastl, S Ketelhut, et al. “Label-free quantitative in vitro live cell imaging with digital holographic microscopy”. In: *Label-Free Monitoring of Cells in vitro* (2019), pp. 219–272.

[35] Leonid Yaroslavsky. *Digital holography and digital image processing: principles, methods, algorithms*. Springer Science & Business Media, 2003.

[36] Ulf Schnars and Werner PO Jüptner. “Digital recording and numerical reconstruction of holograms”. In: *Measurement science and technology* 13.9 (2002), R85.

[37] Björn Kemper and Gert Von Bally. “Digital holographic microscopy for live cell applications and technical inspection”. In: *Applied optics* 47.4 (2008), A52–A61.

[38] Ichirou Yamaguchi. “Phase-shifting digital holography”. In: *Digital Holography and Three-Dimensional Display*. Springer, 2006, pp. 145–171.

[39] Myung K Kim. “Principles and techniques of digital holographic microscopy”. In: *SPIE reviews* 1.1 (2010), p. 018005.

[40] KyeoReh Lee, Kyoohyun Kim, Jaehwang Jung, JiHan Heo, Sangyeon Cho, Sangyun Lee, Gyuyoung Chang, et al. “Quantitative phase imaging techniques for the study of cell pathophysiology: from principles to applications”. In: *Sensors* 13.4 (2013), pp. 4170–4191.

[41] K Weir, WJO Boyle, BT Meggit, AW Palmer, and KTV Grattan. “A novel adaptation of the Michelson interferometer for the measurement of vibration”. In: *Journal of lightwave technology* 10.5 (1992), pp. 700–703.

[42] YongKeun Park, Monica Diez-Silva, Gabriel Popescu, George Lykotrafitis, Wonshik Choi, Michael S Feld, and Subra Suresh. “Refractive index maps and membrane dynamics of human red blood cells parasitized by Plasmodium falciparum”. In: *Proceedings of the National Academy of Sciences* 105.37 (2008), pp. 13730–13735.

[43] Gabriel Popescu, Takahiro Ikeda, Ramachandra R Dasari, and Michael S Feld. "Diffraction phase microscopy for quantifying cell structure and dynamics". In: *Optics letters* 31.6 (2006), pp. 775–777.

[44] Gabriel Popescu, Kamran Badizadegan, Ramachandra R Dasari, and Michael S Feld. "Observation of dynamic subdomains in red blood cells". In: *Journal of biomedical optics* 11.4 (2006), p. 040503.

[45] Pinhas Girshovitz and Natan T Shaked. "Compact and portable low-coherence interferometer with off-axis geometry for quantitative phase microscopy and nanoscopy". In: *Optics express* 21.5 (2013), pp. 5701–5714.

[46] Jaeduck Jang, Chae Yun Bae, Je-Kyun Park, and Jong Chul Ye. "Self-reference quantitative phase microscopy for microfluidic devices". In: *Optics letters* 35.4 (2010), pp. 514–516.

[47] David J Beebe, Glennys A Mensing, Glenn M Walker, et al. "Physics and applications of microfluidics in biology". In: *Annual review of biomedical engineering* 4.1 (2002), pp. 261–286.

[48] Peter Gravesen, Jens Branebjerg, and O Søndergård Jensen. "Microfluidics-a review". In: *Journal of micromechanics and microengineering* 3.4 (1993), p. 168.

[49] Philip M Gerhart, Andrew L Gerhart, and John I Hochstein. *Munson, Young and Okiishi's fundamentals of fluid mechanics*. John Wiley & Sons, 2016.

[50] Henrik Bruus. *Theoretical microfluidics*. Vol. 18. Oxford university press, 2007.

[51] AB Metzner and RE Otto. "Agitation of non-Newtonian fluids". In: *AIChE Journal* 3.1 (1957), pp. 3–10.

[52] Sarvesh Varma and Joel Voldman. "A cell-based sensor of fluid shear stress for microfluidics". In: *Lab on a Chip* 15.6 (2015), pp. 1563–1573.

[53] Henrik Bruus. "Governing equations in microfluidics". In: (2014).

[54] Chao Liu, Chundong Xue, Jiashu Sun, and Guoqing Hu. "A generalized formula for inertial lift on a sphere in microchannels". In: *Lab on a Chip* 16.5 (2016), pp. 884–892.

[55] J Kim, J Lee, C Wu, S Nam, Dino Di Carlo, and Wonhee Lee. "Inertial focusing in non-rectangular cross-section microchannels and manipulation of accessible focusing positions". In: *Lab on a Chip* 16.6 (2016), pp. 992–1001.

[56] G Segre and A Silberberg. "Radial particle displacements in Poiseuille flow of suspensions". In: *Nature* 189 (1961), pp. 209–210.

[57] Yixing Gou, Yixuan Jia, Peng Wang, and Changku Sun. "Progress of inertial microfluidics in principle and application". In: *Sensors* 18.6 (2018), p. 1762.

[58] Chao Liu, Chundong Xue, Xiaodong Chen, Lei Shan, Yu Tian, and Guoqing Hu. "Size-based separation of particles and cells utilizing viscoelastic effects in straight microchannels". In: *Analytical chemistry* 87.12 (2015), pp. 6041–6048.

[59] A Karimi, S Yazdi, and AM Ardekani. "Hydrodynamic mechanisms of cell and particle trapping in microfluidics". In: *Biomicrofluidics* 7.2 (2013), p. 021501.

[60] Joel P Golden, Gusphyl A Justin, Mansoor Nasir, and Frances S Ligler. "Hydrodynamic focusing—a versatile tool". In: *Analytical and bioanalytical chemistry* 402.1 (2012), pp. 325–335.

[61] Axel Günther and Klavs F Jensen. "Multiphase microfluidics: from flow characteristics to chemical and materials synthesis". In: *Lab on a Chip* 6.12 (2006), pp. 1487–1503.

[62] Todd Thorsen, Richard W Roberts, Frances H Arnold, and Stephen R Quake. "Dynamic pattern formation in a vesicle-generating microfluidic device". In: *Physical review letters* 86.18 (2001), p. 4163.

[63] Carsten Cramer, Peter Fischer, and Erich J Windhab. "Drop formation in a co-flowing ambient fluid". In: *Chemical Engineering Science* 59.15 (2004), pp. 3045–3058.

[64] Shelley L Anna, Nathalie Bontoux, and Howard A Stone. "Formation of dispersions using "flow focusing" in microchannels". In: *Applied physics letters* 82.3 (2003), pp. 364–366.

[65] Shelley L Anna and Hans C Mayer. "Microscale tipstreaming in a microfluidic flow focusing device". In: *Physics of fluids* 18.12 (2006), p. 121512.

[66] Wingki Lee, Lynn M Walker, and Shelley L Anna. "Role of geometry and fluid properties in droplet and thread formation processes in planar flow focusing". In: *Physics of Fluids* 21.3 (2009), p. 032103.

[67] Ali Lashkaripour, Christopher Rodriguez, Luis Ortiz, and Douglas Densmore. "Performance tuning of microfluidic flow-focusing droplet generators". In: *Lab on a Chip* 19.6 (2019), pp. 1041–1053.

[68] Eike S Debus and Walter Gross-Fengels. *Operative und interventionelle Gefäßmedizin*. Springer-Verlag, 2019.

[69] coachrom diagnostica. *Produktportfolio*. URL: `https://www.coachrom.com/produkte/ueberblick-produktportfolio` (visited on 11/01/2023).

[70] M Gawaz. "Antithrombozytäre Substanzen". In: *Das Blutplättchen* (1999), pp. 54–79.

[71] Edward Cedrone, Barry W Neun, Jamie Rodriguez, Alison Vermilya, Jeffrey D Clogston, Scott E McNeil, Yechezkel Barenholz, et al. "Anticoagulants influence the performance of in vitro assays intended for characterization of nanotechnology-based formulations". In: *Molecules* 23.1 (2017), p. 12.

[72] Jasmijn A van Balveren, Mirelle JAJ Huijskens, Eugenie FA Gemen, Nathalie CV Péquériaux, and Ron Kusters. "Effects of time and temperature on 48 routine chemistry, haematology and coagulation analytes in whole blood samples". In: *Annals of Clinical Biochemistry* 54.4 (2017), pp. 448–462.

[73] Jennifer Yee and Colin G Kaide. "Emergency reversal of anticoagulation". In: *Western Journal of Emergency Medicine* 20.5 (2019), p. 770.

[74] Chang-geng Song, Li-jie Bi, Jing-jing Zhao, Xuan Wang, Wen Li, Fang Yang, and Wen Jiang. "The efficacy and safety of Hirudin plus Aspirin versus Warfarin in the secondary prevention of Cardioembolic Stroke due to Nonvalvular Atrial Fibrillation: A multicenter prospective cohort study". In: *International journal of medical sciences* 18.5 (2021), p. 1167.

[75] Jianguo Jin, James L Daniel, and Satya P Kunapuli. "Molecular basis for ADP-induced platelet activation: II. The P2Y1 receptor mediates ADP-induced intracellular calcium mobilization and shape change in platelets". In: *Journal of Biological Chemistry* 273.4 (1998), pp. 2030–2034.

[76] Mark L Kahn, Mayumi Nakanishi-Matsui, Michael J Shapiro, Hiroaki Ishihara, Shaun R Coughlin, et al. "Protease-activated receptors 1 and 4 mediate activation of human platelets by thrombin". In: *The Journal of clinical investigation* 103.6 (1999), pp. 879–887.

[77] David Whiting and James A DiNardo. "TEG and ROTEM: technology and clinical applications". In: *American journal of hematology* 89.2 (2014), pp. 228–232.

[78] Dirk Sibbing, Siegmund Braun, Stefan Jawansky, Wolfgang Vogt, Julinda Mehilli, Albert Schömig, Adnan Kastrati, et al. "Assessment of ADP-induced platelet aggregation with light transmission aggregometry and multiple electrode platelet aggregometry before and after clopidogrel treatment". In: *Thrombosis and haemostasis* 99.01 (2008), pp. 121–126.

[79] N Håkan Wallén, Mehdi Ladjevardi, Johanna Albert, and Anders Bröijersén. "Influence of different anticoagulants on platelet aggregation in whole blood; a comparison between citrate, low molecular mass heparin and hirudin". In: *Thrombosis research* 87.1 (1997), pp. 151–157.

[80] Ellinor I Peerschke and Marjorie B Zucker. "Fibrinogen receptor exposure and aggregation of human blood platelets produced by ADP and chilling". In: *Blood* 57.4 (1981), pp. 663–670.

[81] Michaela Finsterbusch, Waltraud C Schrottmaier, Julia B Kral-Pointner, Manuel Salzmann, and Alice Assinger. "Measuring and interpreting platelet-leukocyte aggregates". In: *Platelets* 29.7 (2018), pp. 677–685.

[82] Julia Barbara Kral, Waltraud Cornelia Schrottmaier, Manuel Salzmann, and Alice Assinger. "Platelet interaction with innate immune cells". In: *Transfusion Medicine and Hemotherapy* 43.2 (2016), pp. 78–88.

[83] Waltraud C Schrottmaier, Julia B Kral, Sigrun Badrnya, and Alice Assinger. "Aspirin and P2Y12 Inhibitors in platelet-mediated activation of neutrophils and monocytes". In: *Thrombosis and haemostasis* 114.09 (2015), pp. 478–789.

[84] Braedon McDonald, Rossana Urrutia, Bryan G Yipp, Craig N Jenne, and Paul Kubes. "Intravascular neutrophil extracellular traps capture bacteria from the bloodstream during sepsis". In: *Cell host & microbe* 12.3 (2012), pp. 324–333.

[85] Stephen R Clark, Adrienne C Ma, Samantha A Tavener, Braedon McDonald, Zahra Goodarzi, Margaret M Kelly, Kamala D Patel, et al. “Platelet TLR4 activates neutrophil extracellular traps to ensnare bacteria in septic blood”. In: *Nature medicine* 13.4 (2007), pp. 463–469.

[86] Sigrun Badrnya, Waltraud C Schrottmaier, Julia B Kral, Koon-Chu Yaiw, Ivo Volf, Gernot Schabbauer, Cecilia Söderberg-Nauclér, et al. “Platelets mediate oxidized low-density lipoprotein–induced monocyte extravasation and foam cell formation”. In: *Arteriosclerosis, thrombosis, and vascular biology* 34.3 (2014), pp. 571–580.

[87] Christina Christersson, Matilda Johnell, and Agneta Siegbahn. “Tissue factor and IL8 production by P-selectin-dependent platelet–monocyte aggregates in whole blood involves phosphorylation of Lyn and is inhibited by IL10”. In: *Journal of Thrombosis and Haemostasis* 6.6 (2008), pp. 986–994.

[88] Andrew S Weyrich, Mark R Elstad, Rodger P McEver, Thomas M McIntyre, Kevin L Moore, James H Morrissey, Stephen M Prescott, et al. “Activated platelets signal chemokine synthesis by human monocytes.” In: *The Journal of clinical investigation* 97.6 (1996), pp. 1525–1534.

[89] Matteo Iannacone, Giovanni Sitia, Masanori Isogawa, Patrizia Marchese, Maria G Castro, Pedro R Lowenstein, Francis V Chisari, et al. “Platelets mediate cytotoxic T lymphocyte–induced liver damage”. In: *Nature medicine* 11.11 (2005), pp. 1167–1169.

[90] Junichi Hirahashi, Keiichi Hishikawa, Shinya Kaname, Naotake Tsuboi, Yunmei Wang, Daniel I Simon, George Stavrakis, et al. “Mac-1 (CD11b/CD18) links inflammation and thrombosis after glomerular injury”. In: *Circulation* 120.13 (2009), pp. 1255–1265.

[91] N Kasai, A Parbtani, JS Cameron, V Yewdall, P Shepherd, and P Verroust. “Platelet-aggregating immune complexes and intraplatelet serotonin in idiopathic glomerulonephritis and systemic lupus.” In: *Clinical and Experimental Immunology* 43.1 (1981), p. 64.

[92] Kristin N Kornerup, Gary P Salmon, Simon C Pitchford, Wai L Liu, and Clive P Page. “Circulating platelet-neutrophil complexes are important for subsequent neutrophil activation and migration”. In: *Journal of applied physiology* (2010).

[93] Eugenio D Hottz, Anna Cecillia Quirino-Teixeira, Laura Botelho Merij, Mariana Brandi Mendonca Pinheiro, Stephane Vicente Rozini, Fernando A Bozza, and Patricia T Bozza. “Platelet–leukocyte interactions in the pathogenesis of viral infections”. In: *Platelets* 33.2 (2022), pp. 200–207.

[94] Nicole Allen, Tessa J Barrett, Yu Guo, Michael Nardi, Bhama Ramkhelawon, Caron B Rockman, Judith S Hochman, et al. “Circulating monocyte-platelet aggregates are a robust marker of platelet activity in cardiovascular disease”. In: *Atherosclerosis* 282 (2019), pp. 11–18.

[95] Tatsuya Ishikawa, Mie Shimizu, Saori Kohara, Shunya Takizawa, Yasuhisa Kitagawa, and Shigeharu Takagi. "Appearance of WBC-platelet complex in acute ischemic stroke, predominantly in atherothrombotic infarction". In: *Journal of atherosclerosis and thrombosis* (2012), pp. 1201230469–1201230469.

[96] KK Wu and JC Hoak. "A new method for the quantitative detection of platelet aggregates in patients with arterial insufficiency". In: *The Lancet* 304.7886 (1974), pp. 924–926.

[97] Alexandros Rampotas and Sue Pavord. "Platelet aggregates, a marker of severe COVID-19 disease". In: *Journal of Clinical Pathology* 74.11 (2021), pp. 750–751.

[98] Cristina Stasi, Silvia Fallani, Fabio Voller, and Caterina Silvestri. "Treatment for COVID-19: An overview". In: *European journal of pharmacology* 889 (2020), p. 173644.

[99] Kiran Shekar, Jenelle Badulak, Giles Peek, Udo Boeken, Heidi J Dalton, Lovkesh Arora, Bishoy Zakhary, et al. "Extracorporeal life support organization coronavirus disease 2019 interim guidelines: a consensus document from an international group of interdisciplinary extracorporeal membrane oxygenation providers". In: *Asaio Journal* (2020).

[100] Bernd Engelmann and Steffen Massberg. "Thrombosis as an intravascular effector of innate immunity". In: *Nature Reviews Immunology* 13.1 (2013), pp. 34–45.

[101] Steffen Massberg, Lenka Grahl, Marie-Luise von Bruehl, Davit Manukyan, Susanne Pfeiler, Christian Goosmann, Volker Brinkmann, et al. "Reciprocal coupling of coagulation and innate immunity via neutrophil serine proteases". In: *Nature medicine* 16.8 (2010), pp. 887–896.

[102] Konstantin Stark and Steffen Massberg. "Interplay between inflammation and thrombosis in cardiovascular pathology". In: *Nature Reviews Cardiology* 18.9 (2021), pp. 666–682.

[103] Edward M Conway, Nigel Mackman, Ronald Q Warren, Alisa S Wolberg, Laurent O Mosnier, Robert A Campbell, Lisa E Gralinski, et al. "Understanding COVID-19-associated coagulopathy". In: *Nature Reviews Immunology* 22.10 (2022), pp. 639–649.

[104] Aldo Bonaventura, Alessandra Vecchié, Lorenzo Dagna, Kimberly Martinod, Dave L Dixon, Benjamin W Van Tassell, Francesco Dentali, et al. "Endothelial dysfunction and immunothrombosis as key pathogenic mechanisms in COVID-19". In: *Nature Reviews Immunology* 21.5 (2021), pp. 319–329.

[105] Maximilian Ackermann, Stijn E Verleden, Mark Kuehnel, Axel Haverich, Tobias Welte, Florian Laenger, Arno Vanstapel, et al. "Pulmonary vascular endothelialitis, thrombosis, and angiogenesis in Covid-19". In: *New England Journal of Medicine* 383.2 (2020), pp. 120–128.

[106] Mehdi Sakka, Jean M Connors, Guillaume Hékimian, Isabelle Martin-Toutain, Benjamin Crichi, Ines Colmegna, Dominique Bonnefont-Rousselot, et al. "Association between D-Dimer levels and mortality in patients with coronavirus disease 2019 (COVID-19): a systematic review and pooled analysis". In: *JMV-Journal de Médecine Vasculaire* 45.5 (2020), pp. 268–274.

[107] Diana A Gorog, Robert F Storey, Paul A Gurbel, Udaya S Tantry, Jeffrey S Berger, Mark Y Chan, Daniel Duerschmied, et al. "Current and novel biomarkers of thrombotic risk in COVID-19: a Consensus Statement from the International COVID-19 Thrombosis Biomarkers Colloquium". In: *Nature Reviews Cardiology* (2022), pp. 1–21.

[108] Nathaniel R Smilowitz, Dennis Kunichoff, Michael Garshick, Binita Shah, Michael Pillinger, Judith S Hochman, and Jeffrey S Berger. "C-reactive protein and clinical outcomes in patients with COVID-19". In: *European heart journal* 42.23 (2021), pp. 2270–2279.

[109] ATTACC, ACTIV-4a, and REMAP-CAP Investigators. "Therapeutic anticoagulation with heparin in noncritically ill patients with Covid-19". In: *New England Journal of Medicine* 385.9 (2021), pp. 790–802.

[110] Renato D Lopes, Remo HM Furtado, Ariane Vieira Scarlatelli Macedo, Bruna Bronhara, Lucas Petri Damiani, Lilian Mazza Barbosa, Júlia de Aveiro Morata, et al. "Therapeutic versus prophylactic anticoagulation for patients admitted to hospital with COVID-19 and elevated D-dimer concentration (ACTION): an open-label, multicentre, randomised, controlled trial". In: *The Lancet* 397.10291 (2021), pp. 2253–2263.

[111] Tessa J Barrett, MacIntosh Cornwell, Khrystyna Myndzar, Christina C Rolling, Yuhe Xia, Kamelia Drenkova, Antoine Biebuyck, et al. "Platelets amplify endotheliopathy in COVID-19". In: *Science advances* 7.37 (2021), eabh2434.

[112] Karina Althaus, Irene Marini, Jan Zlamal, Lisann Pelzl, Anurag Singh, Helene Häberle, Martin Mehrländer, et al. "Antibody-induced procoagulant platelets in severe COVID-19 infection". In: *Blood* 137.8 (2021), pp. 1061–1071.

[113] Nicola Lazzarini, Avgoustinos Filippoupolitis, Pedro Manzione, and Hariklia Eleftherohorinou. "A machine learning model on Real World Data for predicting progression to Acute Respiratory Distress Syndrome (ARDS) among COVID-19 patients". In: *PLoS One* 17.7 (2022), e0271227.

[114] Mohamed El-Kassas, Maha El Gaafary, Mohamed Elbadry, Mohamed A Medhat, Hany Dabbous, Essam A Hassan, Ahmed Abdelmoaty, et al. "The COVEG score to predict severity and mortality among hospitalized patients with COVID-19". In: *The Journal of Infection in Developing Countries* 16.07 (2022), pp. 1138–1147.

[115] Laure Wynants, Ben Van Calster, Gary S Collins, Richard D Riley, Georg Heinze, Ewoud Schuit, Marc MJ Bonten, et al. "Prediction models for diagnosis and prognosis of covid-19: systematic review and critical appraisal". In: *bmj* 369 (2020).

[116] Leo Nicolai, Alexander Leunig, Sophia Brambs, Rainer Kaiser, Tobias Weinberger, Michael Weigand, Maximilian Muenchhoff, et al. "Immunothrombotic dysregulation in COVID-19 pneumonia is associated with respiratory failure and coagulopathy". In: *Circulation* 142.12 (2020), pp. 1176–1189.

[117] Younes Zaid, Florian Puhm, Isabelle Allaeys, Abdallah Naya, Mounia Oudghiri, Loubna Khalki, Youness Limami, et al. "Platelets can associate with SARS-Cov-2 RNA and are hyperactivated in COVID-19". In: *Circulation research* 127.11 (2020), pp. 1404–1418.

[118] Masako Nishikawa, Hiroshi Kanno, Yuqi Zhou, Ting-Hui Xiao, Takuma Suzuki, Yuma Ibayashi, Jeffrey Harmon, et al. "Massive image-based single-cell profiling reveals high levels of circulating platelet aggregates in patients with COVID-19". In: *Nature communications* 12.1 (2021), pp. 1–12.

[119] Sean X Gu, Tarun Tyagi, Kanika Jain, Vivian W Gu, Seung Hee Lee, Jonathan M Hwa, Jennifer M Kwan, et al. "Thrombocytopathy and endotheliopathy: crucial contributors to COVID-19 thromboinflammation". In: *Nature Reviews Cardiology* 18.3 (2021), pp. 194–209.

[120] Minal D Joshi, Atul H Karode, and SR Suralkar. "White blood cells segmentation and classification to detect acute leukemia". In: *International Journal of Emerging Trends & Technology in Computer Science (IJETTCS)* 2.3 (2013), pp. 147–151.

[121] Mauro Buttarello and Mario Plebani. "Automated blood cell counts: state of the art". In: *American journal of clinical pathology* 130.1 (2008), pp. 104–116.

[122] Benjamin Rubio-Jurado, Lluvia Sugey Sosa-Quintero, Ivette Lenina Carrasco-Martinez, Armando Norato-Delgado, Eduardo Garcia-Luna, Sandra Guzman-Silahua, Carlos Riebeling-Navarro, et al. "New biomarkers in non-Hodgkin lymphoma and acute leukemias". In: *Advances in Clinical Chemistry* 96 (2020), pp. 19–53.

[123] JF Martin, T Shaw, J Heggie, and DG Penington. "Measurement of the density of human platelets and its relationship to volume". In: *British journal of haematology* 54.3 (1983), pp. 337–352.

[124] Susanne Melzer, Silke Zachariae, Jozsef Bocsi, Christoph Engel, Markus Löffler, and Attila Tárnok. "Reference intervals for leukocyte subsets in adults: results from a population-based study using 10-color flow cytometry". In: *Cytometry Part B: Clinical Cytometry* 88.4 (2015), pp. 270–281.

[125] Xiangyu Quan, Kouichi Nitta, Osamu Matoba, Peng Xia, and Yasuhiro Awatsuji. "Phase and fluorescence imaging by combination of digital holographic microscopy and fluorescence microscopy". In: *Optical Review* 22 (2015), pp. 349–353.

[126] Manoj Kumar, Xiangyu Quan, Yasuhiro Awatsuji, Yosuke Tamada, and Osamu Matoba. "Digital holographic multimodal cross-sectional fluorescence and quantitative phase imaging system". In: *Scientific Reports* 10.1 (2020), p. 7580.

[127] Erik M Shapiro, Laura N Medford-Davis, Tarek M Fahmy, Cynthia E Dunbar, and Alan P Koretsky. "Antibody-mediated cell labeling of peripheral T cells with micron-sized iron oxide particles (MPIOs) allows single cell detection by MRI". In: *Contrast media & molecular imaging* 2.3 (2007), pp. 147–153.

[128] Maciej Zborowski and Jeffrey J Chalmers. “Magnetic cell sorting”. In: *Immunochemical Protocols* (2005), pp. 291–300.

[129] Giovanni Romeo, Gaetano D’Avino, Francesco Greco, Paolo A Netti, and Pier Luca Maffettone. “Viscoelastic flow-focusing in microchannels: scaling properties of the particle radial distributions”. In: *Lab on a Chip* 13.14 (2013), pp. 2802–2807.

[130] Gaetano D’Avino, Giovanni Romeo, Massimiliano M Villone, Francesco Greco, Paolo A Netti, and Pier Luca Maffettone. “Single line particle focusing induced by viscoelasticity of the suspending liquid: theory, experiments and simulations to design a micropipe flow-focuser”. In: *Lab on a Chip* 12.9 (2012), pp. 1638–1645.

[131] Francesco Del Giudice, Giovanni Romeo, Gaetano D’Avino, Francesco Greco, Paolo A Netti, and Pier Luca Maffettone. “Particle alignment in a viscoelastic liquid flowing in a square-shaped microchannel”. In: *Lab on a Chip* 13.21 (2013), pp. 4263–4271.

[132] Sukgyun Cha, Kyowon Kang, Jae Bem You, Sung Gap Im, Younghun Kim, and Ju Min Kim. “Hoop stress-assisted three-dimensional particle focusing under viscoelastic flow”. In: *Rheologica Acta* 53 (2014), pp. 927–933.

[133] Murat Serhatlioglu, Mohammad Asghari, Mustafa Tahsin Guler, and Caglar Elbuken. “Impedance-based viscoelastic flow cytometry”. In: *Electrophoresis* 40.6 (2019), pp. 906–913.

[134] Haidong Feng, Alexander R Jafek, Bonan Wang, Hayden Brady, Jules J Magda, and Bruce K Gale. “Viscoelastic particle focusing and separation in a spiral channel”. In: *Micromachines* 13.3 (2022), p. 361.

[135] Francesco Del Giudice. “Viscoelastic focusing of polydisperse particle suspensions in a straight circular microchannel”. In: *Microfluidics and Nanofluidics* 23 (2019), pp. 1–11.

[136] Robert M Haralick. “Statistical and structural approaches to texture”. In: *Proceedings of the IEEE* 67.5 (1979), pp. 786–804.

[137] Je-Ho Lee, Kun-Sop Kim, Byung-Deok Nam, Jae-Chon Lee, Yong-Moo Kwon, and Hyoung-Gon Kim. “Implementation of a passive automatic focusing algorithm for digital still camera”. In: *IEEE transactions on consumer electronics* 41.3 (1995), pp. 449–454.

[138] Jay M Tenenbaum. *Accommodation in computer vision*. Stanford University, 1971.

[139] Juha Vuorte, SE Jansson, and Heikki Repo. “Evaluation of red blood cell lysing solutions in the study of neutrophil oxidative burst by the DCFH assay”. In: *Cytometry* 43.4 (2001), pp. 290–296.

[140] Xavier Bossuyt, Gerald E Marti, and Thomas A Fleisher. “Comparative analysis of whole blood lysis methods for flow cytometry”. In: *Cytometry: The Journal of the International Society for Analytical Cytology* 30.3 (1997), pp. 124–133.

[141] MA Boyd, SM Tennant, JH Melendez, D Toema, JE Galen, CD Geddes, and MM Levine. "Adaptation of red blood cell lysis represents a fundamental breakthrough that improves the sensitivity of Salmonella detection in blood". In: *Journal of applied microbiology* 118.5 (2015), pp. 1199–1209.

[142] Xuexin Duan, Yue Li, Nitin K Rajan, David A Routenberg, Yorgo Modis, and Mark A Reed. "Quantification of the affinities and kinetics of protein interactions using silicon nanowire biosensors". In: *Nature nanotechnology* 7.6 (2012), pp. 401–407.

[143] Patricia C Weber, Douglas H Ohlendorf, JJ Wendoloski, and FR Salemme. "Structural origins of high-affinity biotin binding to streptavidin". In: *Science* 243.4887 (1989), pp. 85–88.

[144] Dohyun Kim and Amy E Herr. "Protein immobilization techniques for microfluidic assays". In: *Biomicrofluidics* 7.4 (2013), p. 041501.

[145] Jan Van den Bossche, Katrien Devreese, Ronald Malfait, Martine Van de Vyvere, Annick Wauters, Hugo Neels, and Pieter De Schouwer. "Reference intervals for a complete blood count determined on different automated haematology analysers: Abx Pentra 120 Retic, Coulter Gen-S, Sysmex SE 9500, Abbott Cell Dyn 4000 and Bayer Advia 120". In: *Clinical Chemistry and Laboratory Medicine* 40 (2002), pp. 69–73.

[146] Zoltan Varga, Edwin Van der Pol, Marcell Palmai, Raul Garcia-Diez, Christian Gollwitzer, Michael Krumrey, J-L Fraikin, et al. "Hollow organosilica beads as reference particles for optical detection of extracellular vesicles". In: *Journal of Thrombosis and Haemostasis* 16.8 (2018), pp. 1646–1655.

[147] ISO Vim. "International vocabulary of basic and general terms in metrology (VIM)". In: *International Organization* 2004 (2004), pp. 09–14.

[148] Matteo Vidali, Anna Carobene, Sara Apassiti Esposito, Gavino Napolitano, Alessandra Caracciolo, Michela Seghezzi, Giulia Previtali, et al. "Standardization and harmonization in hematology: Instrument alignment, quality control materials, and commutability issue". In: *International Journal of Laboratory Hematology* 43.3 (2021), pp. 364–371.

[149] Matthias Kutzner. "Metrological traceability of values assigned to Sysmex SCS-1000 haematology calibrator". In: *Sysmex J Inter* 12 (2002), pp. 49–55.

[150] Young Ran Kim and Leonard Ornstein. "Isovolumetric sphering of erythrocytes for more accurate and precise cell volume measurement by flow cytometry". In: *Cytometry: The Journal of the International Society for Analytical Cytology* 3.6 (1983), pp. 419–427.

[151] Benjamin Rappaz, Alexander Barbul, Yves Emery, Rafi Korenstein, Christian Depeursinge, Pierre J Magistretti, and Pierre Marquet. "Comparative study of human erythrocytes by digital holographic microscopy, confocal microscopy, and impedance volume analyzer". In: *Cytometry Part A: The Journal of the International Society for Analytical Cytology* 73.10 (2008), pp. 895–903.

[152] Minseok Seo, Chantal Paquet, Zhihong Nie, Shengqing Xu, and Eugenia Kumacheva. “Microfluidic consecutive flow-focusing droplet generators”. In: *Soft Matter* 3.8 (2007), pp. 986–992.

[153] Barbara J Ballermann, Alan Dardik, Eudora Eng, and Ailian Liu. “Shear stress and the endothelium”. In: *Kidney International* 54 (1998), S100–S108.

[154] JM Ramstack, L Zuckerman, and LF Mockros. “Shear-induced activation of platelets”. In: *Journal of biomechanics* 12.2 (1979), pp. 113–125.

[155] Jolyon Jesty, Wei Yin, Peter Perrotta, and Danny Bluestein. “Platelet activation in a circulating flow loop: combined effects of shear stress and exposure time”. In: *Platelets* 14.3 (2003), pp. 143–149.

[156] SP Sutera and MH Mehrjardi. “Deformation and fragmentation of human red blood cells in turbulent shear flow”. In: *Biophysical journal* 15.1 (1975), pp. 1–10.

[157] Herbert H Lipowsky, Shunichi Usami, and Shu Chien. “In vivo measurements of “apparent viscosity” and microvessel hematocrit in the mesentery of the cat”. In: *Microvascular research* 19.3 (1980), pp. 297–319.

[158] Herbert H Lipowsky, Steven Kovalcheck, and Benjamin W Zweifach. “The distribution of blood rheological parameters in the microvasculature of cat mesentery.” In: *Circulation research* 43.5 (1978), pp. 738–749.

[159] KP Ivanov, MK Kalinina, and Yu I Levkovich. “Blood flow velocity in capillaries of brain and muscles and its physiological significance”. In: *Microvascular research* 22.2 (1981), pp. 143–155.

[160] Lewis Wexler, Derek H Bergel, Ivor T Gabe, Geoffrey S Makin, and Christopher J Mills. “Velocity of blood flow in normal human venae cavae”. In: *Circulation Research* 23.3 (1968), pp. 349–359.

[161] Xinyi Dai, Guowei Zhou, and Luzhou Xu. “Associations between red blood cell count and metabolic dysfunction-associated fatty liver disease (MAFLD)”. In: *Plos one* 17.12 (2022), e0279274.

[162] Taesik Go, Hyeokjun Byeon, and Sang Joon Lee. “Focusing and alignment of erythrocytes in a viscoelastic medium”. In: *Scientific reports* 7.1 (2017), pp. 1–10.

[163] S Majid Hosseini and James J Feng. “How malaria parasites reduce the deformability of infected red blood cells”. In: *Biophysical journal* 103.1 (2012), pp. 1–10.

[164] Lydie Da Costa, Julie Galimand, Odile Fenneteau, and Narla Mohandas. “Hereditary spherocytosis, elliptocytosis, and other red cell membrane disorders”. In: *Blood reviews* 27.4 (2013), pp. 167–178.

[165] Gilda A Barabino, Manu O Platt, and Dhananjay K Kaul. “Sickle cell biomechanics”. In: *Annual review of biomedical engineering* 12 (2010), pp. 345–367.

[166] Mohammad Asghari, Murat Serhatlioglu, Bülend Ortaç, Mehmet E Solmaz, and Caglar Elbuken. “Sheathless microflow cytometry using viscoelastic fluids”. In: *Scientific reports* 7.1 (2017), pp. 1–14.

[167] Patrick Horn, Simone Bork, and Wolfgang Wagner. “Standardized isolation of human mesenchymal stromal cells with red blood cell lysis”. In: *Mesenchymal Stem Cell Assays and Applications* (2011), pp. 23–35.

[168] Jonghee Yoon, YoungJu Jo, Min-hyeok Kim, Kyoohyun Kim, SangYun Lee, Suk-Jo Kang, and YongKeun Park. “Identification of non-activated lymphocytes using three-dimensional refractive index tomography and machine learning”. In: *Scientific reports* 7.1 (2017), p. 6654.

[169] Martin Stocker, Matteo Fontana, Salhab El Helou, Karl Wegscheider, and Thomas M Berger. “Use of procalcitonin-guided decision-making to shorten antibiotic therapy in suspected neonatal early-onset sepsis: prospective randomized intervention trial”. In: *Neonatology* 97.2 (2010), pp. 165–174.

[170] A Lavrentieva, S Papadopoulou, J Kioumis, E Kaimakamis, and M Bitzani. “PCT as a diagnostic and prognostic tool in burn patients. Whether time course has a role in monitoring sepsis treatment”. In: *Burns* 38.3 (2012), pp. 356–363.

[171] G Töpfer, U Funke, M Schulze, G Lutze, S Ziemer, G Siegert, and U Frick. “Präanalytische Probleme bei Gerinnungsuntersuchungen im venösen Citratblut, Katheterblut und Kapillarblut. Determination of Coagulation Parameters in Citrated Venous Blood, Catheter Blood, and Capillary Blood: Preanalytical Problems”. In: *LaboratoriumsMedizin/Journal of Laboratory Medicine* 24.11 (2000), pp. 514–520.

[172] Jürgen K Koscielny, Reinhard Latza, Stefan Mürsdorf, Christof Mrowietz, Holger Kiesewetter, Ernst Wenzel, and Friedrich Jung. “Capillary microscopic and rheological dimensions for the diagnosis of von Willebrand disease in comparison to other haemorrhagic diatheses”. In: *Thrombosis and haemostasis* 84.12 (2000), pp. 981–988.

[173] Giuseppe Lippi. “Pre-examination procedures in laboratory diagnostics”. In: *LaboratoriumsMedizin* 40.1 (2016), pp. 63–63.

[174] Alan D Michelson. “Methods for the measurement of platelet function”. In: *The American journal of cardiology* 103.3 (2009), 20A–26A.

[175] Grégory Nuel and André Garcia. “A timed tally counter for microscopic examination of thick blood smears in malaria studies”. In: *Malaria Journal* 20 (2021), pp. 1–11.

[176] David A Basiji, William E Ortyn, Luchuan Liang, Vidya Venkatachalam, and Philip Morrissey. “Cellular image analysis and imaging by flow cytometry”. In: *Clinics in laboratory medicine* 27.3 (2007), pp. 653–670.

[177] Satoshi Suzuki et al. “Topological structural analysis of digitized binary images by border following”. In: *Computer vision, graphics, and image processing* 30.1 (1985), pp. 32–46.

[178] Kaiming He, Georgia Gkioxari, Piotr Dollár, and Ross Girshick. “Mask r-cnn”. In: *Proceedings of the IEEE international conference on computer vision*. 2017, pp. 2961–2969.

[179] Shaoqing Ren, Kaiming He, Ross Girshick, and Jian Sun. "Faster r-cnn: Towards real-time object detection with region proposal networks". In: *Advances in neural information processing systems* 28 (2015).

[180] Kaiming He, Xiangyu Zhang, Shaoqing Ren, and Jian Sun. "Deep residual learning for image recognition". In: *Proceedings of the IEEE conference on computer vision and pattern recognition*. 2016, pp. 770–778.

[181] Gary Bradski. "The openCV library." In: *Dr. Dobb's Journal: Software Tools for the Professional Programmer* 25.11 (2000), pp. 120–123.

[182] Martin Abadi, Ashish Agarwal, Paul Barham, Eugene Brevdo, Zhifeng Chen, Craig Citro, Greg S Corrado, et al. "Tensorflow: Large-scale machine learning on heterogeneous distributed systems". In: *arXiv preprint arXiv:1603.04467* (2016).

[183] Chao Wang, Brian R Smith, Kenneth A Ault, and Henry M Rinder. "Reticulated platelets predict platelet count recovery following chemotherapy". In: *Transfusion* 42.3 (2002), pp. 368–374.

[184] G Rock, VA Sherring, and P Tittleyx. "Five-day storage of platelet concentrates". In: *Transfusion* 24.2 (1984), pp. 147–152.

[185] Larry J Dumont, James P AuBuchon, Pamela Whitley, Louise H Herschel, Adrienne Johnson, Deanna McNeil, Sherrie Sawyer, et al. "Seven-day storage of single-donor platelets: recovery and survival in an autologous transfusion study". In: *Transfusion* 42.7 (2002), pp. 847–854.

[186] Rob Fijnheer, Piet W Modderman, H Veldman, Willem H Ouwehand, H Karel Nieuwenhuis, Dirk Roos, and Dirk de Korte. "Detection of platelet activation with monoclonal antibodies and flow cytometry. Changes during platelet storage". In: *Transfusion* 30.1 (1990), pp. 20–25.

[187] Valery Leytin, Meera Mody, John W Semple, Bernadette Garvey, and John Freedman. "Flow cytometric parameters for characterizing platelet activation by measuring P-selectin (CD62) expression: theoretical consideration and evaluation in thrombin-treated platelet populations". In: *Biochemical and biophysical research communications* 269.1 (2000), pp. 85–90.

[188] Alan D Michelson, Marc R Barnard, Lori A Krueger, C Robert Valeri, and Mark I Furman. "Circulating monocyte-platelet aggregates are a more sensitive marker of in vivo platelet activation than platelet surface P-selectin: studies in baboons, human coronary intervention, and human acute myocardial infarction". In: *Circulation* 104.13 (2001), pp. 1533–1537.

[189] John C Marshall, Srinivas Murthy, Janet Diaz, NK Adhikari, Derek C Angus, Yaseen M Arabi, Kenneth Baillie, et al. "A minimal common outcome measure set for COVID-19 clinical research". In: *The Lancet Infectious Diseases* 20.8 (2020), e192–e197.

[190] Ayusha Poudel, Yashasa Poudel, Anurag Adhikari, Barun Babu Aryal, Debika Dangol, Tamanna Bajracharya, Anil Maharjan, et al. "D-dimer as a biomarker for assessment of COVID-19 prognosis: D-dimer levels on admission and its role in predicting disease outcome in hospitalized patients with COVID-19". In: *Plos one* 16.8 (2021), e0256744.

[191] Andrey Skripchenko, James Kurtz, Gary Moroff, and Stephen J Wagner. "Platelet products prepared by different methods of sedimentation undergo platelet activation differently during storage". In: *Transfusion* 48.7 (2008), pp. 1469–1477.

[192] Theodoros G Papaioannou, Christodoulos Stefanadis, et al. "Vascular wall shear stress: basic principles and methods". In: *Hellenic J Cardiol* 46.1 (2005), pp. 9–15.

[193] Katherine A Twohig, Tommy Nyberg, Asad Zaidi, Simon Thelwall, Mary A Sinnathamby, Shirin Aliabadi, Shaun R Seaman, et al. "Hospital admission and emergency care attendance risk for SARS-CoV-2 delta (B. 1.617. 2) compared with alpha (B. 1.1. 7) variants of concern: a cohort study". In: *The Lancet Infectious Diseases* 22.1 (2022), pp. 35–42.

[194] Nicholas G Davies, Christopher I Jarvis, W John Edmunds, Nicholas P Jewell, Karla Diaz-Ordaz, and Ruth H Keogh. "Increased mortality in community-tested cases of SARS-CoV-2 lineage B. 1.1. 7". In: *Nature* 593.7858 (2021), pp. 270–274.

[195] Jesse Fajnzylber, James Regan, Kendyll Coxen, Heather Corry, Colline Wong, Alexandra Rosenthal, Daniel Worrall, et al. "SARS-CoV-2 viral load is associated with increased disease severity and mortality". In: *Nature communications* 11.1 (2020), p. 5493.

[196] David M Smadja, Olivier M Bory, Jean-Luc Diehl, Alexis Mareau, Nicolas Gendron, Anne-Sophie Jannot, and Richard Chocron. "Daily monitoring of D-dimer allows outcomes prediction in COVID-19". In: *TH Open* 6.01 (2022), e21–e25.

[197] Fang Liu, Lin Li, MengDa Xu, Juan Wu, Ding Luo, YuSi Zhu, BiXi Li, et al. "Prognostic value of interleukin-6, C-reactive protein, and procalcitonin in patients with COVID-19". In: *Journal of clinical virology* 127 (2020), p. 104370.

[198] Rui Hu, Chaofei Han, Shiyao Pei, Mingzhu Yin, and Xiang Chen. "Procalcitonin levels in COVID-19 patients". In: *International journal of antimicrobial agents* 56.2 (2020), p. 106051.

[199] Isabell Pink, David Raupach, Jan Fuge, Ralf-Peter Vonberg, Marius M Hoeper, Tobias Welte, and Jessica Rademacher. "C-reactive protein and procalcitonin for antimicrobial stewardship in COVID-19". In: *Infection* 49.5 (2021), pp. 935–943.

[200] Sasidhar Guthikonda, Carlos L Alviar, Muthiah Vaduganathan, Mehmet Arikan, Armando Tellez, Timothy DeLao, Juan F Granada, et al. "Role of reticulated platelets and platelet size heterogeneity on platelet activity after dual antiplatelet therapy with aspirin and clopidogrel in patients with stable coronary artery disease". In: *Journal of the American College of Cardiology* 52.9 (2008), pp. 743–749.

[201] Emma Lefrançais, Guadalupe Ortiz-Muñoz, Axelle Caudrillier, Beñat Mallavia, Fengchun Liu, David M Sayah, Emily E Thornton, et al. “The lung is a site of platelet biogenesis and a reservoir for haematopoietic progenitors”. In: *Nature* 544.7648 (2017), pp. 105–109.

[202] S Guthikonda, EI Lev, R Patel, T DeLao, AL Bergeron, JF DONG, and Neal S Kleiman. “Reticulated platelets and uninhibited COX-1 and COX-2 decrease the antiplatelet effects of aspirin”. In: *Journal of Thrombosis and Haemostasis* 5.3 (2007), pp. 490–496.

[203] Preeti Bhoria, Saniya Sharma, Neelam Varma, Pankaj Malhotra, Subhash Varma, and Manni Luthra-Guptasarma. “Effect of steroids on the activation status of platelets in patients with Immune thrombocytopenia (ITP)”. In: *Platelets* 26.2 (2015), pp. 119–126.

[204] Karla Romero Starke, David Reissig, Gabriela Petereit-Haack, Stefanie Schmauder, Albert Nienhaus, and Andreas Seidler. “The isolated effect of age on the risk of COVID-19 severe outcomes: a systematic review with meta-analysis”. In: *BMJ global health* 6.12 (2021), e006434.

[205] Khanh Thu Nguyen. “Automation of a digital holographic microscope for the Application as a medical technology product”. Bachelor’s Thesis. Technical University of Munich, 2021.

[206] Özgün Turgut. “Development of digital holographic microscopy towards an in vitro diagnostic device for high-throughput haematology analysis”. Master’s Thesis. Technical University of Munich, 2021.

Publications Associated with this Work

[207] **Klenk, Christian**, Johanna Erber, David Fresacher, Stefan Röhrl, Manuel Lengl, Dominik Heim, Hedwig Irl, et al. "Platelet aggregates detected using quantitative phase imaging associate with COVID-19 severity". In: *Nature Communications Medicine* 3.1 (2023), p. 161.

[208] **Klenk, Christian**, David Fresacher, Stefan Röhrl, Dominik Heim, Manuel Lengl, Simon Schumann, Martin Knopp, et al. "Measurement of Platelet Aggregation in Ageing Samples and After in-Vitro Activation". In: *Proceedings of the 16th International Joint Conference on Biomedical Engineering Systems and Technologies* (2023).

[209] Stefan Röhrl, Lukas Bernhard, Manuel Lengl, **Klenk, Christian**, Dominik Heim, Martin Knopp, Simon Schumann, et al. "Explainable Feature Learning with Variational Autoencoders for Holographic Image Analysis". In: *Proceedings of the 16th International Joint Conference on Biomedical Engineering Systems and Technologies* (2023).

[210] Stefan Röhrl, Hendrik Maier, Manuel Lengl, **Klenk, Christian**, Dominik Heim, Martin Knopp, Simon Schumann, et al. "Explainable Artificial Intelligence for Cytological Image Analysis". In: *Artificial Intelligence in Medicine (AIME)* (2023), pp. 75–85.

[211] Alice Hein, Stefan Röhrl, Thea Grobel, Manuel Lengl, Nawal Hafez, Martin Knopp, **Klenk, Christian**, et al. "A Comparison of Uncertainty Quantification Methods for Active Learning in Image Classification". In: *2022 International Joint Conference on Neural Networks (IJCNN)* (2022), pp. 1–8.

[212] Stefan Röhrl, Alice Hein, Lucie Huang, Dominik Heim, **Klenk, Christian**, Manuel Lengl, Martin Knopp, et al. "Outlier Detection using Self-Organizing Maps for Automated Blood Cell Analysis". In: *arXiv preprint arXiv:2208.08834* (2022).

[213] Oliver Hayden and **Klenk, Christian**. "Morphology–Here I Come Again". In: *Cytometry Part A* (2020).

[214] **Klenk, Christian**, Dominik Heim, Matthias Ugele, and Oliver Hayden. "Impact of sample preparation on holographic imaging of leukocytes". In: *Optical Engineering* 59.10 (2020), pp. 102403–102403.

[215] Stefan Röhrl, Matthias Ugele, **Klenk, Christian**, Dominik Heim, Oliver Hayden, and Klaus Diepold. "Autoencoder Features for Differentiation of Leukocytes Based on Digital Holographic Microscopy (DHM)". In: *Computer Aided Systems Theory–EUROCAST 2019: 17th International Conference, Las Palmas de Gran Canaria, Spain, February 17–22, 2019, Revised Selected Papers, Part II 17* (2020), pp. 281–288.

Patent Applications Associated with this Thesis

[216] Oliver Hayden, **Klenk, Christian**, and Stefan Röhrl. "Detection of cell aggregates using quantitative phase-contrast microscopy". EP4124846A1. 2023.

[217] Oliver Hayden, **Klenk, Christian**, and Stefan Röhrl. "Detection of molecular biological objects, cellular biological objects and cell aggregates using quantitative phase-contrast microscopy". WO2023006372A1. 2023.

[218] Oliver Hayden, Katja Peschke, Maximilian Reichert, **Klenk, Christian**, Percy Knolle, and Bastian Höchst. "Analysis of tissue samples using quantitative phase-contrast microscopy". WO2022096315A1. 2023.

[219] Matthias Ugele, **Klenk, Christian**, Oliver Hayden, Bernd Kaspers, Nina Burkhardt, and Stefan Röhrl. "Calibration of devices for optical analysis of blood samples". WO2022152543A1. 2022.